Reducing uncertainty for laser triangulation measurements on moving samples

DIPLOMARBEIT

Ausgeführt zum Zwecke der Erlangung des akademischen Grades eines
Diplom Ingeneurs (Dipl. Ing.)

unter der Leitung von
Assoc.-Prof. Dr.techn. Ernst Csencsics
Dipl.-Ing. Daniel Wertjanz
Univ.-Prof. Dr.sc.techn. Georg Schitter

eingereicht an der
Technischen Universität Wien
Fakultät für Elektrotechnik und Informationstechnik
Institut für Automatisierungs- und Regelungstechnik

von
Thomas Kern, BSc
Matrikelnummer: 11731719

Wien, im Dezember 2023

Advanced Mechatronic Systems Group
Gußhausstrasse 27-29, A-1040 Wien, Internet: http://www.acin.tuwien.ac.at

Acknowledgement

Abstract

Permanent quality control directly in the production line is of high interest in today's manufacturing facilities to increase throughput and reduce production rejects. As optical sensor systems enable contactless, fast, and precise measurements of surface topologies, they are frequently used for in-line measurements on moving samples. Edges are often defining elements of spatial features on 3D structures, e.g. two edges may define the critical width of a trench structure. Thus, to detect deviations from the feature's dimensional specifications, the lateral position of its edges must be determined accurately. As optical sensors have finite exposure times, the motion of the sample during the exposure induces lateral uncertainty. This thesis aims to reduce the lateral position uncertainty of edge features in laser triangulation measurements on moving samples.

An experimental laser triangulation sensor is developed, which allows access and adjustment of relevant parameters such as exposure time and laser intensity and the readout of its imaging sensor's raw pixel data. Combining 1D Gaussian most-likelihood estimation, matched filtering, and Gaussian-mixture-model fitting, the intensity distribution on the imaging sensor is described and analyzed. Using a model of the laser intensity distribution on the moving sample, the lateral position of edge features is estimated by comparing the peak power ratio on the imaging sensor and the power distribution on the sample.

Experimental performance evaluation shows a significant reduction of the lateral edge position uncertainty. The performance of the proposed method is determined by comparing statically and dynamically measured feature widths of a 3D printed sample. The results show a significant reduction of the mean absolute error in the corrected measurements of more than 60% compared to uncorrected measurements. Moreover, features that are missed due to motion blur in the uncorrected measurements are detected with high lateral accuracy by the proposed method.

Kurzfassung

Um den Durchsatz in industriellen Fertigungsanlagen zu erhöhen und Produktausschüsse zu reduzieren, ist eine permanente Qualitätskontrolle direkt in der Fertigungslinie essenziell. Da optische Sensorsysteme berührungslose, schnelle und präzise Messungen von Oberflächentopologien und -strukturen ermöglichen, werden sie häufig für Inline-Messungen an bewegten Objekten eingesetzt. Kanten sind oft kennzeichnenede Merkmale von Oberfächenstrukturen. Um Abweichungen von den Dimensionsspezifikationen zu erkennen, muss daher die laterale Position von Kanten genau bestimmt werden. Da optische Sensoren endliche Belichtungszeiten haben, führt die Bewegung des Objekts während der Belichtung zu einer lateralen Unsicherheit. Ziel dieser Arbeit ist es, die laterale Positionsunsicherheit von Kanten bei Lasertriangulationsmessungen an bewegten Objekten zu reduzieren.

Es wird ein experimenteller Lasertriangulationssensor entwickelt, der die Anpassung essenzieller Messparameter und das Auslesen von Pixel-Rohdatan ermöglicht. Durch statistische Methoden wird die Intensitätsverteilung am Bildsensor beschrieben und analysiert. Unter Verwendung eines Modells der Laserintensitätsverteilung auf dem bewegten Objekt wird die laterale Position von Kanten durch Vergleich der Intensitätsverteilung auf dem Bildsensor und der Leistungsverteilung auf dem Objekt geschätzt.

Die experimentelle Evaluierung zeigt eine signifikante Verringerung der Unsicherheit der lateralen Kantenposition. Die Leistungsfähigkeit des Korrekturalgorithmus wird durch den Vergleich statisch und dynamisch gemessener Featurebreiten einer 3D-gedruckten Probe ermittelt. Die Ergebnisse zeigen eine signifikante Verringerung des mittleren absoluten Fehlers bei den korrigierten Messungen um mehr als 60% im Vergleich zu den unkorrigierten Messungen. Darüber hinaus werden Merkmale, die bei den unkorrigierten Messungen aufgrund von Bewegungsunschärfe übersehen werden, durch den Korrekturalgorithmus mit hoher lateraler Genauigkeit erkannt.

Contents

List of Figures

List of Tables

Acronyms

ADC analog digital converter.

APS active pixel sensor.

CCD charge-coupled device.

CCS confocal chromatic sensor.

CDF cumulative distribution function.

CNN convolutional neural network.

COG center of gravity.

DPS digital pixel sensor.

DR dimensionality reduction.

EM expectation-maximization.

FD floating diffusion.

FDM fused deposition modeling.

FSM fast steering mirror.

GMM Gaussian mixture model.

ICA independent component analysis.

LDA linear discriminant analysis.

LTS laser triangulation sensor.

MLE maximum likelihood estimation.

NLSQ nonlinear least squares.

PCA principal component analysis.

PDF probability density function.

PPS passive pixel sensor.

PSF point spread function.

RAM random access memory.

ROI region of interest.

SLA stereolithography.

CHAPTER 1

Introduction

In the last decades, the demand for throughput and product quality in industrial manufacturing, especially in the high-tech sector, has been constantly increasing [1]. With the growing demand for precision, high-performance measurement systems are ever more sought-after [2]. To keep up with the increasing requirements of today's manufacturing processes, measurement systems are required to be fast, precise, robust, and integrable into the production line [3].

1.1 Motivation

The integration of measurement systems in the production line allows permanent quality inspection of the produced goods. Thus, manufacturing parameters can be dynamically adapted, and production rejects are reduced [4]. Surface structure and condition frequently serve as a quality criterion [5, 6]. Detection of dimensional deviations from the desired specifications is a frequently performed task in quality inspection. Edges are often defining elements of spatial features on 3D structures, e.g. two edges may define the critical width of a trench structure. Thus, to detect such feature width deviations, the lateral edge positions have to be determined accurately. [7].

Due to the required throughput and high production speed, quality inspection has to be performed on the moving products to maintain the production flow. Thus, systems that combine fast measurements with high lateral resolution are required [8].

1

With their contactless measurement principle and high measurement rates, optical sensor systems are of great interest in this field of application [9].

As optical sensor systems use imaging sensors with finite exposure times, their measurement results are affected by motion blur when the object is moving during the exposure [10]. This effect is similar to the often experienced motion blur in photography. When taking an image of a moving object, or the imaging system itself is moving, the obtained image appears blurred. Both, an increase of the exposure time and an increase of the relative speed between the object and the imaging system enhance the motion blur effect [11]. Thus, optical measurement systems with high measurement rates and short exposure times are less prone to blurring. However, short exposure times require a high intensity of the incoming light. In the case of laser triangulation sensors (LTSs), short exposure times require high laser intensities which require inconvenient and costly laser-safety precautions in the production line [12].

Moreover, the finite exposure time of optical sensors limits their sampling rate. Hence, measurement values are only obtained at discrete sampling points in time. As the sample is moving laterally during the exposure, the sampling time of the sensor system causes spatial sampling on the object. Therefore, the detectable minimum lateral feature size increases with increasing sample speed and exposure time, reducing the lateral resolution of the optical sensor system.
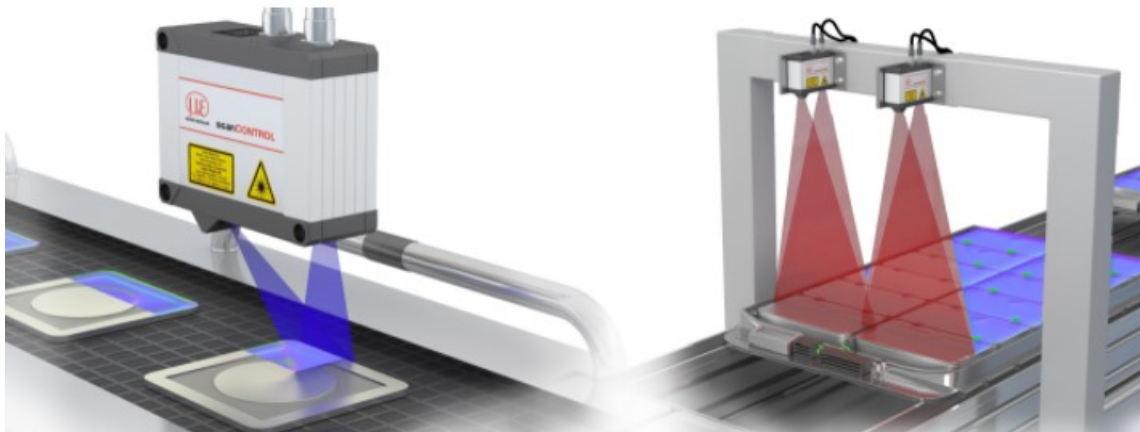
Figure 1.1: Exemplary illustration of an in-line measurement application. Laser line triangulation sensors measure the surface structure of objects moving on a conveyor belt [13].

1.2 Challenges and Goals

Considering the industrial demands for minimal lateral accuracy in detecting edge features on moving samples, a sensor system with high lateral resolution is required. Their contactless and fast measurement principle makes optical sensor systems suitable for in-line measurement applications. Escpecially LTSs are frequently used, since they combine high axial resolution with an extensive measurement range [14]. Their finite exposure time induces lateral uncertainty when detecting the location of edge features on moving samples. Therefore, a novel method to reduce the lateral uncertainty of laser triangulation measurements on moving samples is required. Since the minimum exposure time is frequently limited by the intensity of the incoming light due to laser-safety regulations, a method that either compensates for the relative motion between the sample and the sensor system, or computationally corrects the lateral error is required. Hence, the project goals of this thesis are defined as follows:

- Reduction of lateral edge position uncertainty

- Mitigation of motion blur effects

- Performance evaluation by performing dynamic measurements on moving samples

1.3 Thesis Outline

The thesis is structured as follows. Chapter 2 provides an overview of state-of-the-art measurement systems for in-line quality inspection applications. Furthermore, motion compensation and correction approaches are presented. Based on the literature review, research questions are formulated. The causes of lateral feature uncertainty in laser triangulation measurements are discussed in Chapter 3. Considering the project goals, design guidelines for LTSs are formulated in Chapter 4. Moreover, considering the derived guidelines, the design of an experimental LTS is described. Using the developed experimental LTS, effects of measurements on edges are analyzed, and methods for modeling intensity distributions on the imaging sensor and the sample are proposed in Chapter 5. Using the derived models a lateral feature location correction algorithm is developed in Chapter 6. The performance of the proposed correction algorithm is experimentally validated in Chapter 7. Chapter 8 concludes the thesis and provides an outlook of possible future work in uncertainty reduction for measurements on moving samples.

CHAPTER 2

State of the art

This chapter provides a literature overview of state-of-the-art in-line measurement systems for measurements on moving objects. First, frequently used optical measurement systems are discussed and compared. Subsequently, an overview of the most used imaging sensors for optical measurements is given. Moreover, active sample motion compensation strategies are presented, as well as motion-induced error correction approaches, by deblurring algorithms. Finally, the presented methods are compared, and research questions are formulated.

2.1 Industrial displacement sensors

As surface condition and shape are of great interest in quality inspection applications , high precision and high-resolution measurement systems suitable for in-line applications are required [9]. In the domain of nano-metrology, white light interferometers are frequently used due to their high resolution in the nanometer scale [15, 16]. However, their measurement results are sensitive to ambient vibrations [17]. Hence, they are unsuitable for implementation in the vibration-prone environment of industrial manufacturing lines [18].

Inductive displacement sensors achieve fast measurements with a resolution in the nanometer scale [19]. However, their applicability is limited to conductive materials, which decreases their flexibility [20]. Capacitive displacement sensors overcome this drawback since they can be used on conductive materials and insulators [21]. While achieving nanometer-scale resolution, their measurement range is limited to

a few millimeters [22, 23]. Furthermore, the lateral resolution of both inductive and capacitive displacement sensors is determined and limited by the magnetic and electric field distribution [24].

Optical displacement sensors such as confocal chromatic sensors (CCSs) and LTSs offer high axial and lateral resolution while achieving an extensive measurement range compared to the previously mentioned systems [25, 26]. Therefore, they are among the most frequently used optical measurement systems for in-line measurement applications and are thus discussed in more detail [27].

2.1.1 Confocal chromatic sensors

CCSs measure the distance to a target through spectral analysis. The essential components of a CCS are illustrated in the schematic structure shown in Fig. 2.1. White light is coupled to an optical fiber and guided to the sensor head. The sensor head contains a lens stack, which induces chromatic aberration. Thereby, the spectral components of the white light are focussed at different distances from the sensor head depending on their wavelength, as shown in Fig. 2.1. The same optical fiber transmits white light to the sensor head and guides the reflected light back to the controller. As the fiber acts as a pinhole, only the light focused on the target gets transmitted back to the controller. Thus, due to the chromatic aberration, the wavelength of the reflected light depends on the distance between the sensor head and the target. The wavelength is determined by a spectrometer, where the wavelengths are separated on a grating and directed to a linear detector array [25, 28].
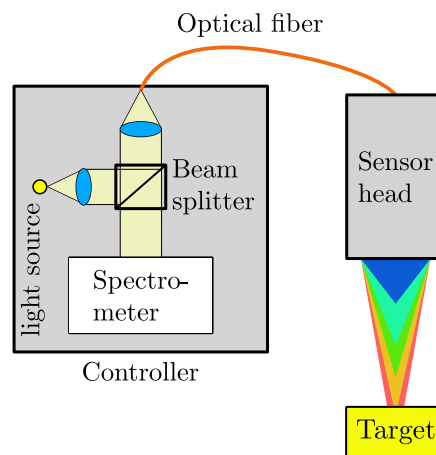
Figure 2.1: Basic components of a confocal chromatic sensor. The distance to the target is determined by analyzing the wavelength of the reflected light [28].

As only the focussed reflected wavelength passes the pinhole of the optical fiber, this measurement system does not suffer from out-of-focus errors. Therefore, thickness measurements can be conducted using a single sensor head when measuring on a transparent target. Since both the upper and lower surfaces of the target reflect light at the respective wavelength, the distance to the target and the thickness can be determined if the refractive index of the target material is known. Industrially available CCSs achieve a resolution in the nanometer scale with a measurement range of single centimeters [25, 28].

2.1.2 Laser triangulation sensors

In contrast to the CCS principle, LTSs use monochromatic laser light to determine the distance to the target by triangulation [26]. The measurement principle is depicted in Fig. 2.2. A laser beam, either collimated or focussed, is directed onto the target. The diffusely reflected spot is focussed on the detector by the lens. The detector, the lens, and the laser are aligned to satisfy the Scheimpflug condition. According to the Scheimpflug condition, a point on the focal plane will be detected sharply if the plane of focus, image, and lens plane intersect in a single line [29]. Thereby, the plane of focus is not parallel to the image plane, as in standard imaging applications, but it is congruent with the plane on which the laser beam propagates from the laser to the target. Thus, the size of the reflected spot on the detector is constant, regardless of the distance to the target.

The displacement d' of the reflected spot, or more precisely it's center of gravity (COG), on the detector concerning the target's displacement d is given as [26, 30]

$$d'(d) = m_{\mathrm{L}} f \sqrt{1 + \left(m_{\mathrm{L}} - \frac{u_0}{f}\right)^2} \frac{\left(\frac{d}{\sqrt{1+m_{\mathrm{L}}^2}}\right)}{\left(\frac{d}{\sqrt{1+m_{\mathrm{L}}^2}} + \frac{u_0}{m_{\mathrm{L}}} - f\right)\left(m_{\mathrm{L}} - \frac{u_0}{f}\right)}, \qquad (2.1)$$

with the triangulation angle Θ, the lens' focal length f, and the distance u_0 from the lens' center to the intersection line, where

$$m_{\mathrm{L}} = \tan(\Theta). \qquad (2.2)$$

As one can see in Eq. (2.1), the relation between the target displacement d and the spot displacement d' is nonlinear. The sensitivity and the measurement range can be adjusted by the parameters Θ and u_0. Industrial precision LTSs achieve measurement ranges of up to $500\,\mathrm{mm}$ with a resolution of $0.1\,\mathrm{\mu m}$ [31].
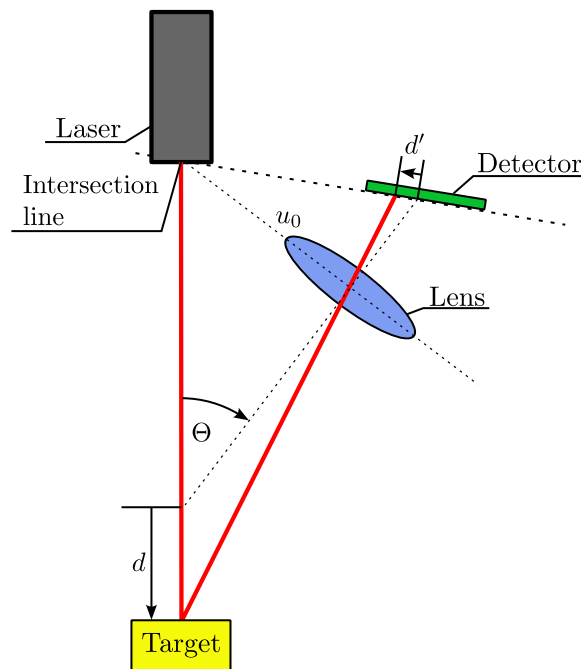
Figure 2.2: Basic geometric arrangement of a laser triangulation sensor. Depending on the geometric parameters, the reflected spot on the detector moves the distance d' for a target displacement d [26].

The principle of a point LTS can also be extended to a line sensor by adding a cylindrical lens in the path of the laser beam and using a 2D imaging sensor as a detector. Thereby, a laser line is projected on the target and reflected on the detector, enabling 3D surface inspections [32].

2.2 Imaging sensors

Both of the considered optical measurement systems typically use imaging sensors to either detect the reflected wavelength in case of a CCS or the COG of the reflected spot in case of the LTS. As the imaging sensor's pixel size and fill factor limit the measurement system's resolution and the framerate limits the measurement rate, these imaging sensors are a critical contributor to the measurement system's performance. Charge-coupled device (CCD) and CMOS imaging sensors are widely used in such measurement systems and, therefore, briefly presented in the following [25, 26].

2.2.1 Charge-Coupled Device imaging sensors

CCD imaging sensors were introduced by W. Boyle and E. Smith in 1969 [33] as analog shift registers. Subsequently, Tompsett et al. [34] were the first who tried to capture images using this technology. Since then, the CCD imaging technology has rapidly evolved, making it the most common high-performance imaging detector for scientific and industrial imaging applications since the 1980s [35].

Imaging with silicon detectors is based on the photoelectric effect [36]. If the condition

$$E_\lambda = \frac{hc}{\lambda} > E_{\text{bandgap}} \tag{2.3}$$

is satisfied, meaning that the photon energy E_λ exceeds the bandgap energy E_{bandgap}, an electron is excited from the silicon valence band to the conduction band. Where h is Planck's constant, c is the speed of light, and λ is the light's wavelength.

The pixels of CCD imaging sensors form potential wells that store charges. The charges result from the photoelectric effect given in Eq. (2.3). Gate structures on the surface, which define the pixels, are used to physically shift the charges from one potential well to the adjacent potential well by applying a clocking voltage to the gates. Thus, the entire image data is read out by shifting charges from one row to the next. The last row is read out serially. Converting the obtained charges to a voltage finally yields the image data. If the whole sensor area is used for active pixels, resulting in the highest fill factor, the pixels get exposed to the incident light during the charge transfer, leading to smearing effects. Thus, a shutter is required to block light from pixels that are currently storing charges generated in a previous row of pixels. As the charges are shifted row by row, a rolling shutter, which only exposes one row at a time, is required. However, when imaging moving objects, the rolling shutter causes unwanted artifacts in the resulting image [37].

To overcome the drawback of rolling shutter, there exist CCD architectures that do not require a shutter. Two of the most commonly used are schematically illustrated in Fig. 2.3. A frame transfer architecture is shown in Fig. 2.3a. The sensor is divided into light-sensitive and light-shielded areas of the same size. Thereby, the whole frame can be stored in the shielded area. Since the charge transfer can be performed very fast ($10^{-6} - 10^{-4}$ s), smearing effects are significantly reduced, and a shutter is obsolete [37].

The interline transfer architecture uses shielded areas to store the charges directly adjacent to the respective active pixel areas. Thus, charges from all pixels can simultaneously be shifted to the shielded areas and subsequently read in a CCD shift-register manner. While this architecture facilitates global shutter-like operation,

(a) Frame transfer sensor   (b) Interline transfer sensor
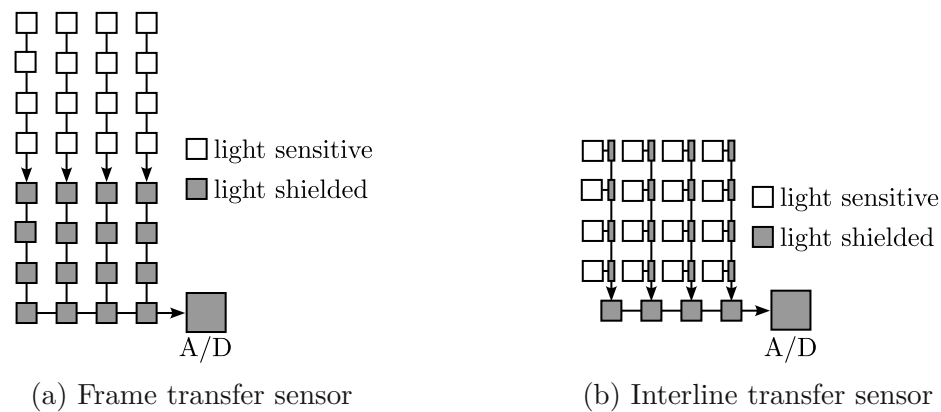
Figure 2.3: Readout methods of CCD arrays. (a) shows a frame transfer sensor, where the charge of each pixel is shifted to the next row until it reaches the readout row, while (b) shows an interline transfer sensor, where the charge of each pixel first gets shifted to a shielded area, facilitating global shutter operation [37].

the fill factor of the sensor is immensely reduced due to the shielded areas between the active pixels [37].

Today's CCD imaging sensors still outperform the CMOS technology regarding noise and fill factor. Furthermore, they show a higher sensitivity than CMOS sensors, which makes them more applicable in low-light conditions. However, region of interest (ROI) readouts are not feasible due to the CCD shift register structure [38].

2.2.2 CMOS imaging sensors

While CMOS imaging sensors were proposed before CCD imaging sensors in 1967 by Weckler et al. [39], they could not compete with the rapidly evolving CCD imaging sensors regarding noise, sensitivity, and fill factor [40]. However, due to significant advancements in CMOS technology in the last decades, especially in terms of miniaturization of semiconductor transistor structures, CMOS imaging sensors slowly replace CCD imaging sensors [41]. Especially the development of active pixel sensors (APSs) [42] significantly improved the SNR, compared to the older passive pixel sensor (PPS) technology [43].

A schematic diagram of an APS pixel using three transistors is illustrated in Fig. 2.4. The pinned photodiode, operated in reverse direction, serves as the sensing element of the pixel. Before the exposure, T1 is turned on, resetting the photodiode by
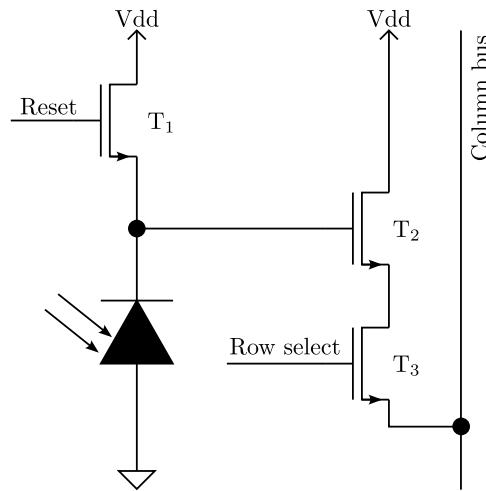
Figure 2.4: Schematic diagram of a 3-Transistor (3T) APS pixel. The APS architecture allows signal amplification at the pixel level [40].

charging its junction capacitance to the initial voltage

$$U_0 = Vdd - U_{\mathrm{DS,T1}}, \tag{2.4}$$

with the supply voltage Vdd and the drain-source voltage of T_1 $U_{\mathrm{DS,T1}}$. At the beginning of the exposure, T_1 is turned off. During the exposure time T_{exp}, the incident light causes a photocurrent I_{photo} due to the photoelectric effect as described in Eq. (2.3). The photocurrent discharges the junction capacitance C_{junciton}, yielding a voltage of

$$U_{\mathrm{D}} = \frac{Q_{\mathrm{D}}}{C_{\mathrm{junction}}} = \underbrace{(Vdd - U_{\mathrm{DS,T1}})}_{U_0} - \frac{1}{C_{\mathrm{junction}}} \int_{t_0}^{t_0+T_{\mathrm{exp}}} I_{\mathrm{photo}}(t)dt, \tag{2.5}$$

after the exposure. This voltage is amplified by the transistor T_2 and finally read out by activating T_3. As all rows of each column of the pixel array are connected via the column bus, T_3 acts as a row select. Thus, each pixel can be read out separately by choosing the respective row and column, similar to a random access memory (RAM) [40].

Adding a fourth transistor T_4 to the circuit leads to the architecture shown in Fig. 2.5. Acting as a transfer gate, the additional transistor shifts the charge from the photodiodes junction capacitance to an n+ doped floating diffusion (FD) where it is intermediately stored. As the transfer action is performed simultaneously on each pixel, the 4T architecture enables global shutter operation, which allows imaging of moving objects without the artifacts caused by the rolling shutter. Same as in
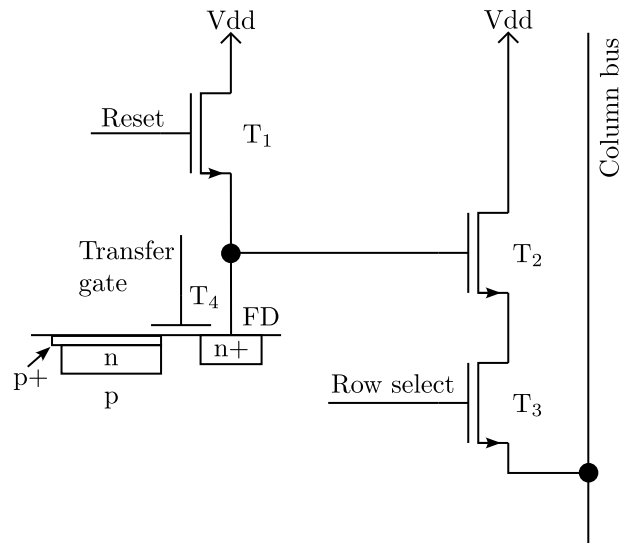
Figure 2.5: Schematic diagram of a 4-transistor (4T) APS pixel. Adding a fourth transistor as a transfer gate allows global shutter operation [40].

the 3T architecture given in Fig. 2.4, the voltage at the FD node is amplified and subsequently read out by the row select transistor [40].

Since each pixel's junction capacitance voltage is amplified directly on the pixel level, an analog digital converter (ADC) for each pixel can be integrated, resulting in a digital pixel sensor (DPS) architecture. Thus, CMOS imaging sensors combine sensing with analog and digital processing on the pixel level, which is a significant advantage over CCD imaging sensors. Using parallel conversion, today's CMOS imaging sensors can operate in the Gigapixel per second scale [44, 45]. Furthermore, CMOS sensors facilitate the readout of a ROI, further speeding up the readout process, as only the desired data has to be transmitted [45].

2.3 Deblurring algorithms

As the presented imaging sensors are used on moving objects, motion blur inevitably corrupts the obtained image [46]. As shown in Eq. (2.5), the voltage of a pixel is proportional to the integrated photocurrent over the exposure time. Thus, when the object is moving during the exposure, the image information that would be present on a single pixel for a static object gets blurred over several pixels. This effect can be modeled as a convolution of the original image $f(a, b)$ and the point spread function

(PSF) $h(a,b)$, resulting in the obtained image [47]

$$g(a,b) = f(a,b) * h(a,b) + n(a,b). \tag{2.6}$$

Additionally to the blurring, the obtained image $g(a,b)$ is corrupted by noise $n(a,b)$. The PSF describes the blur's direction and length. Assuming a linearly moving object with constant speed, the PSF can be modeled as a moving average filter [47]

$$h(a,b) = \frac{1}{L}\Pi_L(a\cos(\Theta) + b\sin(\Theta)), \tag{2.7}$$

with the blur length L, the direction of the blur Θ and the rectangle function

$$\Pi_L(u) = \begin{cases} 1 & |u| \leq \frac{L}{2} \\ 0 & |u| > \frac{L}{2} \end{cases}. \tag{2.8}$$

An example of the effects of motion blur is depicted in Fig. 2.6. The original image in Fig. 2.6a is blurred with a motion blur PSF as given in Eq. (2.7) with a length of $L = 40$ and a blur direction of $\Theta = 45°$.

(a)   (b)
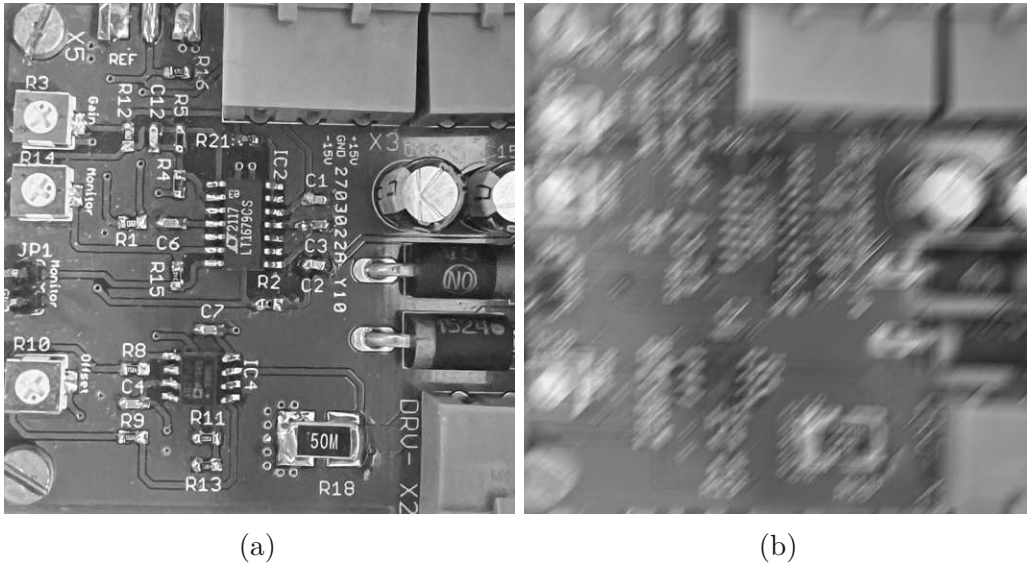
Figure 2.6: Effects of motion blur. The original image in (a) is blurred with a rectangular PSF with a length of 40 px and an angle of 45°. (b) illustrates the resulting blurred image. Own image, cf. [47].

The goal of deblurring algorithms is to estimate the unblurred image $f(a,b)$, given the obtained blurred image $g(a,b)$. Blind deconvolution [48] aims to estimate $f(a,b)$ without knowing the PSF $h(a,b)$, while non-blind deconvolution [49] uses a model of

the PSF. Non-blind convolution is computationally cheaper than blind deconvolution since the PSF is estimated after each iteration in the blind deconvolution approach. Furthermore, since the object's speed, direction, and the imaging sensor's exposure time are typically known in industrial manufacturing lines, the PSF can be modeled, and the parameters can be estimated [49].

For non-uniform motion blur, convolutional neural networks (CNNs) are successfully used to estimate the unblurred image [50]. For constant, linear motion blur, the Wiener Filter [51] and the Richardson-Lucy algorithm [52] are commonly used and thus briefly presented in the following.

2.3.1 Wiener Filter

The Wiener Filter is based on the least-squares image restoration problem and acts as an inverse of the PSF. Deconvolution is performed in the Fourier domain. Hence, in a first step, the blurred image is transformed into Fourier space, yielding [51]

$$G(\alpha, \beta) = F(\alpha, \beta)H(\alpha, \beta) + N(\alpha, \beta), \tag{2.9}$$

with the Fourier transforms of the unblurred image $F(\alpha, \beta)$, the PSF $H(\alpha, \beta)$ and the noise $N(\alpha, \beta)$. As the convolution transforms into a multiplication in the Fourier space, the unblurred image can now be estimated as

$$F(\alpha, \beta) = W(\alpha, \beta)G(\alpha, \beta), \tag{2.10}$$

with the Wiener Filter [53]

$$W(\alpha, \beta) = \frac{H^*(\alpha, \beta)}{|H(\alpha, \beta)|^2 + \frac{1}{\text{SNR}(\alpha,\beta)}}. \tag{2.11}$$

The SNR of the unblurred image is typically unknown and has to be estimated separately. Back-transforming the resulting Fourier transform of the unblurred image $F(\alpha, \beta)$ yields the estimated unblurred image $f(a, b)$. The performance highly depends on the accuracy of the PSF model and the estimate of the SNR. Furthermore, ringing artifacts appear after deblurring the image, which have to be removed in a post-processing step [53].

2.3.2 Richardson-Lucy Algorithm

The Richardson-Lucy algorithm iteratively restores the unblurred image directly in the image domain. Given the PSF and the blurred image, it maximizes the likelihood

of the unblurred image using Bayes-theorem [52]. Neglecting the noise, Eq. (2.6) can be written as a discrete convolution

$$g_i = \sum_j f_j h_{ij},$$ (2.12)

with the pixel indices i, j. The maximum likelihood solution of g_i is found when the iteration

$$f_j^{(t+1)} = f_j^{(t)} \sum_i \frac{g_i}{c_i} h_{ij},$$ (2.13a)

$$c_i = \sum_j f_j^{(t)} h_{ij}$$ (2.13b)

converges [54]. While the performance increases with the number of iterations, ringing artifacts must be removed in a post-processing step.

Compared to the Wiener Filter, no information about the noise is required. Furthermore, no Fourier transforms must be calculated, as the deconvolution is performed directly in the image space. However, both the Wiener Filter and the Richardson-Lucy algorithm require an accurate model of the PSF. Hence, a PSF parameter estimation approach is presented in the following.

2.3.3 Point spread function estimation

As the parameters of the PSF not only depend on known parameters such as exposure time, sample speed, and direction of movement but also on parameters of the used optics and component alignment, precise estimation of the blur parameters is needed [55]. The assumed PSF given in Eq. (2.7) is a rectangle function with the length L and direction Θ. Looking at the Fourier transform of the rectangle function

$$\mathcal{F}\{\Pi_L(u)\} = \frac{2}{\omega} \sin\left(\frac{L\omega}{2}\right) = \frac{4}{L} \text{sinc}\left(\frac{L\omega}{2}\right),$$ (2.14)

one can see that the zeros of the Fourier transform are located at

$$\omega = \frac{k2\pi}{L}, \quad k \in \mathbb{N}.$$ (2.15)

As the Fourier transform of the PSF appears multiplicatively in the Fourier transform of the blurred image (see Eq. (2.9)), the zeros of Eq. (2.14) are zeros of Eq. (2.9) as well, neglecting the noise. Thus, the parameters of the PSF can be determined by analyzing the Fourier transform of the blurred image [47].
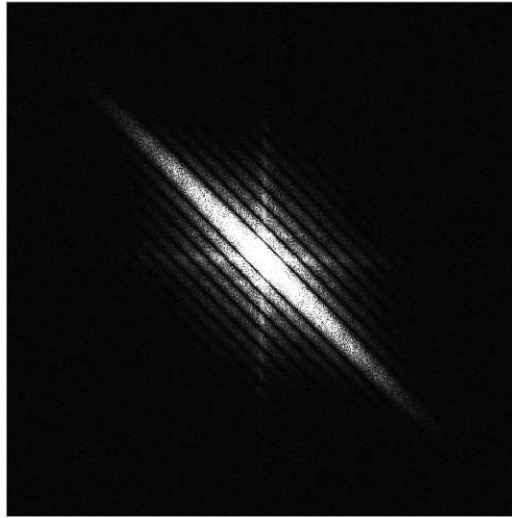
Figure 2.7: Fourier transform of the blurred image. The parallel lines run perpendicular to the blur direction Θ, and the distance between the minima is equal to the blur length L. Own image, cf. [47].

Fig. 2.7 shows the Fourier transform of the blurred image in Fig. 2.6b. The zeros of the PSF are clearly visible as diagonal lines. As the parallel lines in Fig. 2.7 are perpendicular to the direction of the motion blur, the blur direction Θ can be determined by estimating the angle of the visible lines. In literature, the Hough transform [56] or the Radon transform [57] are commonly used for this task. Knowing the blur direction Θ, the blur length L is determined by estimating the distance between the minima.

2.4 Motion compensation

The relative motion between the sample and the sensing system causes motion blur effects in the measurement results. Thus, compensating the relative motion by active sample tracking can mitigate these effects [58]. Wang et al. proposed a compensation approach for surface inspection where the whole camera system is moved at the same speed as the sample using a linear stage as schematically depicted in Fig. 2.8 [58]. The sample's speed has to be accurately measured by an encoder or in-plane sensor to match the speed of the imaging system and sample perfectly.

Hayakawa et al. proposed a motion blur compensation method that manipulates the optical path of a camera using a galvanometer mirror. The sample's speed is not

measured by additional sensors, but by analyzing the background of the obtained images [59]. Manipulating the optical path of point sensors by fast steering mirrors (FSMs) is also a well-known approach in literature [60, 61]. While these approaches are primarily intended to obtain 3D images by scanning the spot over the sample surface, the scanning motion can be adapted to follow the sample, compensating for motion blur. While manipulating the optical path allows high sample speeds, the actuation range is limited by the mirror's actuation range and the displacement sensor's measurement range [61]. Laimer and Wertjanz et al. [62, 63] proposed a robot-based dual-stage in-line measurement system, where an industrial robot extends the measurement range of a fast and precise scanning confocal chromatic sensor [61] in all 6 degrees of freedom as illustrated in Fig. 2.9.
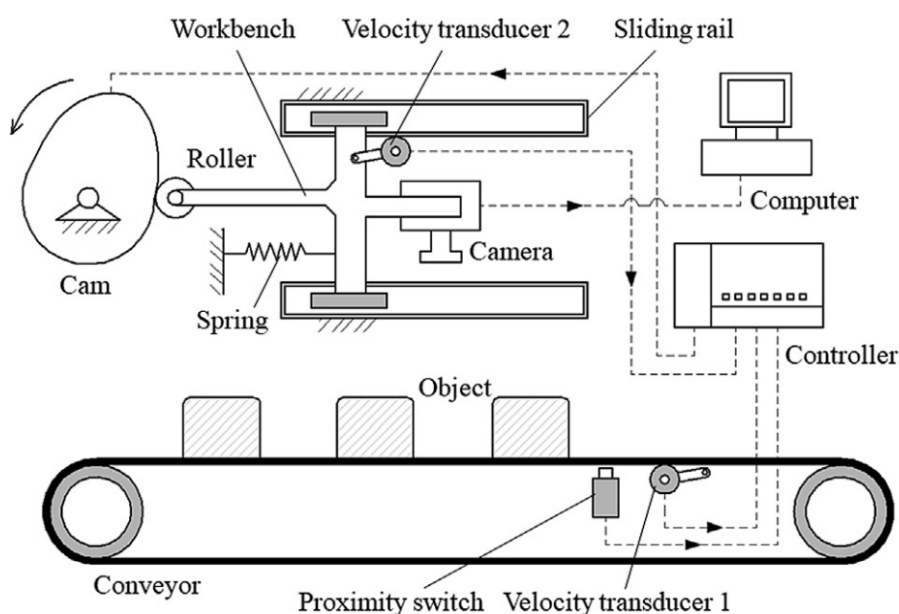
Figure 2.8: Schematic illustration of an active motion compensation system. The sample's motion can be compensated by moving the whole measurement system at the sample's speed [58].

While all these approaches compensate for relative motion between the measurement system and the sample, the actuation system must be reset at the end of its actuation range, yielding a blind spot in the measurement result. Thus, these approaches are limited to piece-good production lines. Furthermore, the sample size is limited by the actuation range of the motion compensation system.
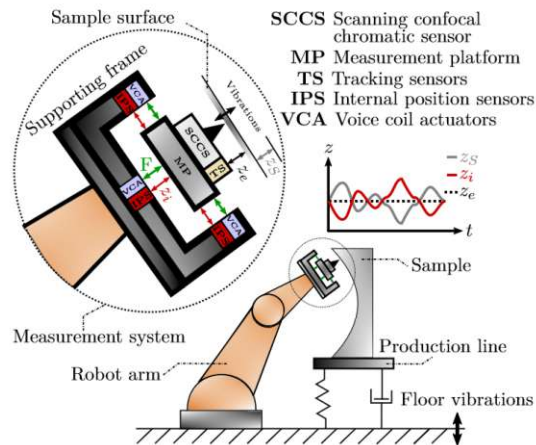
Figure 2.9: Robot based dual-stage approach. The industrial robot extends the
measurement range of the scanning confocal chromatic sensor [63].

2.5 Research questions

Considering the literature review findings, CCSs and LTSs are the most commonly
used measurement systems for fast, precise, and contactless quality inspection within
the production line. While the confocal chromatic principle facilitates high resolution
in the nanometer scale and simultaneous thickness measurements on transparent
samples, LTSs combine high axial resolution with an extensive measurement range,
making them suitable for most in-line measurement applications [14].

Active motion compensation systems significantly reduce the effects of motion blur
and create a static measurement environment by active sample tracking. Nevertheless,
the requirement for highly accurate sample tracking sensor systems, coupled with the
constraint of being applicable primarily to piece-good production lines, considerably
narrows down their range of potential applications. Edges are often defining elements
of spatial structures. Therefore, to determine the critical width of features, the
lateral position of the feature's edges has to be determined accurately. Thus, a
measurement data correction approach is needed to mitigate motion-induced lateral
position uncertainty of edges in laser triangulation measurements on moving samples,
which leads to the first research question:

> Research Question 1
>
> Is it feasible to reduce the lateral position uncertainty of edge features in laser
> triangulation measurements on moving samples by algorithmically correcting
> the obtained measurement data?

As LTSs primarily use CCD and CMOS line sensors to detect the position of the reflected spot's COG, measurements on moving samples are prone to motion blur. The presented PSF estimation method assumes that the motion blur is constant and linear [64]. Although the produced goods in a production line mostly move at a constant and known speed, the motion of the light spot on the imaging sensor is not expected to be constant. As the position of the spot, in LTSs, depends on the sample height, the movement of the spot depends on the sample's motion and, especially, its topography. Hence, implementing the presented deblurring methods in LTS systems is not feasible since the required PSF depends on the unknown structure of the sample. A deblurring method tailored for laser triangulation measurements is still missing, posing the question:

> **Research Question 2**
>
> Is it feasible to reduce the effects of motion blur in laser triangulation measurements on moving samples by a tailored deblurring approach?

CHAPTER 3

Lateral feature uncertainty

To successfully reduce lateral uncertainty of edge feature locations, the root causes are identified and analyzed first. The main two contributors are the spatial sampling itself and motion blur, caused by the finite exposure time of the used camera.

3.1 Spatial sampling

LTSs typically use line cameras with CMOS imaging sensors to detect the reflected laser spot [65]. The frame rate and, thus, the sampling rate of the LTS is limited by the necessary exposure time of the camera. Various parameters, such as laser power, surface reflectivity, and surface orientation, affect the required exposure time. From the sensor system design point of view, the only adjustable parameter is the laser power. However, since most applications require eye-safe laser sensor systems, the laser power is limited to $1\,\mathrm{mW}$ [12], determining the minimum exposure time of the camera. The achievable sampling time, therefore, results to

$$T_{\mathrm{s}} = T_{\mathrm{exp}} + T_{\mathrm{idle}} + T_{\mathrm{cam}}, \tag{3.1}$$

with the exposure time T_{exp}, the time for internal analog-digital conversion and data processing T_{cam} and the remaining idle time T_{idle}, which is typically chosen to be zero to minimize blind spots.

A typical industrial measurement application, where a produced good is transported on a conveyor belt at a velocity v and inspected with an LTS, is schematically depicted in Fig. 3.1. The spatial sampling length Δx_s is equivalent to the distance

21
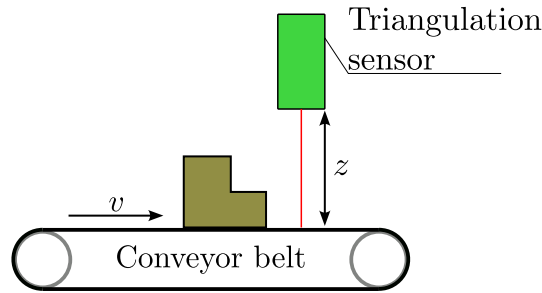
Figure 3.1: Schematic illustration of an object, containing an edge feature, passing
          by a LTS on a conveyor belt at speed v.

the sample travels during one sampling time of the LTS' detector and can therefore
be described as

$$\Delta x_s = vT_s, \tag{3.2}$$

with the sample's velocity v and the sampling time T_s. Inserting Eq. (3.1) yields

$$\Delta x_s = vT_{\text{exp}} + v\left(T_{\text{idle}} + T_{\text{cam}}\right) = \Delta x_{\text{exp}} + \Delta x_{\text{blind}}, \tag{3.3}$$

with the exposed sampel length Δx_{exp} and the blind spot length Δx_{blind}.
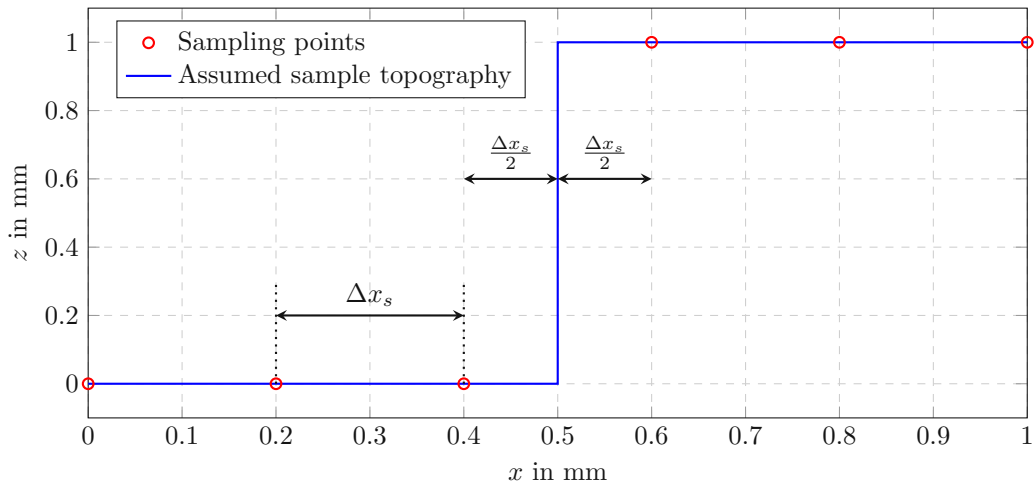
Figure 3.2: Spacial sampling induced lateral uncertainty. The blue line illustrates
          the sample topography, while the red circles mark the sampling points.
          The smallest uncertainty $\frac{\Delta x}{2}$ is achieved when the actual edge is assumed
          to be exactly between two sampling points.

An example showing lateral uncertainty caused by spatial sampling is illustrated in
Fig. 3.2. The red circles represent measurements taken at discrete locations equally

spaced in the interval of $\Delta x_\mathrm{s} = 0.2\,\mathrm{mm}$. As can be seen, the measurements at $x = 0.4\,\mathrm{mm}$ and $x = 0.6\,\mathrm{mm}$ show a significant deviation of $\Delta z = 1\,\mathrm{mm}$. Thus, it can be assumed that an edge is located between the two sampling points. However, since there is no additional measurement information between these points, the exact edge location between the sampling points is unknown. It could be located at any position between the two points. Thus, the lateral length of uncertainty is equal to the spatial sampling length Δx_s. A reasonable approach would be to assume that the edge is located exactly between the two sampling points. In this case, the possible error is minimal and in a range of $\pm\frac{\Delta x_\mathrm{s}}{2}$.

3.2 Motion blur

Another source of lateral uncertainty is motion blur. Since motion blur has different effects on the measurement results depending on the measurement principle, it has to be analyzed separately. In the case of an LTS, a change of the distance to the sample causes the spot on the camera to move laterally, as illustrated in Fig. 3.3. A measurement at a distance d_1 would yield a single intensity peak at P_1 on the detector, while a measurement at a distance d_2 would lead to a single local intensity maximum at P_2.

Considering a moving sample with an edge feature, at first, the sample's surface before the edge at a distance d_1 is illuminated by the laser, and afterward, the surface after the edge at a distance d_2 is illuminated. During the exposure of the imaging sensor, the voltage of each pixel capacitance drops depending on the light intensity and exposure time. Therefore, if the transition from d_1 to d_2 happens during one exposure time T_exp, two peaks, located at P_1 and P_2, respectively, will be detected since the pixels at both locations are exposed. A commonly used way to determine the distance to the target is to consider the highest intensity peak. Two equally high peaks would mean that the edge is located precisely in between the sampling point prior to the start of the exposure and the point after the exposure. In this case, either of the two peaks can be chosen, leading to the worst-case error explained in the following.

Fig. 3.4 depicts the worst case scenario. Note that for the sake of simplicity, in this illustration, T_cam and T_idle are assumed to be zero, i.e. $T_\mathrm{s} = T_\mathrm{exp}$. Furthermore, it is assumed that the edge is located at

$$x_\mathrm{edge} = x_{i-1} + \frac{\Delta x_\mathrm{exp}}{2} + \epsilon, \quad 0 < \epsilon < \frac{\Delta x_\mathrm{exp}}{2}, \tag{3.4}$$
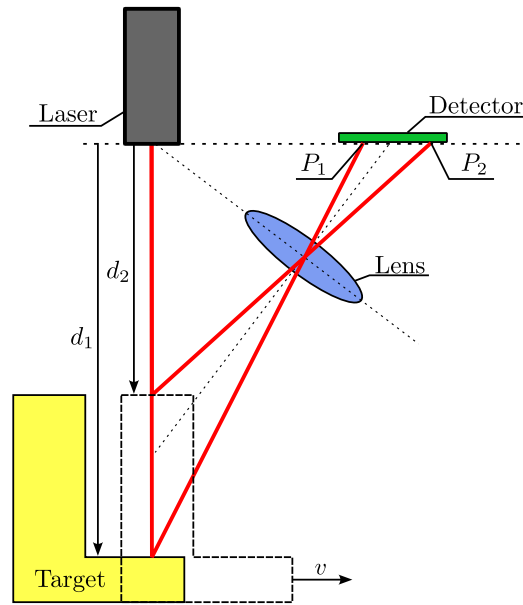
Figure 3.3: Laser triangulation on a moving sample. A change in the distance to the sample between d_1 and d_2 during one exposure time yields two local intensity maxima P_1 and P_2 at the detector.

with the index of the current sampling step i. In this case, the sample surface before the edge at the distance d_1 is exposed longer than the surface after the edge at a distance d_2. Thus, the peak at P_1 is higher than at P_2, yielding d_1 as measurement result. However, this result is wrong in the sense that the laser spot has already passed the edge, and the distance after the exposure time is d_2. The distance from the true location of the edge to the wrongly measured sampling point is denoted as Δx_b. The smaller ϵ gets, the larger the distance Δx_b gets. As ϵ approaches zero, Δx_b reaches its maximum of

$$\Delta x_\mathrm{b,max} = \frac{\Delta x_\mathrm{exp}}{2} + \Delta x_\mathrm{blind}. \tag{3.5}$$

Note that if negative values of ϵ would be allowed, the measured distance would be d_2, which decreases the position uncertainty. As in Fig. 3.4, the detected transition from d_1 to d_2 is now shifted by the distance Δx_b. At this point, the previously discussed uncertainty caused by spatial sampling has to be considered, and the edge location is estimated according to Section 3.1.

Combining the aspects of spatial sampling and motion blur, the total edge position uncertainty lies in the interval

$$
\begin{aligned}
\Delta x &\in \left(- \left(\Delta x_{exp} + \frac{3\Delta x_{blind}}{2} \right), \frac{\Delta x_s}{2} \right] \\
&= \left(- \left(v T_{\mathrm{exp}} + \frac{3}{2} v \left(T_{\mathrm{idle}} + T_{\mathrm{cam}} \right) \right), \frac{v \left(T_{\mathrm{exp}} + T_{\mathrm{idle}} + T_{\mathrm{cam}} \right)}{2} \right].
\end{aligned}
\tag{3.6}
$$

As can be seen, the uncertainty range Δx can be reduced by reducing the sample velocity v and the exposure time T_{exp}.
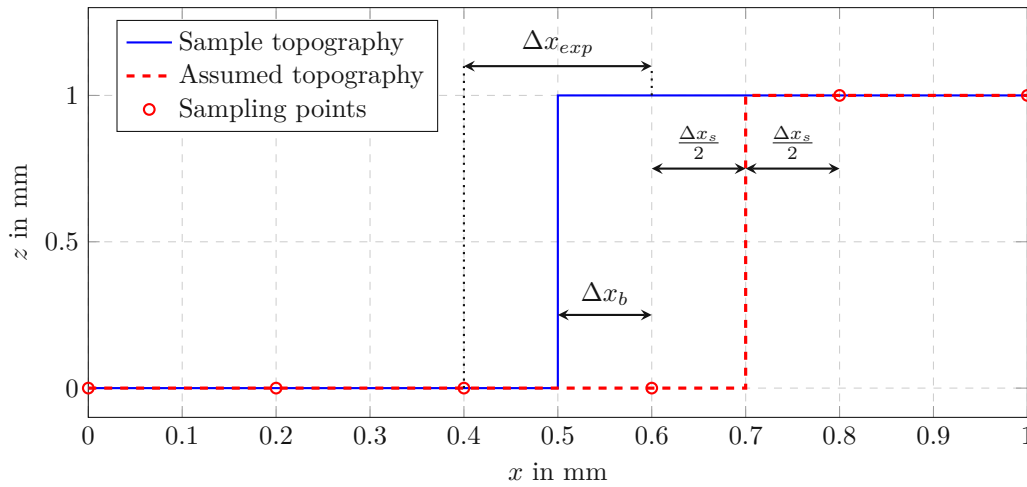
Figure 3.4: Worst case lateral uncertainty. An edge located in the center of the exposed sample length Δx_{exp} results in the largest possible lateral uncertainty.

At this point, it should be mentioned that industrially used LTSs offer a variety of multi-peak handling strategies, such as choosing the highest, first, second, or widest peak [31, 66]. Choosing either the first or second peak is only applicable for transparent multilayer samples where multiple spots are reflected from material interface layers and, therefore, is not considered in this context. The widest peak is suitable when measuring samples with varying surface conditions. This method is also disregarded as this thesis focuses on measuring samples with constant surface conditions.

CHAPTER 4

Laser triangulation sensor design

Although a large variety of industrial LTSs is available, these sensors usually do not offer the possibility to read out the entire camera data and set specific parameters, such as laser intensity or exposure time, automatically. However, to comprehensively analyze the system behavior on moving samples, all the parameters mentioned must be accessible and controllable. Therefore, a custom LTS is designed and built, enabling the adjustment of all system parameters.

4.1 Design considerations for LTS

The thin lens equation describes the optical setup in standard imaging applications, where the image plane and the plane of focus are parallel. However, these planes are non-parallel in the case of an LTS, as can be easily seen in Fig. 4.1a. The Scheimpflug and the hinge condition generalize the thin lens equation for non-parallel planes [67].

Satisfying the Scheimpflug condition ensures a constant image size of an object on the focal plane. Thus, in the case of an LTS, a constant spot size on the imaging sensor over the whole measurement range. The Scheimpflug condition is satisfied if the image plane, the lens plane, and the focal plane intersect on a single line, the Scheimpflug line, as illustrated in Fig. 4.1a.

While the Scheimpflug condition ensures a constant spot size on the imaging sensor, it does not automatically ensure that the focal plane is actually in the focus of the lens [68]. Additionally, satisfying the hinge condition solves this problem. Like the

Scheimpflug condition, the hinge condition is satisfied if three planes intersect on a single line. In this case, the focal plane, the plane that runs parallel to the image plane and through the center of the lens, and the front-focal plane, which is parallel to the lens plane and offset by the front focal length of the lens, have to intersect on the hinge line as shown in Fig. 4.1a. If those two conditions are satisfied, the spot on the camera will be focussed and of constant size over the whole measurement range.

For calibration purposes, an industrial LTS (type: optoNCDT1420, Micro-Epsilon, Ortenburg, Germany) is used as a reference. To utilize the full range and resolution of the industrial LTS, the experimental LTS should have a similar measurement range. Furthermore, the industrial and the experimental LTS' laser beams should be parallel and on the same focal plane, enabling measurements on the same lateral sample locations.

The satisfaction of the conditions mentioned above in the custom LTS design is assured by adding the planes and constraints in the CAD tool (Solidworks, Dassault Systèmes SolidWorks Corp., France) during the design of the mechanical frame. As seen in Fig. 4.1b, both conditions are satisfied, resulting in a constant sized and focussed spot of the custom LTS within the measurement range. The laser beams of the industrial and experimental LTS are on the same focal plane and the measurement ranges of both sensor systems are identical.

4.2 System components

The develped experimental LTS is displayed in Fig. 4.3. The black mechanical frame is 3D printed using a fused deposition modeling (FDM) printer, while the lens mount is printed with an stereolithography (SLA) printer due to its higher requirements for dimensional accuracy. The geometry of these parts is designed to fulfill both the Scheimpflug- and the hinge condition, which are discussed in detail in Section 4.1.

A solid-state laser (type: PL206, Thorlabs, USA), depicted in Fig. 4.2, with a wavelength of $638.8\,\text{nm}$ and output power of $0.93\,\text{mW}$ is used as a laser light source. For the sake of convenience and easier handling, the beam of the solid-state laser is coupled into an optical fiber (type: P1-630A-FC-2 Thorlabs, USA) by operating a fiber collimator (type: F280FC-B Thorlabs, USA) in the reverse direction. A second fiber collimator (type: F230FC-B Thorlabs, USA) on the output side of the optical fiber is used to generate a collimated laser beam with a waist diameter of $0.8\,\text{mm}$, that is aligned perpendicular to the target. Industrial LTSs typically use focussed laser beams to achieve smaller spot sizes on the target and hence better axial
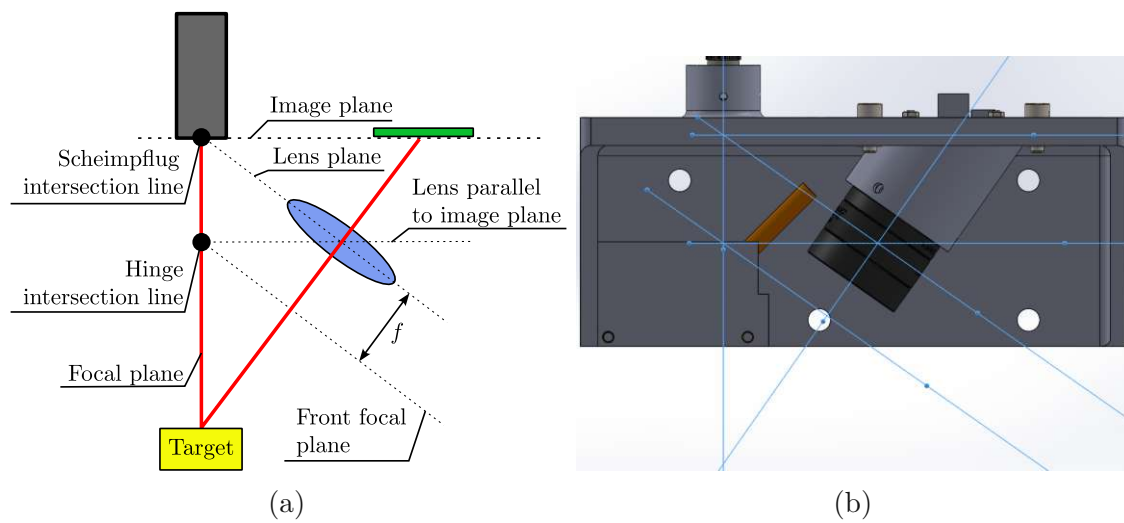
Figure 4.1: Scheimpflug and hinge condition. (a) If the image plane, lens plane, and focal plane intersect on the Scheimpflug line, the spot size on the detector is constant for the whole focal plane. If the focal plane, front focal plane, and parallel to lens plane intersect on the hinge line as well, the focal plane is also focused on the detector. (b) shows the satisfaction of the two conditions in the CAD design.

resolution [26]. However, the choice of a collimated beam is deliberately made to simplify the sample illumination modeling and feature position correction procedure (see Chapters 5 and 6).

A bi-convex lens (type: LB1761-A-ML, Thorlabs, USA) with a focal length of $f = 25.4$ mm is used to focus the reflected laser spot on the detector. As a detector, a CMOS board camera (type: DMM 37UX273-ML, The Imaging Source, USA) with a resolution of 1,440x1,080 pixels and a pixel pitch of 3.45 µm is used. The global shutter prevents artifacts caused by the sample's movement during readout, as they would appear in rolling shutter imaging sensors. Furthermore, the shutter time is adjustable between 1 µs and 30 s, which makes it perfectly suitable for various laser powers and sample reflectivities. The image data is transferred to a computer via a USB 3.1 interface. Industrial LTS typically use line cameras instead of 2D imaging sensors since the reflected spot moves along a line as the sample displacement changes. Thus, a large area of the used 2D imaging sensor is unused, producing excessive image data. Therefore, a ROI is defined on the imaging sensor, limiting the resolution to 1,440x500 pixels, with the window starting at the 400th vertical pixel.
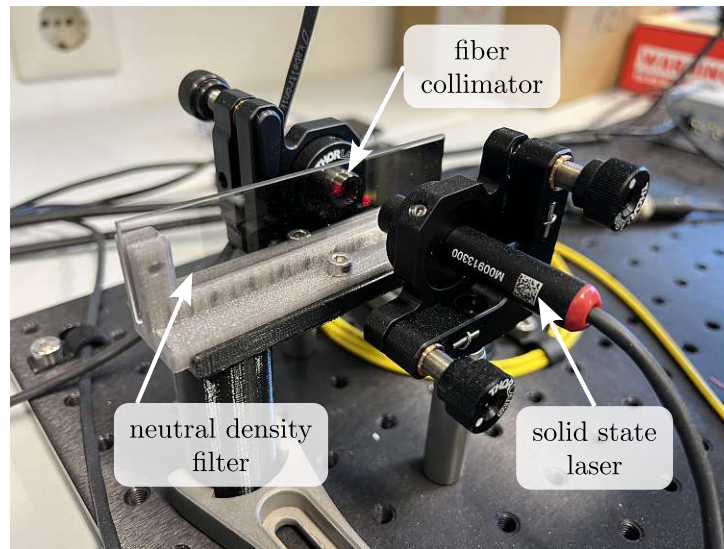
Figure 4.2: Laser coupling. The beam from the solid-state laser is coupled to the optical fiber using a fiber collimator. The neutral-density filter allows adjustments of the laser power.

3D printed test samples, as illustrated in Fig. 4.4, are used to test the lateral edge position correction performance. The samples are printed using an SLA printer with a pixel pitch of $50\,\mu m$ to create sharp edges on the sample. To move the sample past the LTS, a linear stage (type: VT-80, Physik Instrumente GmbH & Co. KG, Germany) with a top speed of $v = 20\,\mathrm{mm\,s^{-1}}$ is used. Although the maximum achievable speed of the linear stage is much smaller than the maximum speed in industrial production lines, which can reach up to speeds of $10\,\mathrm{m\,s^{-1}}$, its positioning accuracy of $\pm 10\,\mu m$ and constant travel speed makes additional lateral position sensors obsolete, which substantially decreases the system complexity. Furthermore, as discussed in Chapter 3, the lateral feature position uncertainty Δx highly depends on the distance the sample travels during the exposure. Increasing the exposure time T_{exp} can compensate for the small sample velocity v as shown in Eq. (3.6). The linear stage and the camera can be operated using Matlab (The MathWorks, USA).

4.3 Dimensionality reduction using PCA

The phrase "the curse of dimensionality," introduced by Richard Bellman [69], describes the extraordinary rapid growth of complexity in problems as the number of dimensions increases [70]. Since this is a common problem in the field of machine
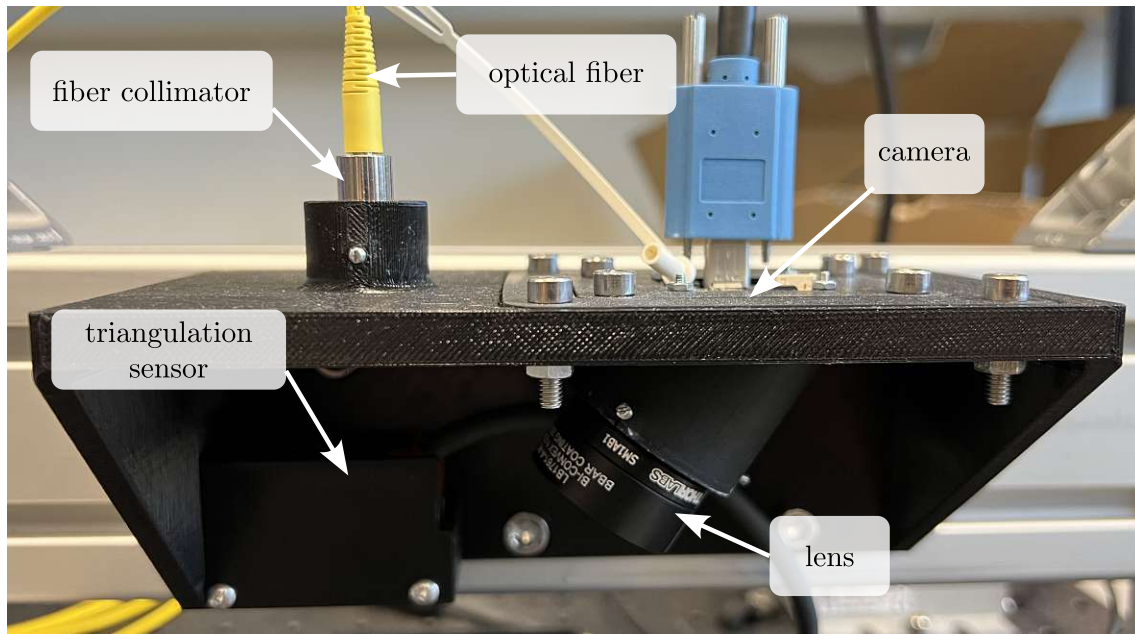
Figure 4.3: Experimental LTS. The optical fiber and the fiber collimator offer a collimated laser beam, which is orientated perpendicular to the target. The lens focuses the reflected spot on the CMOS camera chip. An industrial LTS is used for calibration purposes.

learning and data science [71], a variety of dimensionality reduction (DR) algorithms, such as principal component analysis (PCA), independent component analysis (ICA) or linear discriminant analysis (LDA) are well known and often used [72]. For normally distributed data, PCA is the most applicable since its problem formulation is based on Gaussian distributions [73, 74].

An axial displacement of the sample leads to a lateral movement of the laser spot on the camera, as discussed in Section 2.1.2. That means only one-dimensional information is needed from the camera for displacement measurements. Since a 2D CMOS imaging sensor is used in the custom LTS as described in Section 4.2, all the information spread along the axis perpendicular to the spot's axis of motion is redundant. Hence, DR from 2D to 1D of the sensors pixel-information is appropriate. A simple and computationally efficient DR approach is to use a linear transformation

$$\boldsymbol{\xi} = \mathbf{w}^{\mathrm{T}}\mathbf{X}, \quad \boldsymbol{\xi} \in \mathbb{R}^{1 \times n}, \mathbf{w} \in \mathbb{R}^2, \mathbf{X} \in \mathbb{R}^{2 \times n}, \|\mathbf{w}\| = 1, \tag{4.1}$$

where the transformation vector $\mathbf{w}$ transforms a number of n 2D coordinates $\mathbf{X}$ to n 1D coordinates $\boldsymbol{\xi}$. The transformation vector is chosen as a unity vector, so the
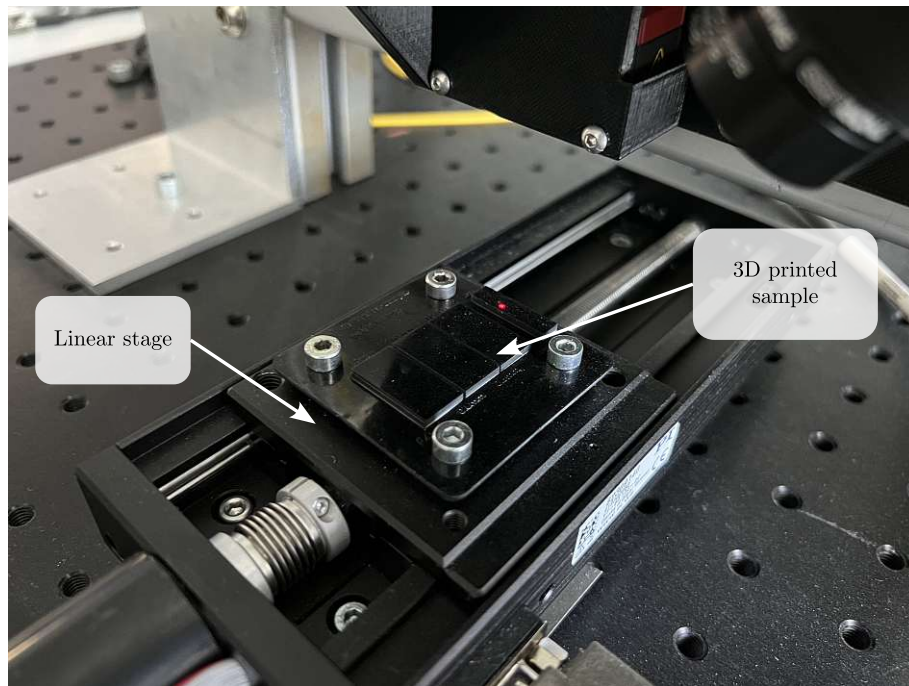
Figure 4.4: Moving sample. The 3D-printed sample is mounted on a linear stage, which allows linear motion with precise velocity.

transformation is scale invariant. Fig. 4.5 illustrates the DR principle using PCA. The normalized first principle component $\mathbf{w}_1$ depicted in Fig. 4.5a is used as the transformation vector. Note that the two principal components of the scattered data are orthogonal. Applying Eq. (4.1) yields the transformed data ξ, as shown in Fig. 4.5b. As can be seen, the scattered data gets projected on the axis of the highest variance, and thus, the projected data contains the maximum information.

Since the laser's spot profile is Gaussian, the spot on the camera will also be normally distributed, which makes PCA the most suitable DR technique to determine the transformation vector $\mathbf{w}$. Since PCA is primarily used in data science and machine learning, it is typically formulated for a set of scattered data containing n samples, where each sample has m features, and the transformed n samples have k features, where $k < m$. An image can also be interpreted as scattered data, having two features, its pixel coordinates (a, b). The pixel values $I_{\mathrm{px}}(a, b)$ can be interpreted as the frequency of respective data points at the coordinates (a, b). As the primary method for scattered data and image data is the same, it is first discussed for scattered data and subsequently extended for image data.
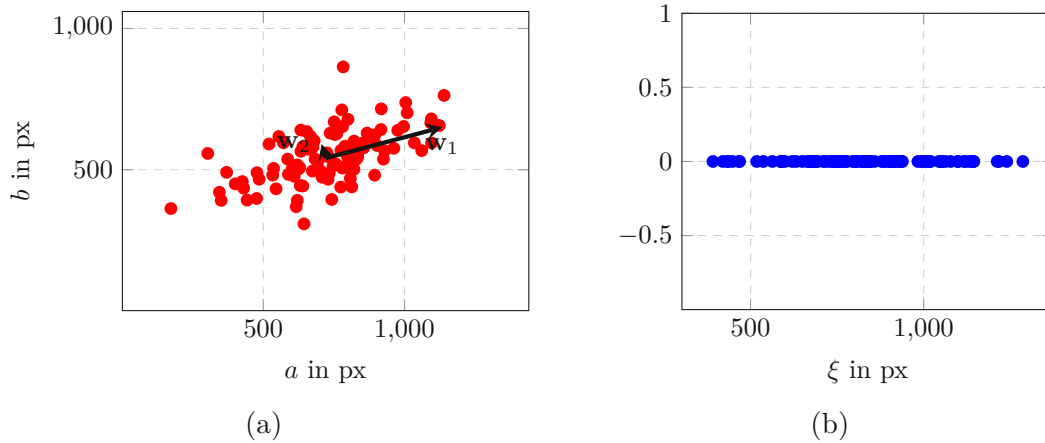
Figure 4.5: Dimensionality reduction of 2D scattered data. (a) shows 2D scattered data points and its two principal components $\mathbf{w}_1$ and $\mathbf{w}_2$. The result, after transforming the data onto the first principal axis $\mathbf{w}_1$, is depicted in (b).

Given a dataset $\mathbf{X} \in \mathbb{R}^{m \times n}$, with n samples, consisting of m features each, a transformed data set $\xi \in \mathbb{R}^{1 \times n}$ in a one-dimensional feature space is obtained by applying Eq. (4.1). The transformation vector $\mathbf{w}$ is determined by solving the optimization problem

$$\mathbf{w} = \underset{\|\mathbf{w}\|=1}{\operatorname{argmax}} \operatorname{var}\left(\boldsymbol{\xi}\right), \tag{4.2}$$

which maximizes the variance, and thereby the information, of the transformed data $\boldsymbol{\xi}$ [75]. The mean value of the transformed data vector can be calculated as

$$\mu_\xi = \frac{1}{n} \sum_{i=1}^{n} \mathbf{w}^{\mathrm{T}} \mathbf{X}_i = \mathbf{w}^{\mathrm{T}} \boldsymbol{\mu_{\mathbf{X}}}, \tag{4.3}$$

with the mean value of the initial data $\boldsymbol{\mu_{\mathbf{X}}}$. Using Eq. (4.1) and Eq. (4.3), the variance of the transformed data is given as

$$
\begin{aligned}
\operatorname{var}\left(\boldsymbol{\xi}\right) &= \frac{1}{n} \sum_{i=1}^{n} \left(\boldsymbol{\xi}_i - \mu_\xi\right)\left(\boldsymbol{\xi}_i - \mu_\xi\right)^{\mathrm{T}} \\
&= \frac{1}{n} \sum_{i=1}^{n} \left(\mathbf{w}^{\mathrm{T}} \mathbf{X}_i - \mathbf{w}^{\mathrm{T}} \boldsymbol{\mu_{\mathbf{x}}}\right)\left(\mathbf{w}^{\mathrm{T}} \mathbf{X}_i - \mathbf{w}^{\mathrm{T}} \boldsymbol{\mu_{\mathbf{x}}}\right)^{\mathrm{T}} \\
&= \mathbf{w}^{\mathrm{T}} \mathbf{S} \mathbf{w},
\end{aligned}
\tag{4.4}
$$

with the covariance matrix of the initial data $\mathbf{S}$. Thus, the optimization problem given in Eq. (4.2) can be solved by finding the solution of

$$\frac{\partial}{\partial \mathbf{w}} \left(\mathbf{w}^{\mathrm{T}} \mathbf{S} \mathbf{w} + \lambda \left(1 - \mathbf{w}^{\mathrm{T}} \mathbf{w} \right) \right) = 0, \tag{4.5}$$

with λ being the Lagrangian multiplier. Solving the partial derivative and rearranging yields the eigenvalue problem

$$\mathbf{S} \mathbf{w} = \lambda \mathbf{w}. \tag{4.6}$$

Therefore, the transformation vector $\mathbf{w}$ can be found by solving the eigenvalue problem given in Eq. (4.6). Using the eigenvector corresponding to the largest eigenvalue λ as the transformation vector $\mathbf{w}$ maximizes the variance of ξ. If the transformed data should have k features, the eigenvectors of the first k eigenvalues are combined in a transformation matrix $\mathbf{W} = [\mathbf{w}_1 ... \mathbf{w}_k]$, yielding the linear transformation

$$\boldsymbol{\xi} = \mathbf{W}^{\mathrm{T}} \mathbf{X}, \quad \boldsymbol{\xi} \in \mathbb{R}^{k \times n}, \mathbf{W} \in \mathbb{R}^{m \times k}, \mathbf{X} \in \mathbb{R}^{m \times n}, k < m. \tag{4.7}$$

Image data can be interpreted as scattered data, where the pixel value $I(u, v)$ is the frequency of occurrence of the respective datapoint at the coordinates (u, v). Therefore, the total number of points is not described by the total number of pixels on the imaging sensor but by the total sum of pixel values given as

$$N = \sum_{u=1}^{n_u} \sum_{v=1}^{n_v} I(u, v), \tag{4.8}$$

with the number of rows n_u and the number of columns n_v. The mean value μ of the image data is given by

$$\boldsymbol{\mu} = \frac{1}{N} \sum_{u=1}^{n_u} \sum_{v=1}^{n_v} \begin{bmatrix} u \\ v \end{bmatrix} I(u, v), \tag{4.9}$$

where, again, each pixel is weighted by its frequency $I(u, v)$. Similarly, the covariance matrix $\mathbf{S}$ can be calculated by weighting each addend by its frequency, yielding

$$\mathbf{S} = \frac{1}{N} \sum_{u=1}^{n_u} \sum_{v=1}^{n_v} I(u, v) \left(\begin{bmatrix} u \\ v \end{bmatrix} - \boldsymbol{\mu} \right)^2. \tag{4.10}$$

The transformation vector $\mathbf{w}$ is obtained by solving the eigenvalue problem formulated in Eq. (4.6) for the covariance matrix derived in Eq. (4.10).

4.3.1 Identification of the principle component and transformed pixel coordinates

In the case of an LTS, the axis of interest is the axis the spot moves along on the camera due to an axial displacement of the sample. Therefore, in the first step, data on spot positions for various axial displacements has to be acquired. A linear stage (type: X-VSR20A-SV2, Zaber, Canada) operated in z-direction acts as sample with adjustable height, as shown in Fig. 4.6.
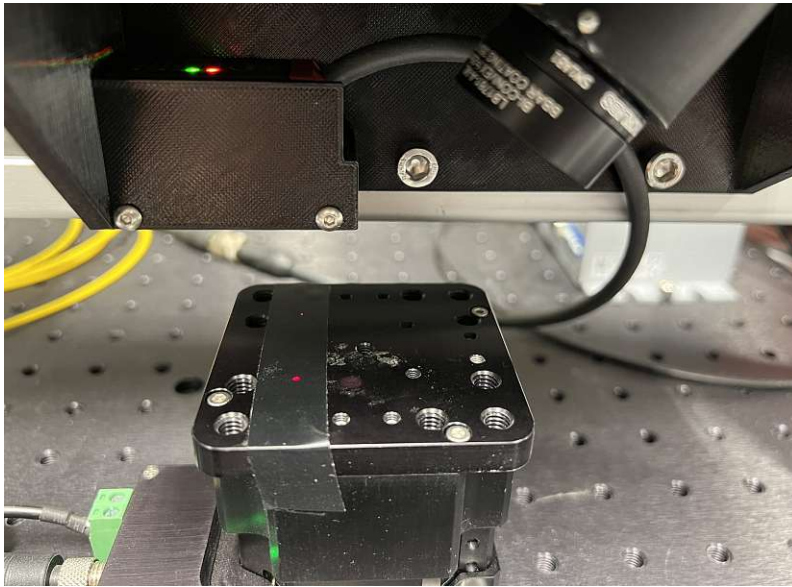
Figure 4.6: Calibration setup. The linear z-stage acts as an adjustable sample. Both spots of the industrial LTS are visible.

One hundred images for equally spaced displacements within the measurement range are taken to acquire data over the full spot movement range. These pictures are converted to real-valued images and added to obtain one cumulative image representing the spot distribution over the full measurement range as depicted in Fig. 4.7. The first principal component is determined by applying the procedure described in Section 4.3, yielding the transformation vector

$$\mathbf{w} = \begin{bmatrix} 0.9999 \\ 0.0111 \end{bmatrix}, \quad \|\mathbf{w}\| = 1. \tag{4.11}$$
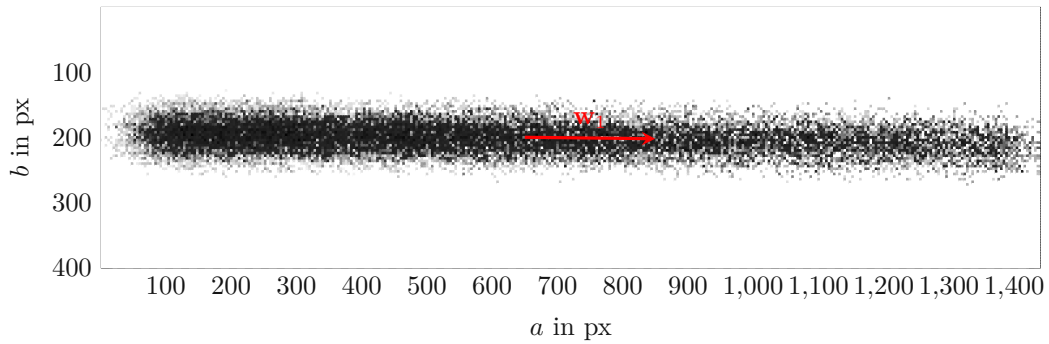
Figure 4.7: Cummulative image of the spots movement. The first principle component is almost parallel to the *a*-axis.

The new 1D pixel coordinates ξ are obtained using Eq. (4.1). All possible 2D pixel coordinate combinations are combined in the matrix $\mathbf{X}$ as

$$\mathbf{X} = \begin{bmatrix} 1 & \dots & n_u & 1 & \dots & n_u \\ 1 & \dots & 1 & 2 & \dots & n_v \end{bmatrix}, \quad \mathbf{X} \in \mathbb{R}^{2 \times n_u n_v}, \tag{4.12}$$

yielding a 1D coordinate vector ξ of length $n_u n_v$. The entries of ξ are subsequently sorted in ascending order. The sorted coordinates, as well as the sorted indices of ξ prior to sorting, are saved.

A raw 2D image as depicted in Fig. 4.9a can now be transformed into a 1D representation by reshaping the 2D data to a vector and sorting the entries according to the coordinate vector's previously saved sorted indices. The resulting image is displayed in Fig. 4.9b. While the Gaussian intensity profile is visible, the plot looks like an area plot. The transformation causes this artifact. Since all pixel coordinates get transformed on the first principal axis, and all pixel values are assigned to the new coordinates, pixel values from outside the spot, with a low intensity value, get projected between pixels of the actual spots. This leads to periodically appearing low intensity values between the high intensity values of the spot.

Furthermore, due to the angle of the projection axis, the transformed pixel coordinates are not equidistantly spaced along the axis, which can lead to complications described in Section 5.2. Equidistantly spaced data points are desired to make the 1D image applicable for operations like linear filtering. This is achieved by binning the pixel coordinates into equidistant bins with a distance of 1 between the respective bins. All pixel values within one bin are summed up, resulting in the image shown in Fig. 4.9c. As one can see, the Gaussian intensity profile is still clearly visible. The noise in the intensity profile is mainly caused by speckles. While there exist methods to reduce speckle noise, e.g., by integrating a moving diffuser mechanism in the optical path

[30], such methods are not considered in this work as they would exceed the scope of this thesis.

As discussed above and visible in Fig. 4.7, the projection axis is not precisely parallel to either of the two coordinate axes. This is caused by a rotational alignment error of the camera in the experimental LTS. Transforming the pixel data onto the projection axis, the motion axis of the spot, compensates for this error, making the 2D camera act as a perfectly aligned line camera.

4.4 Data driven system calibration

Since the relation between sample displacement and spot position on the camera is non-linear (see Chapter 2) and alignment errors caused by manufcaturing uncertainties cannot be neglected, a data-driven calibration approach is chosen to map the spot's COG to a displacement value. The COG of the spot is calculated similar to Eq. (4.3) as

$$\text{CoG} = \frac{1}{n_u n_v} \sum_{i=1}^{n_u n_v} \xi_i I(\xi_i). \tag{4.13}$$

Note that not the binned 1D image is used to calculate the COG, but the full resolution 1D image (as in Fig. 4.9b) since the variable distance between pixel coordinates and the low intensity pixels between the high intensity spot pixels do not corrupt the calculation of the COG.
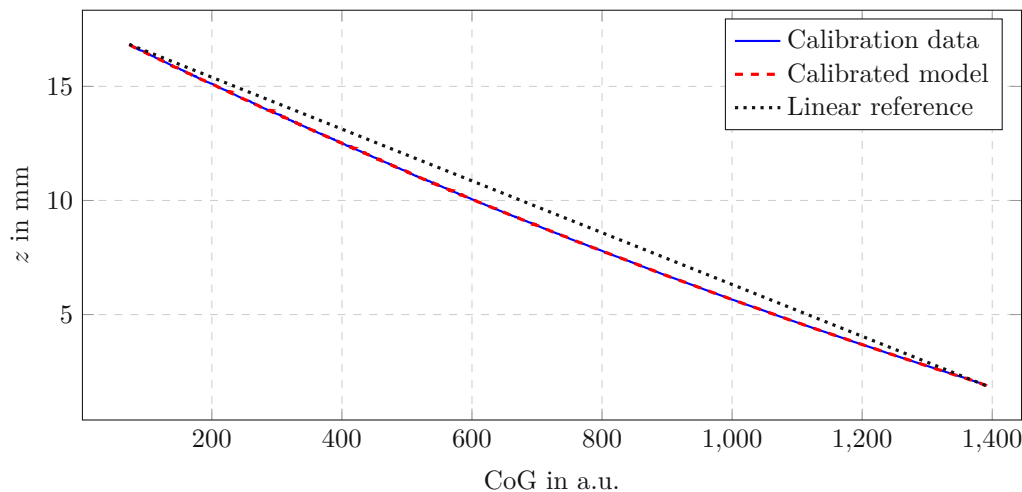
Figure 4.8: System calibration results. The red dashed cubic spline model fits the measurement data obtained by the industrial LTS.

The same setup as explained in Fig. 4.6 is used for the calibration procedure. An industrial LTS (type: optoNCDT1420, Micro-Epsilon, Germany) serves as a reference, providing the ground-truth for displacement in z. Over a displacement range of $15\,\mathrm{mm}$ 1000 measurements are taken. The displacement z over the COGs are shown in Fig. 4.8 in solid blue. Using Matlab's curve fitting toolbox, a cubic spline model

$$z = \mathcal{M}\left(\mathrm{CoG}\right) \tag{4.14}$$

is fitted to the calibration data. The resulting model is illustrated as a dashed red line in Fig. 4.8. Looking at the dotted black linear reference, the nonlinearity of the sensor system is clearly visible.
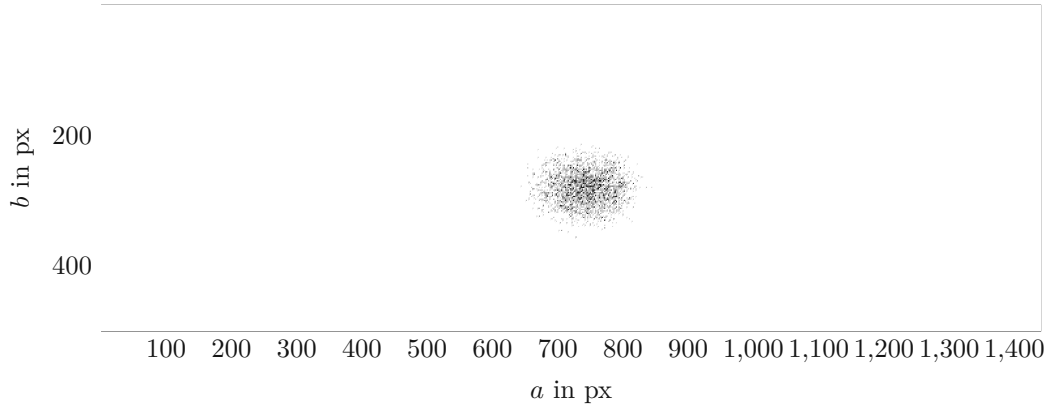
(a) Raw image of the laser spot on the camera.
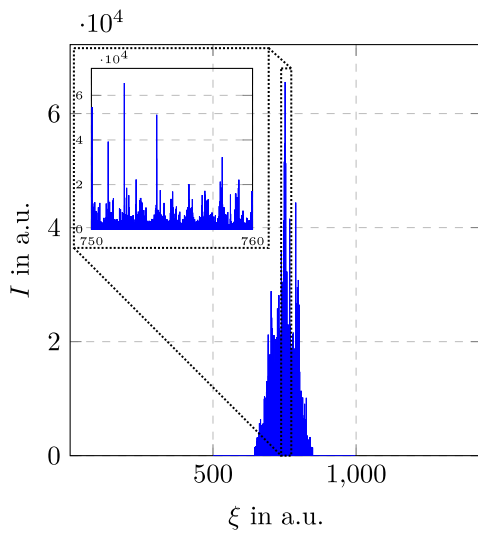
(b) Image data transformed into new pixel coordinates ξ.
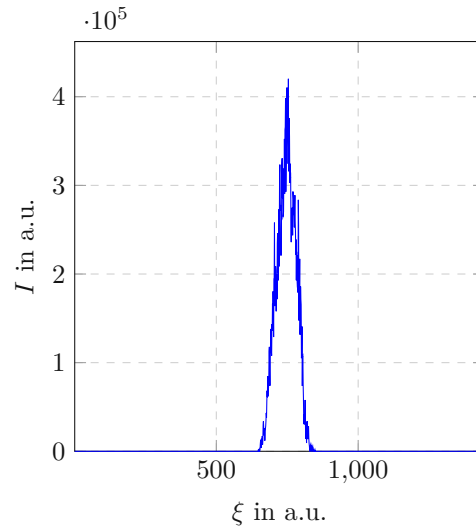
(c) Binned transformed image data

Figure 4.9: DR of real image data. (a) depicts the raw image data of the laser spot on the camera. The coordinate transformation yields the 1D representation of the image in new pixel coordinates ξ as shown in (b). The obtained equidistant pixel coordinates of the transformed data is binned, yielding the results depicted in (c).

CHAPTER 5

Analysis of measurements on edge features

Before analyzing measurements on moving samples, the effects of measuring statically on a sharp edge are investigated in the first step. Since the raw image data and the transformed 1D image data are affected by noise caused by speckling, image transformation, and binning, two ways for denoising and describing the obtained intensity distribution are discussed. Subsequently, the causes for the obtained intensity distribution are investigated and modeled.

5.1 Static measurements

A 3D printed structure containing a sharp edge with a height of $2\,\mathrm{mm}$ is used as a sample. As the laser spot moves over the edge, both the upper (d_1) and lower (d_2) part of the structure, prior to and after the edge, get illuminated by the laser as illustrated in 5.1a. Therefore, two areas on the imaging sensor correspond to the respective heights and are expected to be illuminated by the reflected light as depicted in 5.1b. The higher the edge, the larger the separation between the two points. Looking at 5.1b, an offset in the v direction between the two reflected spots (P_1 and P_2) is visible. This is not caused by misalignments but by the geometric arrangement of the components. The red dotted lines indicate the path of the reflected light, showing the offset in the v direction of the sample's surface before and after the edge.

The result of an actual measurement on the sample's edge is shown in Fig. 5.2. Two spots with their COGs representing the sample's surface height are visible in
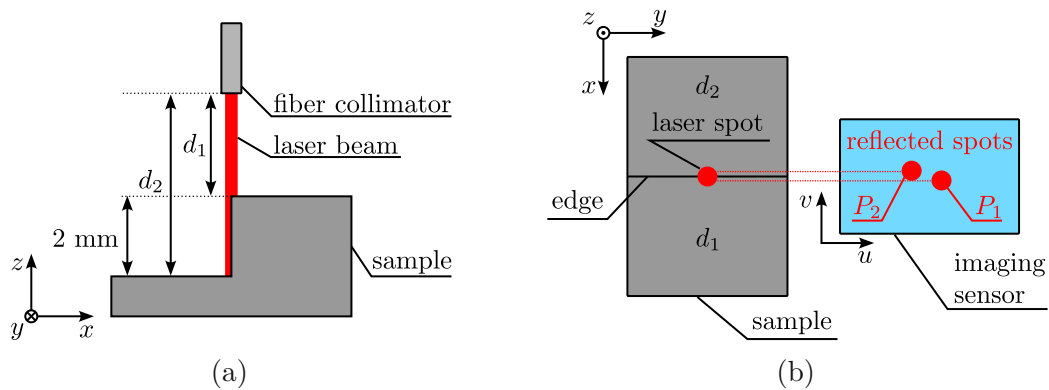
Figure 5.1: Schematic illustration of a measurement on an edge. (a) shows the laser illuminating the sample's surface before and after the edge. (b) Two spots, with an offset in v direction, are reflected onto the imaging sensor.

Fig. 5.2a. As shown in Fig. 4.8, a COG at a lower pixel coordinate corresponds to a smaller sample height. Hence, the spot on the left in Fig. 5.2a results from a smaller sample height than the spot on the right. The spot on the right side being offset to higher v coordinates than the left spot indicates that the area of a larger sample height is located at a larger x coordinate than the area of a smaller sample height. This corresponds to the schematic illustration in Fig. 5.1.

When the sample is moved past the LTS, the surface at d_1 is illuminated, resulting in a spot P_1 on the imaging sensor. After the edge passed the LTS, a spot P_2, corresponding to d_2, will be detected on the imaging sensor. During the transition, i.e., when measuring on the edge, there is no smooth transition from P_1 to P_2 on the imaging sensor. Since the u axis represents axial displacements in the z direction and the measurement is performed on a sharp edge, spot P_2 appears, and spot P_1 disappears as the sample moves. The intensity on the sensor is dependent on the laser intensity the respective sample area is exposed to, since only the reflected light from the sample's surface is detected on the imaging sensor.

The two spots are appearing as intensity peaks in the transformed 1D image in Fig. 5.2b. Speckling, caused by the coherent light source, mainly contributes to the considerable measurement noise. The image transformation itself also contributes to the noise, as discussed in Section 4.3.1. However, by binning the unevenly spaced transformed pixel coordinates to evenly spaced intervals and summing up the pixel values within the bins, this effect can be mitigated to a large extent. To reduce the speckle noise and to describe the obtained intensity distribution, further data processing steps are necessary.

(a) Raw 2D camera image

(b) Transformed 1D image
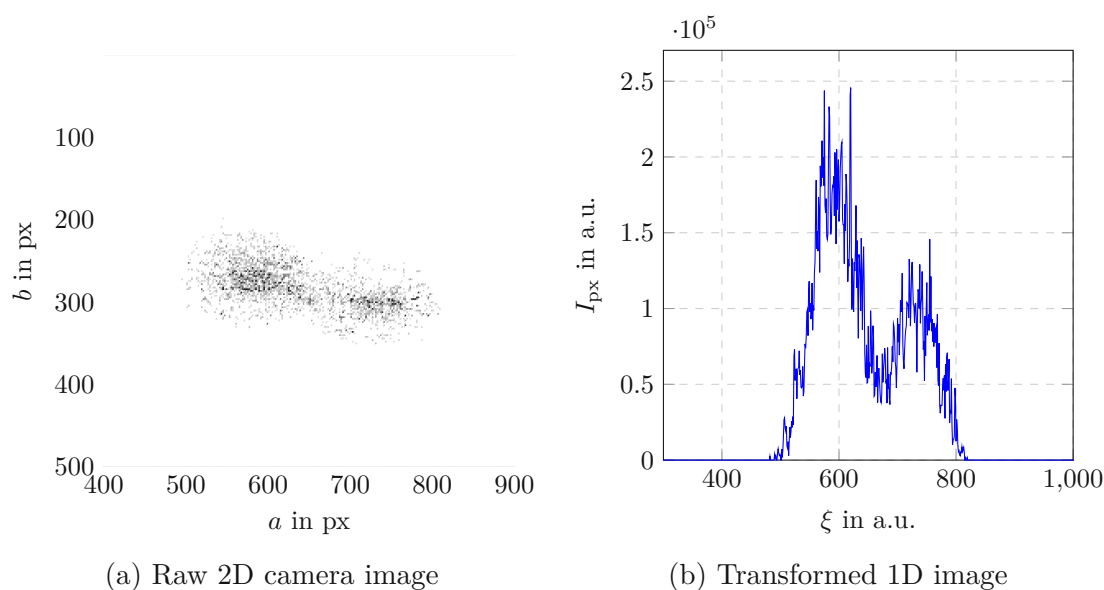
Figure 5.2: Image data taken on a sharp edge. (a) shows the raw 2D image obtained by the imaging sensor. Two spots, each representing one side of the edge, are visible. The transformed image in (b) also shows two visible double peaks. Both peaks appear to have Gaussian shapes.

5.2 Description of the intensity distribution

Since the fiber collimator at the optical fiber output emits a collimated beam with a Gaussian intensity profile, it is a reasonable assumption that the intensity profile on the imaging sensor will also be normally distributed. This assumption is further backed up by the intensity distribution shown in Fig. 5.2b. It appears to be the combination of two Gaussian normal distributions. Therefore, Gaussian models are chosen to describe the intensity profile on the imaging sensor. Additionally, a matched filter approach is discussed, as a complete model of the intensity profile is not always needed to correct the lateral edge position.

5.2.1 Gaussian modelling

Choosing the suitable Gaussian model to describe the obtained data from the imaging sensor is crucial for the subsequent feature position correction step (see Chapter 6). As shown in Fig. 5.2, when measuring on an edge, the intensity profile in Fig. 5.2b has the shape of two superimposed Gaussian distributions. On the other hand, when measuring on a flat surface as shown in Fig. 5.3, the intensity profile can be described as one single Gaussian distribution. Therefore, when fitting a Gaussian model to the

(a) Raw 2D image

(b) Transformed 1D image
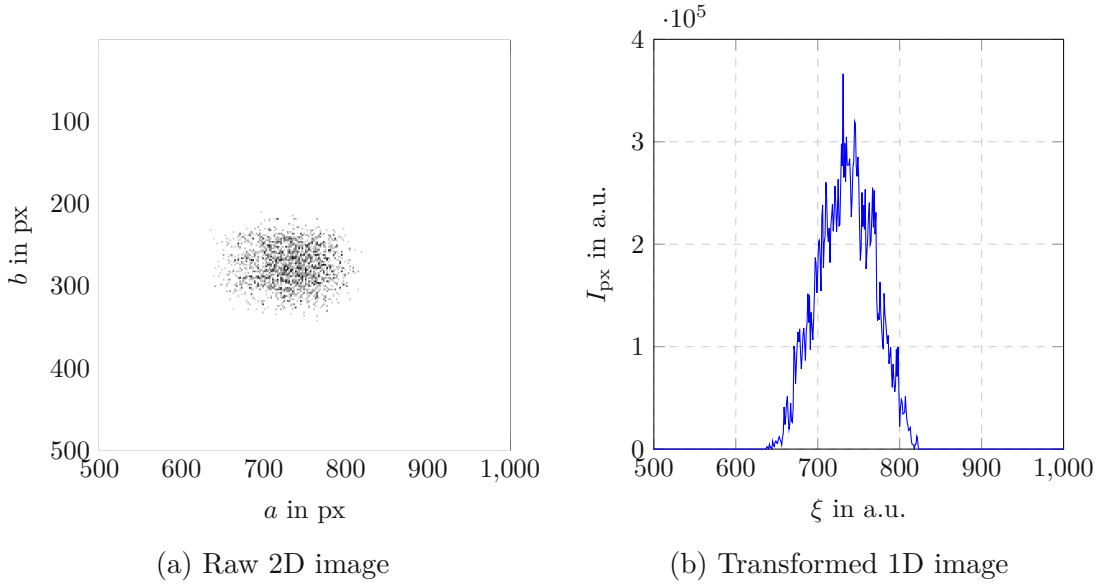
Figure 5.3: Spot profile obtained from a flat surface measurement. (a) shows the raw 2D data from the imaging sensor, while the transformed and binned 1D image is displayed in (b).

image data, it is first modeled as a single Gaussian normal distribution

$$\mathcal{N}\left(x|\mu,\sigma\right) = \frac{1}{\sigma\sqrt{2\pi}} e^{-\frac{1}{2}\left(\frac{x-\mu}{\sigma}\right)^2}. \tag{5.1}$$

The mean value μ and the standard deviation σ are the parameters to be estimated.

5.2.1.1 Gaussian model on flat surfaces

The parameters μ and σ appear nonlinearly in the Gaussian normal distribution given in Eq. (5.1). Therefore, a nonlinear optimization problem must be solved to estimate these parameters. One approach would be to minimize the squared error of the measured intensity distribution on the imaging sensor and the modelled distribution. Another possibility would be to tackle the problem from a probabilistic theory point of view. Both approaches are discussed and compared in the following.

Nonlinear least squares (NLSQ) fit
The parameters can be estimated by minimizing the squared deviation between the obtained image data and the modeled intensity distribution. In general, the

optimization problem [76]

$$\boldsymbol{\Theta} = \underset{\boldsymbol{\Theta}}{\operatorname{argmin}} J\left(\mathbf{I}(\boldsymbol{\xi}), \boldsymbol{\xi}, \boldsymbol{\Theta}\right), \tag{5.2}$$

has to be solved for the parameters

$$\boldsymbol{\Theta} = \begin{bmatrix} \mu \\ \sigma \\ d \\ g \end{bmatrix}. \tag{5.3}$$

The sum of squared errors between the image data and the intensity model is used as the cost function

$$J\left(\mathbf{I}(\boldsymbol{\xi}), \boldsymbol{\xi}, \boldsymbol{\Theta}\right) = \frac{1}{2}\left(\mathbf{I}(\boldsymbol{\xi}) - \left(d + g\mathcal{N}\left(\boldsymbol{\xi}|\mu, \sigma\right)\right)\right)\left(\mathbf{I}(\boldsymbol{\xi}) - \left(d + g\mathcal{N}\left(\boldsymbol{\xi}|\mu, \sigma\right)\right)\right)^{\mathrm{T}}. \tag{5.4}$$

Despite the Gaussian normal distribution in Eq. (5.1) having only the two parameters, μ, and σ, to be estimated, two additional parameters d and g are needed for the NLSQ. The Gaussian normal distribution $\mathcal{N}\left(\boldsymbol{\xi}|\mu, \sigma\right)$ is normalized to have a total area of 1. Thus, the additional parameter g is used as a gain factor to match the image data. Offsets caused by dark currents of the sensor and background illumination are compensated for by the offset parameter d. This doubles the dimensionality of the optimization problem, excessively increasing the complexity of the problem [69, 77], which is a significant drawback of this approach. Furthermore, the choice of initial values for the optimization algorithm significantly impacts the convergence properties of the NLSQ fit. A suitable choice of initial parameters $\boldsymbol{\Theta}_0$, which chooses them already close to the optimal value is

$$\mu_0 = \underset{\xi}{\operatorname{argmax}}\left(I\left(\xi\right)\right), \tag{5.5a}$$

$$\sigma_0 = 35, \tag{5.5b}$$

$$d_0 = 0, \tag{5.5c}$$

$$g_0 = \frac{\max\left(I\left(\xi\right)\right)}{\mathcal{N}\left(\mu_0|\mu_0, \sigma_0\right)}. \tag{5.5d}$$

The initial mean value μ_0 is the pixel coordinate ξ at which the highest intensity value occurs. The initial standard deviation value $\sigma_0 = 35$ is chosen based on empirically determined values for the experimental setup configuration. Since the offset errors cannot be determined and are expected to be minor, a zero value is chosen for the initial offset d_0. The initial gain g_0 is chosen, such that the maximum value of the initial Gaussian model and the maximum measured intensity are equal.

Fig. 5.4 shows the results of NLSQs fits. As one can see, if the initial parameters are chosen according to Eq. (5.5), the model fits the image data very well. However, if the initial values deviate too much from the optimal values, the optimization algorithm converges to a local minimum, which does not fit the image data satisfactorily. As displayed in Fig. 5.4 an initial standard deviation of $\sigma_0 = 60$ results in the red dotted line, which mean value fits the image data, but the standard deviation converged to an even larger value. For measurements on perfectly flat surfaces with known constant illumination and surface conditions, the nominal standard deviation σ_0 can be determined empirically, as done in Eq. (5.5). If, for example, the surface condition, such as the sample's reflectivity, changes or if the sample is slightly tilted, the obtained intensity profile on the imaging sensor would show a larger standard deviation. As these conditions are not known during the NLSQ fit, it would lead to a significant deviation between the initial values of the optimization parameters $\mathbf{\Theta}_0$ and the true parameters, and thus, leading to a poor NLSQ fit performance. Therefore, this approach only applies under well-known conditions, which cannot be guaranteed, especially in detecting defects in produced goods.
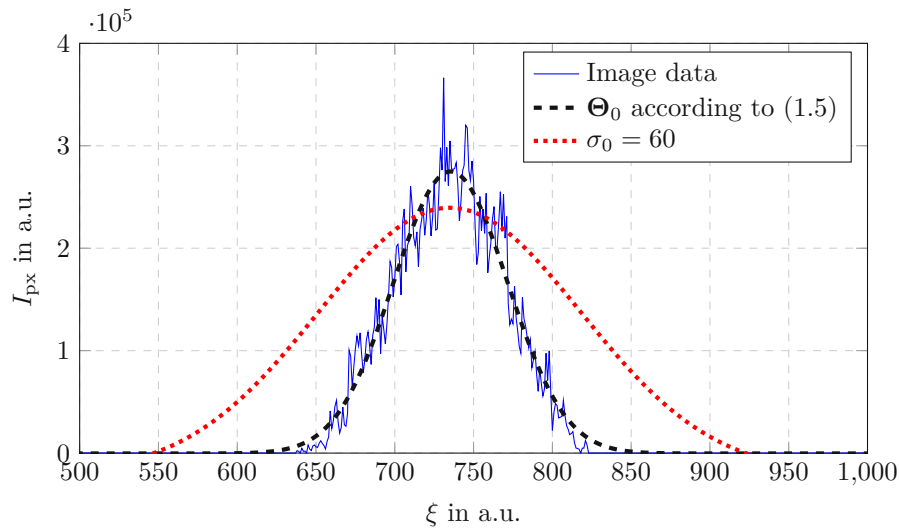
Figure 5.4: Result of an NLSQ fit on a flat surface measurement. The choice of initial parameters has a significant impact on the convergence properties. The dashed black line shows the result for initial values that are close to the optimum, while the red dotted line shows the bad result for a standard deviation chosen too large.

Maximum likelihood estimation (MLE)
To overcome the previously discussed drawbacks of NLSQ fits for Gaussian models,

an approach that incorporates probabilistic theory methods is discussed in this section. An efficient way to estimate the parameters of Gaussian distributions is the maximum likelihood estimation (MLE) [77, 78]. It maximizes the probability of a set of datapoints $\mathbf{X}$ containing N samples, given the parameters $\mathbf{\Theta} = [\mu, \sigma]^{\mathrm{T}}$. It is assumed that the data points are normally distributed. Therefore, the probability of a single datapoint x_n, given the parameters μ and σ, is obtained using Eq. (5.1). To get the probability of the whole dataset $\mathbf{X}$, the joint probability is given by the product of single datapoint probabilities as

$$p\left(\mathbf{X}|\mu, \sigma\right) = \prod_{n=1}^{N} \mathcal{N}\left(x_n|\mu, \sigma\right), \tag{5.6}$$

assuming that the probabilities of the data points x_n are independent. Since the probability density function (PDF) given in Eq. (5.1) contains an exponential function, it is convenient not to maximize the joint probability in Eq. (5.6), but to maximize the loglikelihood function

$$
\begin{aligned}
l(\mathbf{\Theta}) &= \ln p\left(\mathbf{X}|\mathbf{\Theta}\right) \\
&= \ln \prod_{n=1}^{N} \mathcal{N}\left(x_n|\mu, \sigma\right) \\
&= \sum_{n=1}^{N} \left\{ -\ln\left(\sigma\sqrt{2\pi}\right) - \frac{1}{2\sigma^2}\left(x_n - \mu\right)^2 \right\},
\end{aligned}
\tag{5.7}
$$

instead, as the exponential function gets eliminated. This is valid since the natural logarithm is a strictly monotonically increasing function. The optimization problem

$$\mathbf{\Theta} = \underset{\mathbf{\Theta}}{\operatorname{argmax}} \, l(\mathbf{\Theta}) \tag{5.8}$$

is solved by evaluating the zeros of the gradient

$$\frac{\partial}{\partial\mu} \ln p\left(\mathbf{X}|\mu, \sigma\right) = \sum_{n=1}^{N} \frac{1}{\sigma^2}\left(x_n - \mu\right) = 0, \tag{5.9a}$$

$$\frac{\partial}{\partial\sigma} \ln p\left(\mathbf{X}|\mu, \sigma\right) = \sum_{n=1}^{N} \left\{ -\frac{1}{\sigma} + \frac{\left(x_n - \mu\right)^2}{\sigma^3} \right\} = 0. \tag{5.9b}$$

Solving Eqs. (5.9a) and (5.9b) for μ and σ, respectively, yields the optimal set of parameters

$$\mu = \frac{1}{N} \sum_{n=1}^{N} x_n, \tag{5.10a}$$

$$\sigma^2 = \frac{1}{N} \sum_{n=1}^{N} (x_n - \mu)^2. \tag{5.10b}$$

Similar to the problem discussed in Section 4.3, this approach is tailored for scattered data, where each datapoint is located at a coordinate x_n. In the case of estimating the distribution of intensities on the imaging sensor, these coordinates have to be weighted with the measured intensity values $I(\xi_n)$, as described in Section 4.3. Substituting the weighted pixel coordinates $I(\xi_n)\xi_n$ for the datapoints x_n yields the optimal parameters

$$\mu = \frac{1}{I_{\text{tot}}} \sum_{n=1}^{N} I(\xi_n)\,\xi_n, \tag{5.11a}$$

$$\sigma = \frac{1}{I_{\text{tot}}} \sum_{n=1}^{N} I(\xi_n)\,(\xi_n - \mu)^2, \tag{5.11b}$$

with the total intensity on the imaging sensor

$$I_{\text{tot}} = \sum_{n=1}^{N} I(\xi_n). \tag{5.12}$$

Since MLE estimates distribution parameters of scattered data, it is unnecessary to work with the binned equidistant pixel coordinates. The algorithm performs even better when using the full transformed image data (see Fig. 4.9b), since more data points are available for the parameter estimation.

Fig. 5.5 shows the result of a Gaussian MLE fit of a spot obtained on a flat surface. The estimated parameters are given in Table 5.1. As one can see, the Gaussian model fits the obtained image data very well. Note that for the image data and the modeled distribution, two different ordinates are used since the model is normalized to have a cumulative density of

$$\int_{-\infty}^{\infty} \mathcal{N}(x|\mu,\sigma)\mathrm{d}x = 1. \tag{5.13}$$

In contrast to the NLSQ approach, no a priori intensity distribution information is needed to estimate the parameters. As one can see in Eqs. (5.11a), (5.11b) and (5.12), only the pixel coordinates ξ_n and the corresponding measured intensity values $I(\xi_n)$ are needed. Therefore, as long as the intensity profile on the imaging sensor is normally distributed, this approach outperforms the NLSQ approach due to its robustness.
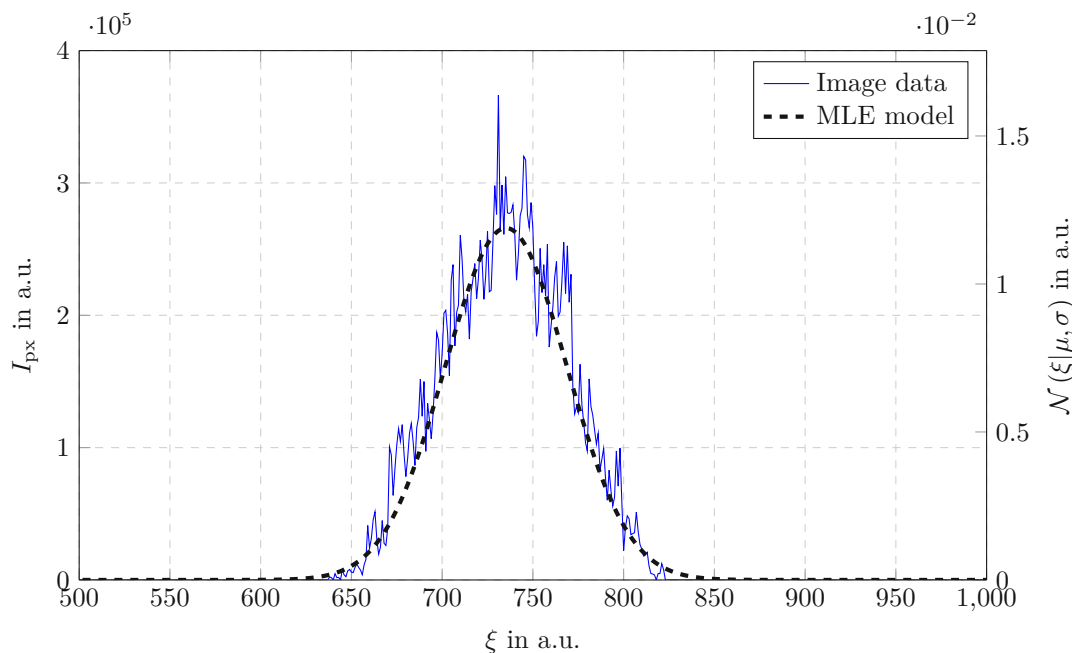
Figure 5.5: Results of the parameter estimation using MLE. As the image data is normally distributed, the estimated normal distribution fits the image data very well. Note that the estimated model is normalized and not to scale with the image data. Hence, a second ordinate is introduced.

Table 5.1: Estimated parameters of the MLE approach.

Parameter	Value
μ	735.193
σ	33.534

5.2.1.2 Gaussian mixture model (GMM) on edges

While the MLE algorithm for single Gaussian normal distributions performs well on flat surfaces, it quickly approaches its limit when the measurement is conducted on the

edge of the sample. Since the intensity distribution on the imaging sensor is no longer normally distributed as shown in Fig. 5.2b, a single normal distribution is no longer suitable to model the intensity distribution. Looking at Fig. 5.2b, the transformed image appears to consist of two Gaussian distributions combined with different weights. Thus, the model given in Eq. (5.1) is extended to a Gaussian mixture model (GMM) [79], a superposition of weighted normal distributions

$$\text{GMM}(\mathbf{X}|\mathbf{\Theta}) = p\left(\mathbf{X}|\mathbf{\Theta}\right) = \sum_{k=1}^{K} \pi_k \mathcal{N}\left(\mathbf{X}|\mathbf{\Theta}_k\right). \tag{5.14}$$

with the parameters

$$\mathbf{\Theta} = \begin{bmatrix} \mathbf{\Theta}_1 \\ \vdots \\ \mathbf{\Theta_K} \end{bmatrix} = \begin{bmatrix} \mu_1 \\ \sigma_1 \\ \pi_1 \\ \vdots \\ \mu_K \\ \sigma_K \\ \pi_K \end{bmatrix}, \tag{5.15}$$

K Gaussian normal distributions, each parametrized by the respective mean value μ_k and standard deviation σ_k are weighted with a weight π_k and added up. The weighting factor π_k is called the prior of the respective Guassian component and is constrained to

$$\sum_{k=1}^{K} \pi_k = 1, \quad 0 \le \pi_k \le 1, \tag{5.16}$$

assuring that the cummulative probability of the GMM is normalized as

$$\begin{aligned} \int_{-\infty}^{\infty} p\left(x|\mathbf{\Theta}\right) dx &= \int_{-\infty}^{\infty} \sum_{k=1}^{K} \pi_k \mathcal{N}\left(x|\mathbf{\Theta}_k\right) dx \\ &= \pi_1 \underbrace{\int_{-\infty}^{\infty} \mathcal{N}\left(x|\mathbf{\Theta}_1\right) dx}_{=1} + \ldots + \pi_K \underbrace{\int_{-\infty}^{\infty} \mathcal{N}\left(x|\mathbf{\Theta}_K\right) dx}_{=1} \\ &= \sum_{k=1}^{K} \pi_k = 1. \end{aligned} \tag{5.17}$$

Equally as in the single Gaussian model, the parameters are obtained by solving the optimization problem stated in Eq. (5.8) with the loglikelihood function

$$l(\boldsymbol{\Theta}) = \ln p(\mathbf{X}|\boldsymbol{\pi}, \boldsymbol{\mu}, \boldsymbol{\sigma}) = \sum_{n=1}^{N} \left[\ln \left[\sum_{k=1}^{K} \pi_k \mathcal{N}\left(x_n|\mu_k, \sigma_k\right) \right] \right]. \tag{5.18}$$

Solving the optimization problem for a GMM is more complex than solving it for a single Gaussian distribution. Setting the derivatives to zero does not yield a closed-form solution for the parameters [77]. Therefore, a different approach, namely the expectation-maximization (EM) algorithm for GMM [80–83] is used to estimate the parameters iteratively. As the name suggests, the EM algorithm consists of two steps: the E-step (expectation) and the subsequent M-step (maximization). The calculations needed in the EM algorithm can be derived by maximizing the loglikelihood function for each parameter.

Setting the partial derivative of Eq. (5.18) with respect to μ_k to zero leads to

$$\frac{\partial}{\partial \mu_k} l(\boldsymbol{\Theta}) \rightarrow 0 = -\sum_{n=1}^{N} \underbrace{\frac{\pi_k \mathcal{N}\left(x_n|\mu_k, \sigma_k\right)}{\sum_{j=1}^{K} \pi_j \mathcal{N}\left(x_n|\mu_j, \sigma_j\right)}}_{\gamma_{n,k}} \sigma_k^2(x_n - \mu_k). \tag{5.19}$$

Dividing by σ_k^2 and rearanging yields the solution for μ_k

$$\mu_k = \frac{1}{N_k} \sum_{n=1}^{N} \gamma_{n,k} x_n. \tag{5.20}$$

The posterior probability, or responsibility

$$\gamma_{n,k} = p\left(w_k|x_n, \boldsymbol{\Theta}\right) = \frac{p(w_k)p(x_n|\boldsymbol{\Theta}_k)}{p(x_n|\boldsymbol{\Theta})} = \frac{\pi_k \mathcal{N}\left(x_n|\mu_k, \sigma_k\right)}{\sum_{j=1}^{K} \pi_j \mathcal{N}\left(x_n|\mu_j, \sigma_j\right)}, \tag{5.21}$$

describes the probability of a Gaussian component w_k, given a datapoint x_n and the current parameters $\boldsymbol{\Theta}$. Alternatively, in other words, it expresses the probability that a datapoint x_n, given the current parameters $\boldsymbol{\Theta}$, belongs to the Gaussian component w_k. Since it "expects" which Gaussian component w_k contains the datapoint x_n, based on the current parameters $\boldsymbol{\Theta}$, this calculation is called the expectation step, or E-step. The variable N_k can be interpreted as the number of points, which are

part of the respective Gaussian component as is calculated as

$$N_k = \sum_{n=1}^{N} \gamma_{n,k}. \tag{5.22}$$

Using the responsibility, the mean value of the respective component μ_k can be interpreted as a weighted mean value, with the responsibilities acting as the weights as shown in Eq. (5.20).

Similar to the calculation of the mean values, the standard deviations σ_k can be calculated by setting the partial derivative of the loglikelihood function with respect to σ_k to zero and subsequently solving the equation for σ_k. Using Eqs. (5.21) and (5.22), yields

$$\sigma_k^2 = \frac{1}{N_k} \sum_{n=1}^{N} \gamma_{n,k} \left(x_n - \mu_k \right)^2, \tag{5.23}$$

which is also a weighted form of the standard variance formula.

To derive the optimal parameter π_k, the constraint in Eq. (5.16) is considered through a Lagrange multiplier in the maximization function

$$\ln p(\mathbf{X}|\mathbf{\Theta}) + \lambda \left(\sum_{k=1}^{K} \pi_k - 1 \right). \tag{5.24}$$

Setting the partial derivative to zero yields

$$\frac{\partial}{\partial \pi_k} \left(\ln p(\mathbf{X}|\mathbf{\Theta}) + \lambda \left(\sum_{k=1}^{K} \pi_k - 1 \right) \right) \rightarrow 0 = \sum_{n=1}^{N} \frac{\mathcal{N}\left(x_n|\mu_k, \sigma_k\right)}{\sum_{j=1}^{K} \pi_j \mathcal{N}\left(x_n|\mu_j, \sigma_j\right)} + \lambda. \tag{5.25}$$

By multplying both sides with π_k and summing up over all k, the Lagrange multiplier can be determined as $\lambda = -N$ and subsequently the priors result as

$$\pi_k = \frac{N_k}{N}. \tag{5.26}$$

Since π_k are the prior probabilities of the respective Gaussian components, they can intuitively be interpreted as the proportion of the total number of points N belonging to the respective component.

Despite solutions that can be derived as shown above, the equations presented in Eqs. (5.20), (5.23) and (5.26) are not a closed-form solution since they all depend on the responsibilities given in Eq. (5.21). The responsibilities, however, depend on the

parameters that should be estimated. Therefore, the maximization problem has to be solved iteratively in the following steps.

1. **Initialization**

   A good choice of initial parameter values significantly improves the convergence speed of the EM algorithm and prevents it from converging to a suboptimal local loglikelihood maximum. Since the GMM is used on measurements on edges, two Gaussian components ($K = 2$), one for each surface on either side of the edge, are sufficient. Initially, the priors π_k are chosen to be equal, so both components are weighted equally. The standard deviations σ_k are also chosen equally and set to the standard deviation of the whole intensity distribution according to Eq. (5.11b). To choose initial mean values mu_k, some a priori knowledge of the intensity profile can be used. Since the highest intensity in the image data is expected to coincide with the mean value of one Gaussian component, the first initial mean μ_1 is chosen to be the pixel coordinate ξ at which the highest intensity value $I(\xi)$ occurs. The second mean value μ_2 is set to the pixel coordinate with the largest weighted squared distance to μ_1. Therefore, the initial parameters for the EM algorithm result as

$$\mu_1^{(0)} = \operatorname*{argmax}_{\xi} I(\xi) \tag{5.27a}$$

$$\mu_2^{(0)} = \operatorname*{argmax}_{\xi} \frac{I(\xi)(\xi - \mu_1)^2}{I_{\text{tot}}} \tag{5.27b}$$

$$\sigma_1^{(0)} = \sigma_2^{(0)} = \frac{1}{I_{\text{tot}}} \sum_{n=1}^{N} I(\xi_n)(\xi_n - \mu)^2 \tag{5.27c}$$

$$\pi_1^{(0)} = \pi_2^{(0)} = \frac{1}{K} = \frac{1}{2} \tag{5.27d}$$

   with μ being the total mean value of the image data according to Eq. (5.11a) and I_{tot} being the sum of intensity values given in Eq. (5.12). The superscripted zero marks the parameters as initial values. From now on, currently available old parameters are marked with a "-", and updated parameters are indicated with "+".

2. **E-step**

   In the expectation step, the responsibilities, meaning the probabilities of points x_n belonging to a Gaussian component w_k given the current parameters, are calculated. Similarly to the MLE in the one-dimensional case, scattered data

is imitated using the intensity $I(\xi)$ as the frequency of a pixel coordinate ξ.

$$\gamma_{n,k} = \frac{\pi_k^- \mathcal{N}\left(\xi_n | \mu_k^-, \sigma_k^-\right)}{\sum_{j=1}^2 \pi_j^- \mathcal{N}\left(\xi_n | \mu_j^-, \sigma_j^-\right)} \tag{5.28a}$$

$$N_k = \sum_{n=1}^N I\left(\xi_n\right) \gamma_{n,k} \tag{5.28b}$$

3. **M-step**

   In the maximization step, the loglikelihood function is increased by calculating the optimal parameter values derived previously, using the responsibilities obtained in the E-step and the current parameters as

$$\mu_k^+ = \frac{1}{N_k} \sum_{n=1}^N \gamma_{n,k} I(\xi_n) \xi_n, \tag{5.29a}$$

$$\sigma_k^+ = \frac{1}{N_k} \sum_{n=1}^N \gamma_{n,k} I(\xi_n) \left(\xi_n - \mu_k^+\right)^2, \tag{5.29b}$$

$$\pi_k^+ = \frac{N_k}{I_{\text{tot}}}. \tag{5.29c}$$

4. **Evaluation**

   Using the updated parameter values, the loglikelihood function

$$l(\mathbf{\Theta}^+) = \sum_{n=1}^N \left[\ln \left[\sum_{k=1}^2 \pi_k^+ I(\xi_n) \mathcal{N}\left(\xi_n | \mu_k^+, \sigma_k^+\right) \right] \right]. \tag{5.30}$$

   is evaluated. If the condition

$$l(\mathbf{\Theta}^+) - l(\mathbf{\Theta}^-) < \Delta l, \tag{5.31}$$

   with a threshold Δl is fulfilled, the loglikelihood function does not change significantly with updated parameters, and thus, the EM algorithm has converged and is terminated. The next iteration starts at step 2 if the condition is not fulfilled.

As the EM algorithm uses a probabilistic approach to determine the model parameters, the pixel coordinates do not have to be equidistantly spaced. Therefore, to improve the fit performance, the whole transformed 1D image data, not the binned image data, is used to estimate the parameters. The computation time can be significantly reduced by thresholding the intensity values and omitting all values below the threshold. In

Fig. 5.6, the result of a GMM fit is shown, with the estimated parameters given in Table 5.2. Each Gaussian component represents one reflected spot from either side of the edge. The combination of the two components fits the obtained intensity profile.

Table 5.2: Estimated parameters of the GMM shown in Fig. 5.6.

Gaussian component	π_k	μ_k	σ_k
component 1	0.656	594.824	37.698
component 2	0.344	732.330	34.717

The intensity detected by the imaging sensor is reflected from the sample's surface. Therefore, when measuring on an edge, the higher the laser intensity on the sample's surface on one side of the edge, the higher the detected intensity peak on the imaging sensor corresponds to this sample height. Thus, the proportion of the laser power reflected from one sample height can be determined using the intensity profile obtained by the imaging sensor. Using a GMM, the power proportion reflected from one sample height can be obtained by integrating over one Gaussian component. The property in Eq. (5.17) comes in handy, as the integral simplifies to the prior π_k. Hence, the intensity proportions are determined as

$$\frac{P_{1,\text{sample}}}{P_{\text{tot,sample}}} = \pi_1, \tag{5.32a}$$

$$\frac{P_{2,\text{sample}}}{P_{\text{tot,sample}}} = \pi_2, \tag{5.32b}$$

with the total laser power on the sample $P_{\text{tot,sample}}$ and the power on the respective sample height $P_{1,\text{sample}}$ and $P_{2,\text{sample}}$.

5.2.2 Matched filter

Determining the proportional laser power on either side of the sample does not necessarily require a GMM of the image data. One could add up the measured intensities corresponding to the respective sample height. The local minimum between the two intensity peaks can be used as a threshold to distinguish between the sample heights before and after the edge. In the GMM, this local minimum is the transition point between the Gaussian components, as clearly visible in Fig. 5.6. However, the noise in the image data impedes the detection of the local minimum. Therefore, a filter has to be designed to denoise the signal.
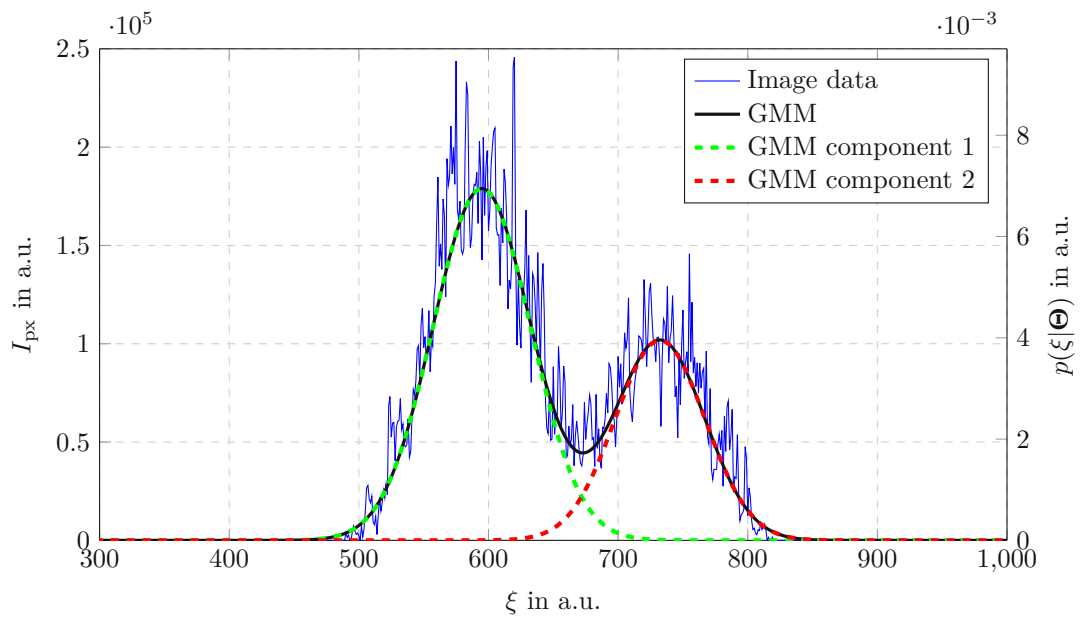
Figure 5.6: GMM fit of the measurement data. The GMM in black fits the complete shape of the intensity profile. Each Gaussian component represents one intensity peak caused by the varying sample heights on either side of the edge.

It would be sufficient for the filtered signal to detect the intensity peaks and the local minimum in between, as the power related to two different sample heights can be obtained by summing up the intensity values to the left and right of the minimum, respectively. Since, as discussed previously, the shape of an intensity peak on the imaging sensor can be expected to be Gaussian, a matched filter approach is suitable for this application [84, 85]. A Gaussian function $\mathcal{N}\left(\mathbf{X}_f|\mu_f,\sigma_f\right)$ with its parameters given in Table 5.3 is used as the filter kernel. Note that the kernel is zero-centered to avoid offsets in the resulting signal. A value of μ_f other than zero would result in an offset of μ_f in ξ-direction in the filtered intensity distribution. As shown above in Tables 5.1 and 5.2, an intensity peak on a flat surface typically has a standard deviation of approximately 35 for the chosen system configuration. To avoid overlaps with the second maximum, the filter kernel's standard deviation is three times smaller as $\sigma_f = 10$. Smaller values of σ_f would cause less noise reduction, while higher values would blur the two peaks. As 99.99 % of all points in a normal distribution are within $\pm 4\sigma$, the sampling points of the filter $\mathbf{X}_f$ are chosen to be in the interval $[-4\sigma \ldots 4\sigma]$. The filtered intensity profile is calculated by multiplying the Fourier transform of the image data with the conjugate complex Fourier transform of the

matched filter and subsequent inverse Fourier transforming as

$$I_f(\boldsymbol{\xi}) = \mathcal{F}^{-1}\left\{\mathcal{F}\left\{\mathbf{I}(\boldsymbol{\xi})\right\}\mathcal{F}^*\left\{\mathcal{N}\left(\mathbf{X}_f|\mu_f,\sigma_f\right)\right\}\right\}. \tag{5.33}$$

The resulting filtered intensity profile is depicted in Fig. 5.7. Using the matched filter approach, the noise data gets smoothed, and the denoised intensity profile is clearly visible in dashed black.

Table 5.3: Parameters of the matched filter kernel.

Parameter	Value
μ_f	0
σ_f	10
$\mathbf{X}_f$	$-4\sigma_f \ldots 4\sigma_f$
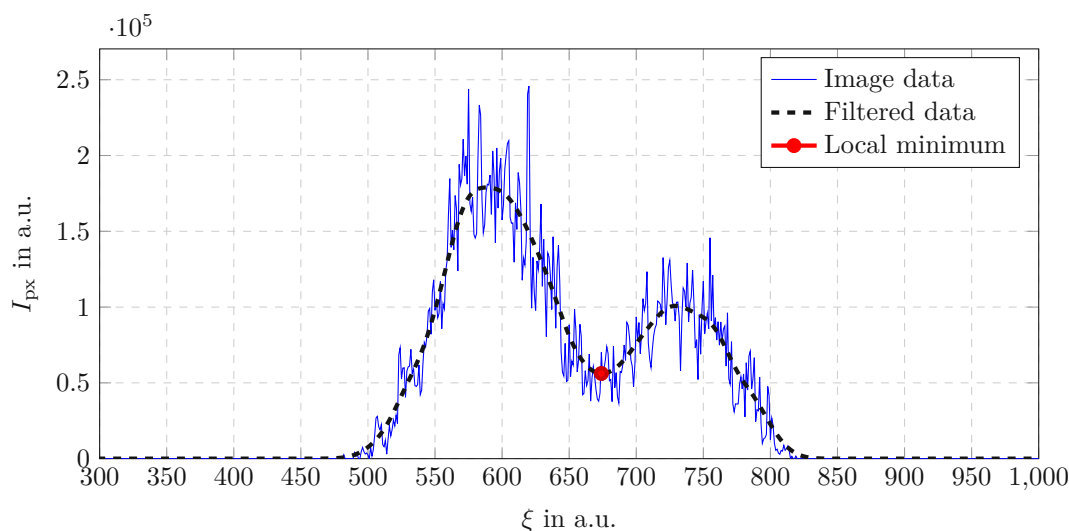
Figure 5.7: Filtered image using the matched filter. The raw data gets denoised and a smooth envelope curve, shown in black, is obtained. Using the denoised data, the local minimum between the peaks, shown in red, is identified.

Using the filtered data, the local minimum between the two intensity peaks can now be identified by searching for the local minimum with the highest prominence. The prominence of a local minimum is defined as the distance to the lowest adjacent local minimum value [86, 87]. To avoid the detection of ambiguous minima, an additional minimum prominence with an empirically determined value of 50 is used as a lower bound. The red dot in Fig. 5.7 indicates the detected minimum at the location $\xi_m = 674$.

The detection of the local minimum is sufficient to determine the proportional power of the peaks. Summing up the intensity values of the measured intensity profile to the left and the right of the minimum, respectively, yields the proportional laser power on the sample

$$\frac{P_{1,\text{sample}}}{P_{\text{tot,sample}}} = \frac{\sum_{n=1}^{m} I(\xi_n)}{\sum_{n=1}^{N} I(\xi_n)}, \tag{5.34a}$$

$$\frac{P_{2,\text{sample}}}{P_{\text{tot,sample}}} = \frac{\sum_{n=m+1}^{m} I(\xi_n)}{\sum_{n=1}^{N} I(\xi_n)}. \tag{5.34b}$$

5.3 Dynamic measurements

Due to the function principle of CMOS imaging sensors (see Section 2.2.2), a pixel value is proportional to the integral value of the received light flux during the exposure time

$$I(\xi) \propto \int_0^{T_{\text{exp}}} \Phi_e(t) dt, \tag{5.35}$$

with the radiant flux Φ_e. Therefore, if the sample height changes during the exposure time, a larger area of the imaging sensor gets exposed, yielding a non-Gaussian intensity distribution on the sensor due to motion blur. However, the sample height does not change when measuring on a flat, moving surface. Hence, the spot location on the imaging sensor stays constant during the exposure. Solely, the speckle pattern gets blurred by the motion, yielding an overall speckle noise reduction [30]. Therefore, when an edge feature moves past the LTS, both illuminated sample heights, before and after the edge, result in a spot on the imaging sensor. Since the change in height occurs instantaneously, two spots are detected. The obtained intensity distribution cannot be distinguished from a static measurement on an edge. Thus, all methods mentioned above to analyze the intensity distribution can also be used for dynamic measurements on moving samples.

As both the GMM model and the matched filter approach can determine the proportional laser power on each sample surface, this information can determine the lateral edge position within the distance the sample moves during the exposure time. However, since the fiber collimator outputs a collimated beam with a Gaussian intensity profile, the laser power is not homogenously distributed on the sample. Thus, a model of the intensity distribution on the moving sample is required.

5.3.1 Modelling the laser intensity distribution on the sample

According to the fiber collimator's datasheet, the emitted beam has a Gaussian intensity profile with a waist diameter of $d = 0.8\,\mathrm{mm}$. As the collimator is aligned perpendicular to the flat sample surface, the intensity profile at the static sample can be modeled as a symmetrical Gaussian normal distribution

$$I_{\mathrm{spot}}(x,y) = \frac{1}{2\pi\sigma^2}e^{\left(-\frac{1}{2}\frac{(x-x_0)^2+(y-y_0)^2}{\sigma^2}\right)}, \tag{5.36}$$

with the spot center (x_0, y_0). The waist diameter is the $1/e^2$ diameter, which means the diameter at which the power is reduced to a factor of $1/e^2$ from the maximum power. Using the symmetry of Eq. (5.36), y can be set to y_0, and thus, the standard deviation σ can be determined by solving

$$\frac{1}{2\pi\sigma^2}e^{-\frac{1}{2}\left(\frac{d}{2\sigma}\right)^2} = \frac{1}{2\pi\sigma^2}e^{-2} \tag{5.37}$$

for σ. This results in a standard deviation of

$$\sigma = \frac{d}{4}. \tag{5.38}$$

However, the effective spot size that the imaging sensor detects is expected to be smaller than the spot size on the sample since the intensity of light reflected from a point further away from the spot's center is too low to be detected. Thus, the effective spot size on the sample that contributes to the spot on the imaging sensor must be determined. In the first step, the model of the spot in Eq. (5.36) can be simplified to a one-dimensional Gaussian distribution function. Since the edges of the sample are expected to occur perpendicular to the movement direction x as illustrated in Fig. 5.1, the intensity that is reflected from a line in y direction at a constant position x corresponds to the same height measurement on the imaging sensor. Thus, by integrating the intensity over y, the one-dimensional length-related power is obtained as

$$I_{\mathrm{spot}}(x) = \int_{-\infty}^{\infty}\frac{1}{2\pi\sigma^2}e^{\left(-\frac{1}{2}\frac{(x-x_0)^2+(y-y_0)^2}{\sigma^2}\right)}dy = \frac{1}{\sigma\sqrt{2\pi}}e^{-\frac{(x-x_0)^2}{2\sigma^2}}. \tag{5.39}$$

Static measurements on an edge are conducted to estimate the effective spot size. The respective proportional power that is reflected from the surface before (d_1) and after edge (d_2), is determined using the previously introduced GMM. The prior π_2 equals the light's proportional power, reflected from the surface d_2 after the edge

as shown in Eq. (5.32). As the edge moves past the laser spot, more power gets reflected from d_2, and the power at P_2 increases. Thus, by taking images for various lateral displacements x and deterimining the parameters of the GMM, the cumulative distribution function (CDF) of the laser power on d_2

$$P_{\text{spot}}(x) = \int_{-\infty}^{x} I_{\text{spot}}(\tau)d\tau = \int_{-\infty}^{x} \frac{1}{\sigma\sqrt{2\pi}} e^{-\frac{(\tau-x_0)^2}{2\sigma^2}} d\tau = \frac{1}{2} + \frac{\text{erf}\left(\frac{\sqrt{2}(x-x_0)}{2\sigma}\right)}{2}, \quad (5.40)$$

can be determined. The obtained CDF is displayed in Fig. 5.8. While the blue line shows the obtained values of the prior π_2, and thus the proportional power reflected from d_2, the black line shows the fitted model given in Eq. (5.40). The parameters x_0 and σ are estimated using NLSQ parameter estimation. While the mean value x_0 is only used as an offset in x-direction, the estimated standard deviation of $\sigma_{\text{eff}} = 0.0834\,\text{mm}$ yields the intensity distribution shown in blue in Fig. 5.9 with an effective spot diameter of $d_{\text{eff}} = 0.3336\,\text{mm}$. Surface defects on the 3D-printed sample cause the outliers of the measured power.
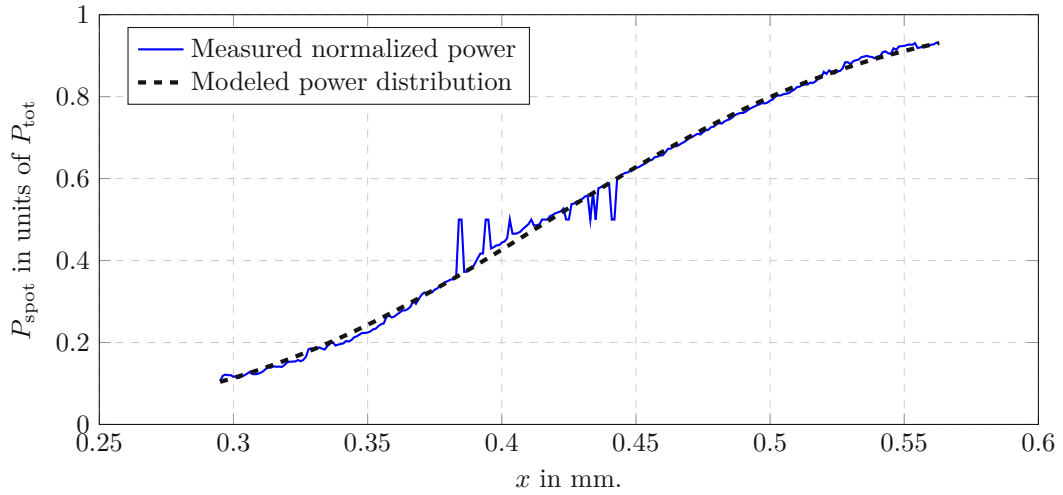
Figure 5.8: Identification of the effective spot size. The modeled normalized power distribution fits the measured distribution. Surface defects on the sample cause the outliers in the measured power distribution.

As the sample is moving at the velocity v in x-direction, the center of the laser spot on the sample travels the distance

$$\Delta x = \underbrace{vT_{\text{exp}}}_{\Delta x_{\text{exp}}} + \underbrace{v\left(T_{\text{ADC}} + T_{\text{cam}}\right)}_{\Delta x_{\text{blind}}}, \quad (5.41)$$

during one frame, as discussed in Section 3.1. Since the obtained image results solely from the sample surface illuminated by the laser during the exposure time T_{exp}, only the travel distance Δx_{exp} is relevant for the model. The intensity distribution on the moving sample can be modeled as a convolution of the spot profile $I_{\text{spot}}(x)$ over the traveled distance Δx_{exp}, resulting in

$$
\begin{aligned}
I_{\text{sample}}(x) &= \frac{1}{\Delta x_{\text{exp}}} \int_{x_0}^{x_0+\Delta x_{\text{exp}}} \frac{1}{\sigma\sqrt{2\pi}} e^{-\frac{(x-x_0-\tau)^2}{2\sigma^2}} d\tau \\
&= \frac{\text{erf}\left(\frac{\sqrt{2}(x-2x_0)}{2\sigma}\right) + \text{erf}\left(\frac{\sqrt{2}(2x_0+\Delta x_{\text{exp}}-x)}{2\sigma}\right)}{2\Delta x_{\text{exp}}}.
\end{aligned}
\tag{5.42}
$$

The red dotted line in 5.9 illustrates the modeled intensity distribution for a travel distance of $\Delta x_{\text{exp}} = 0.5\,\text{mm}$, starting at $x = 0\,\text{mm}$. To obtain the power on the sample, the intensity distribution derived in Eq. (5.42) is integrated, resulting in

$$
\begin{aligned}
P_{\text{sample}}(x) &= \int_{-\infty}^{x} I_{\text{sample}}(\tau) d\tau \\
&= \frac{\sigma\left(e^{-\alpha^2} - e^{-\beta^2}\right)}{\sqrt{2\pi}\Delta x_{\text{exp}}} + \\
&\quad \frac{(x-2x_0)\text{erf}(\alpha) + (x-2x_0-\Delta x_{\text{exp}})\text{erf}(\beta) + \Delta x_{\text{exp}}}{2\Delta x_{\text{exp}}},
\end{aligned}
\tag{5.43}
$$

where

$$
\alpha = \frac{(x-2x_0)}{\sqrt{2}\sigma},
\tag{5.44a}
$$

$$
\beta = \frac{(-x+2x_0+\Delta x_{\text{exp}})}{\sqrt{2}\sigma}.
\tag{5.44b}
$$

The resulting power $P_{\text{sample}}(x)$ is the resulting power of the intensity distribution $I_{\text{sample}}(x)$ until the point x, shown in dotted black in Fig. 5.9. If an edge is located at a location $x_1 = 0.3\,\text{mm}$, the surface area at a distance d_1 located before the edge is exposed to the power $P_1 = P_{\text{sample}}(x_1) = 0.602$, as illustrated in Fig. 5.9. The area after the edge, at a distance d_2, is exposed to the power $P_2 = 1 - P_1 = 0.398$.

Knowing the modeled intensity- and power distribution on the sample, as well as the measured proportional power of the peaks on the imaging sensor, the lateral position of an edge within the interval $[x_0, x_0 + \Delta x_{\text{exp}}]$ can now be determined, with the correction procedure being described in detail in Chapter 6.
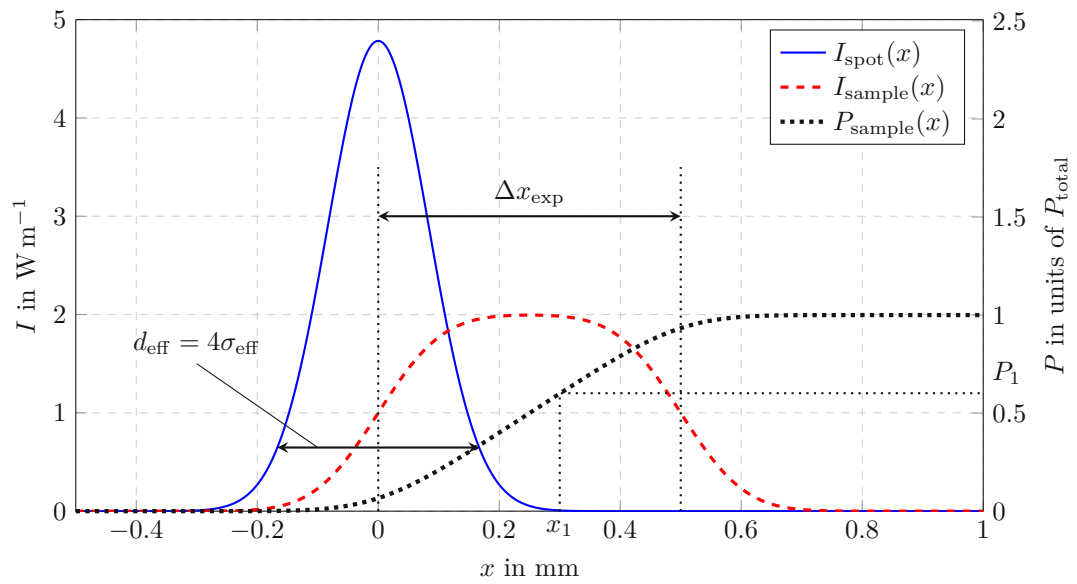
Figure 5.9: Model of the intensity distribution on the sample. On a static sample, the intensity has a Gaussian distribution shown in blue, while on the moving sample, it is spread along the traveled distance as shown in red dashed. Integrating the red intensity distribution results in the power on the sample shown as the black dotted line.

Lateral feature correction

The previously derived methods for DR (see Section 4.3) and to analyze the intensity distribution on the imaging sensor (see Chapter 5), are now used to estimate the true edge location on a moving sample. Correcting the lateral feature location is performed in a postprocessing step and consists of the following sequentially performed steps:

1. **Raw data preprocessing**
   The raw 2D images are converted to 1D intensity profiles using PCA based DR. These intensity profiles are analyzed, and features, such as the distance to the sample and proportional peak power, are extracted using a combination of filtering, 1D MLE and GMMs.

2. **Detection of edge frames and edge types**
   Frames obtained at the location of an edge are detected and classified into various edge types. The frame for the correction step is selected based on the respective edge type.

3. **Estimation of the true edge location**
   Using the features extracted in step 1, the edge location in the selected frame is estimated. The resulting data point at the estimated edge location is added to the existing measurement.

6.1 Raw data preprocessing

Before the correct edge locations can be estimated, the imaging sensor's raw data must be preprocessed. The sequential steps performed in the preprocessing are illustrated in Fig. 6.1. As one can see, in the first step, the 2D images are transformed into 1D intensity profiles using the DR method described in detail in Section 4.3.

Subsequently, key features, namely the distance to the target and the proportional power of the peaks, are extracted using the methods described in Section 5.2, of which the matched filter approach is the computationally cheapest. Furthermore, it provides the real measured power of the respective peak since the true measured intensity values are summed up. Therefore, it is used first to search for local minima in the intensity profile. In some cases, multiple local minima are detected due to excessive noise, contamination of the sample, or surface defects. If so, the minimum having the highest prominence is selected, and the intensity values to the left and the right of the minimum are summed up to obtain the proportional powers of each peak, $\pi_{1,2}$, respectively. As mentioned in Section 3.2, the highest intensity peak is used to determine the distance to the sample surface. The location of the intensity maximum ζ is determined to sub-pixel accurarcy by Gaussian interpolation [88, 89] as

$$\zeta = \frac{\ln(\xi_{\max} - 1) - \ln(\xi_{\max} + 1)}{2\left[\ln(\xi_{\max} + 1) - 2\ln(\xi_{\max}) + \ln(\xi_{\max} - 1)\right]}, \tag{6.1}$$

with the pixel coordinate of the maximum measured intensity $\xi_{\max}$ obtained as

$$\xi_{\max} = \underset{\xi}{\operatorname{argmax}}\, I_{\mathrm{f}}(\xi), \tag{6.2}$$

of the filtered intensity profile $I_f(\xi)$. Using the interpolated location of the maximum and the cubic spline model $\mathcal{M}$, derived in Section 4.4, yields the distance to the sample surface

$$d = \mathcal{M}\left(\zeta\right). \tag{6.3}$$

In some cases, if one peak is significantly higher than the other, no local minimum can be detected, even though the measurement is conducted on an edge feature. Therefore, if no minimum is found, a 1D MLE fit of a Gaussian normal distribution is performed in the next step. The 1D MLE is the only one of the three used algorithms to determine whether the measurement was conducted on an edge feature or a flat surface. Since it is assumed that the sample surface is aligned perpendicularly to the laser beam and the laser beam is collimated, a constant spot size on the imaging sensor for an arbitrary distance to the sample is expected. Thus, when the standard deviation σ of the 1D MLE Gauss fit exceeds a threshold of $\sigma_{\max} = 50$, it can be expected that the measurement was conducted on an edge feature. Otherwise, the
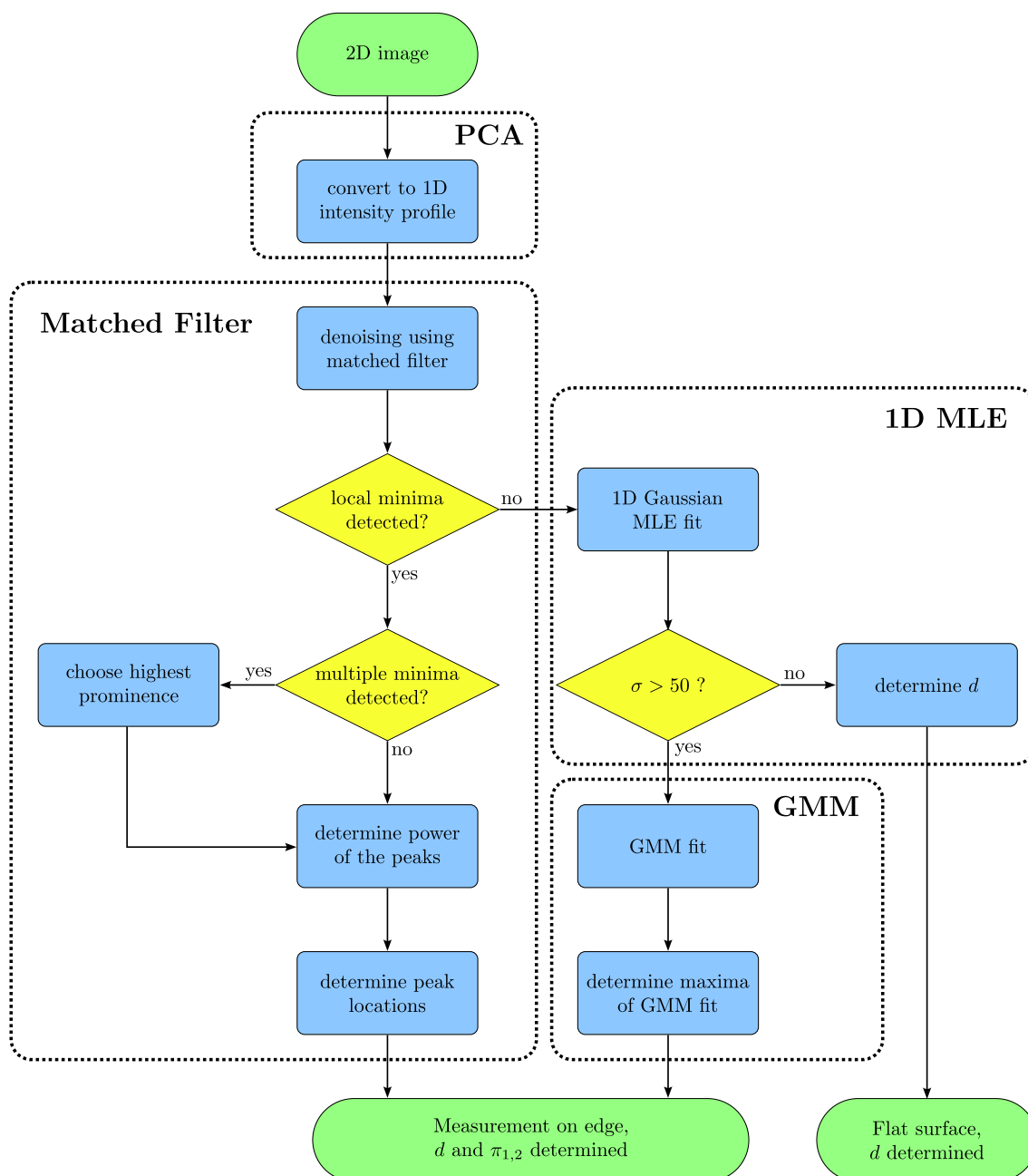
Figure 6.1: Flowchart of the preprocessing algorithm. The raw 2D image is converted to the 1D intensity profile using PCA. A combination of the methods introduced in Section 5.2 is used to obtain the measurement value and the proportional peak powers.

measurement was performed on a flat surface. In the latter case, the distance to the sample d is determined by

$$d = \mathcal{M}\left(\mu\right), \tag{6.4}$$

with the mean μ of the MLE fit.

If σ exceeds the threshold, two intensity peaks are expected. Using a GMM fit, the proportional power of the peaks $\pi_{1,2}$ are immediately received as estimated parameters. However, the location of the GMM's peaks does not necessarily coincide with the estimated means $\mu_{1,2}$. Therefore, the location of the maxima is determined by solving the optimization problem

$$\zeta_{1,2} = \underset{\zeta}{\mathrm{argmin}}\left\{-\mathrm{GMM}\left(\zeta|\mathbf{\Theta}\right)\right\}, \quad \zeta_0 = \mu_{1,2}, \tag{6.5}$$

with the GMM given in Eq. (5.14), where the two maxima $\zeta_{1,2}$ are determined by running the optimization two times with the starting values $\zeta_0 = \mu_{1,2}$, respectively. The distance ultimately results as

$$d = \mathcal{M}\left(\underset{\zeta_{1,2}}{\mathrm{argmax}}\left\{\mathrm{GMM}\left(\zeta_{1,2}|\Theta\right)\right\}\right), \tag{6.6}$$

where the location of the highest peak is used in the model $\mathcal{M}$.

The order of the analysis algorithms is chosen to maximize the parameter estimation accuracy in minimum runtime. Since the matched filtering is the computationally cheapest and provides the most accurate proportional power estimation, it is run first. If it fails, meaning that no local minimum is found, the 1D MLE algorithm is executed since it is computationally cheaper than the GMM fit, and it can determine whether the measurement was conducted on a flat surface or not. The GMM fitting is only performed if the filtering approach fails and the 1D MLE estimation leads to the expectation that the measurement was performed on an edge feature.

The result of the preprocessing is a dataset of distance measurements d and, if an edge feature occurred, estimations of the proportional peak powers $\pi_{1,2}$. From now on, the frames where an edge was detected are referred to as "feature frames".

6.2 Edge location estimation

The estimation of the true edge location is performed equally, regardless of the specific edge type. Therefore, it is discussed before the edge frame detection and edge type determination are described in detail.

Table 6.1: Comparison of preprocessing methods. The matched filter approach is the computationally cheapest and applicable for both single and double peaks.

Algorithm	Application	Computational effort
1D MLE	single peak	cheap
Matched filter	single & double peak	cheapest
GMM	double peak	expensive

Looking at the schematic illustration of a dynamic measurement illustrated in Fig. 6.2a, during one exposure time T_exp the sample moves the distance $\Delta x_\text{exp} = vT_\text{exp}$ in x-direction. To estimate the true edge location, it is more convenient to analyze the measurement in the sample-fixed reference frame $[x_\text{s}, y_\text{s}, z_\text{s}]^\text{T}$. Using this measurement frame, the sample moving in x-direction is equivalent to the laser spot on the sample moving in x_s direction. The moving laser spot causes the intensity distribution on the sample $I(x_\text{s})$. Given the edge location, the power reflected from the surface before and after the edge is indicated as the green and orange areas, respectively. Since the exposed surface area before the edge is larger than the surface area after the edge, the power P_1 is larger than P_2. This yields a higher intensity peak corresponding to d_1 at the imaging sensor. Hence, the measurement result of this frame is d_1. As the lateral position of a measurement point is defined as the laser spot's center position at the end of the exposure, the lateral position of the distance measurement d_1 is located after the true edge, as illustrated in Fig. 6.2b. The dashed red line indicates the assumed sample topography in the uncorrected case. As discussed in Section 3.1, the edge is assumed to be exactly between two measurement points to minimize the possible error.

The measurement result of the datapoint at $x_\text{s} = 0.5\,\text{mm}$ of d_1 does not correspond to the true distance to the sample d_2 at this location due to motion blur. As the intensity distribution on the imaging sensor that lead to this measurement value shows a double peak, the actual edge has to be located between this datapoint and the previous one. Thus, the lateral offset Δx_offset has to be estimated to obtain the true lateral edge location.

Due to the symmetry of the intensity distribution of the sample, the power on the sample's surface after the edge P_2 is given as

$$P_2 = \int_{\Delta x_\text{exp} - \Delta x_\text{offset}}^{\infty} I(x)dx = \int_{-\infty}^{\Delta x_\text{offset}} I(x)dx = P_\text{sample}(\Delta x_\text{offset})\big|_{x_0=0}, \tag{6.7}$$

(a) Schematic illustration   (b) Measurement result
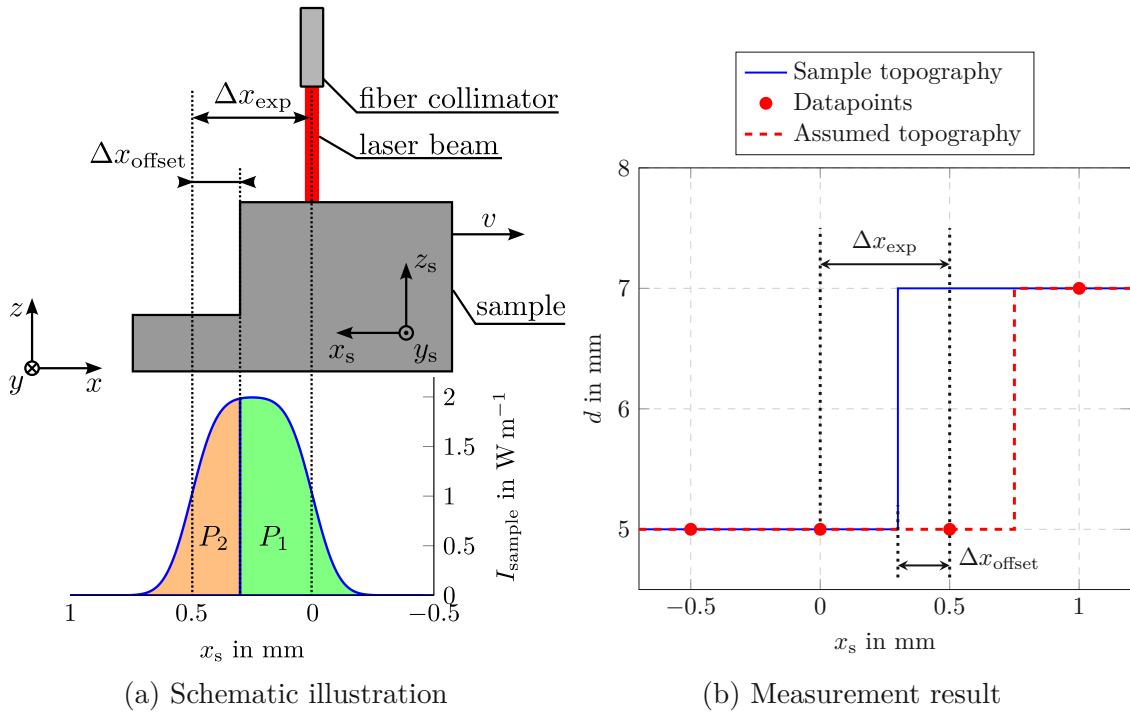
Figure 6.2: Schematic illustration of the laser power distribution von measuring on a
moving sample. While the sample in (a) moves in x-direction, the laser
moves in the sample fixed reference frame in x_s-direction. The power
on the sample P_1 being greater than P_2 leads to the measuring result
depicted in (b).

with P_sample derived in Eq. (5.43). To determine the offset using the given power
distribution, the equation

$$P_\mathrm{sample}(x)\big|_{x_0=0} - P_2 = 0, \tag{6.8}$$

is numerically solved for x, yielding the lateral edge offset $\Delta x_\mathrm{offset} = x$ as illustrated
in Fig. 6.3a.

Knowing the lateral offset, the true edge location can now be determined. Since
the lateral position of the datapoint in the considered frame is defined as the end
of the exposure, the true edge location is always before the datapoint's location.
Thus, the true edge location is determined by shifting the datapoint in negative
x_s-direction by the determined distance Δx_offset. This procedure is illustrated in
Fig. 6.3. The datapoint shown in gray in Fig. 6.3b is shifted in negative x_s-direction
by the obtained distance Δx_offset to the true edge location.

If $P_2 < 0.5$, which is equivalent to $P_2 < P_1$ since $P_1 + P_2 = 1$, the measured distance d is the distance to the sample's surface before the edge, due to the higher intensity peak at this location on the imaging sensor. The lateral position of a measurement point is defined as the laser spot's center at the end of the exposure. Thus, if $P_2 < 0.5$, the shifted datapoint represents the distance to the sample before the edge. To obtain a sharp edge in the measurement result, the datapoint of the next frame is copied to the same x_s position as the corrected point. This is shown in Fig. 6.3b, where the two red x's mark the shifted and the copied data point, respectively. Similarly, if $P_2 > 0.5$, the measured distance at the considered frame corresponds to the distance of the surface after the edge. Thus, after shifting the datapoint to the determined lateral edge position, the previous datapoint is copied and placed at the same position to obtain a sharp edge.

(a) Power distribution

(b) Corrected measurement
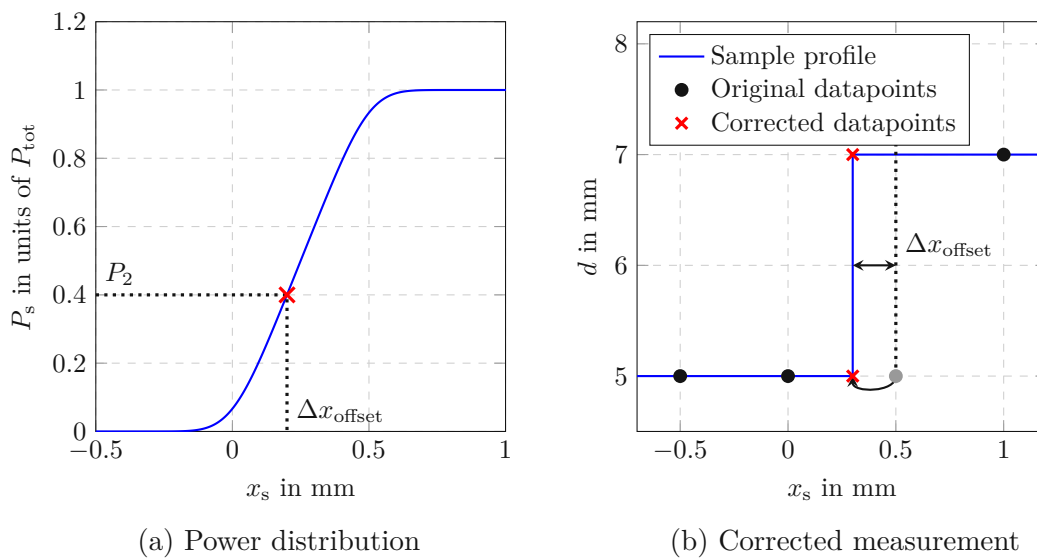
Figure 6.3: Edge location correction. Analyzing the power distribution in (a) corresponds to an offset Δx_{offset} for the power P_2. Correcting the measurement by this offset yields the corrected result in (b). The wrongly measured point, shown in grey, is shifted by the estimated offset. An additional point is inserted to obtain a sharp edge.

6.3 Detection of edge frames and edge types

The edge location correction procedure introduced above applies to any given feature frame. However, which frame should be considered for the correction is not trivial.

Before describing the frame selection process, the following definitions of terms are introduced for clarification.

Definition 1 (Edge frame). *A frame is an edge frame if the difference between the distance measurements of the considered frame d_i and the previous or next frame d_{i-1} and d_{i+1}, exceeds a minimum threshold of $\Delta d_{\min}$.*

$$|d_i - d_{i+1}| > \Delta d_{\min} \vee |d_i - d_{i-1}| > \Delta d_{\min} \tag{6.9}$$

Definition 2 (Feature frame). *If the intensity distribution on the imaging sensor shows a double-peak, this frame is denoted as a feature frame.*

Definition 3 (Single edge). *An edge is a single edge if at least two data points are located between the considered edge and the next edges before and after the considered edge.*

Definition 4 (Double edge). *A double edge combines a rising and falling edge, or vice versa, where only one data point is located between the edges.*

Note that, according to Definitions 1 and 2, an edge frame can also be a feature frame. Five different edge types can be distinguished, of which four are correctable. These cases, as well as the uncorrectable cases are discussed in the following.

6.3.1 Sinlge edge with mulitple feature frames

The first and most straightforward case is a single edge with multiple feature frames as illustrated in Fig. 6.4a. Multiple feature frames can occur if the travel distance during the exposure $\Delta x_{\exp}$ is on the scale of the spot size. In this case, the exposed sample areas of consecutive frames overlap. Hence, the edge is visible in multiple frames. The correction accuracy highly depends on the accuracy of the power distribution model. With the laser spot's standard deviation σ being the only empirically determined and error-prone model parameter, a power distribution with minimal sensitivity to σ is beneficial. The power distribution sensitivity depicted in Fig. 6.5 shows that the model is insensitive to σ in the middle of the travel distance. This is equivalent to P_2 having a value of $P_2 = 0.5$. Thus, the feature frame with a minimal power difference between the two peaks is chosen for the correction procedure.

6.3.2 Double edge with three feature frames

In the case of a double edge, where three feature frames are detected as illustrated in Fig. 6.4b, two of the three points must be chosen for the correction procedure. Only the two outer frames unambiguously contain information about the two edge

(a) Single edge, multiple feature frames

(b) Double edge, three feature frames

(c) Double edge, two feature frames

(d) Two feature frames without edge
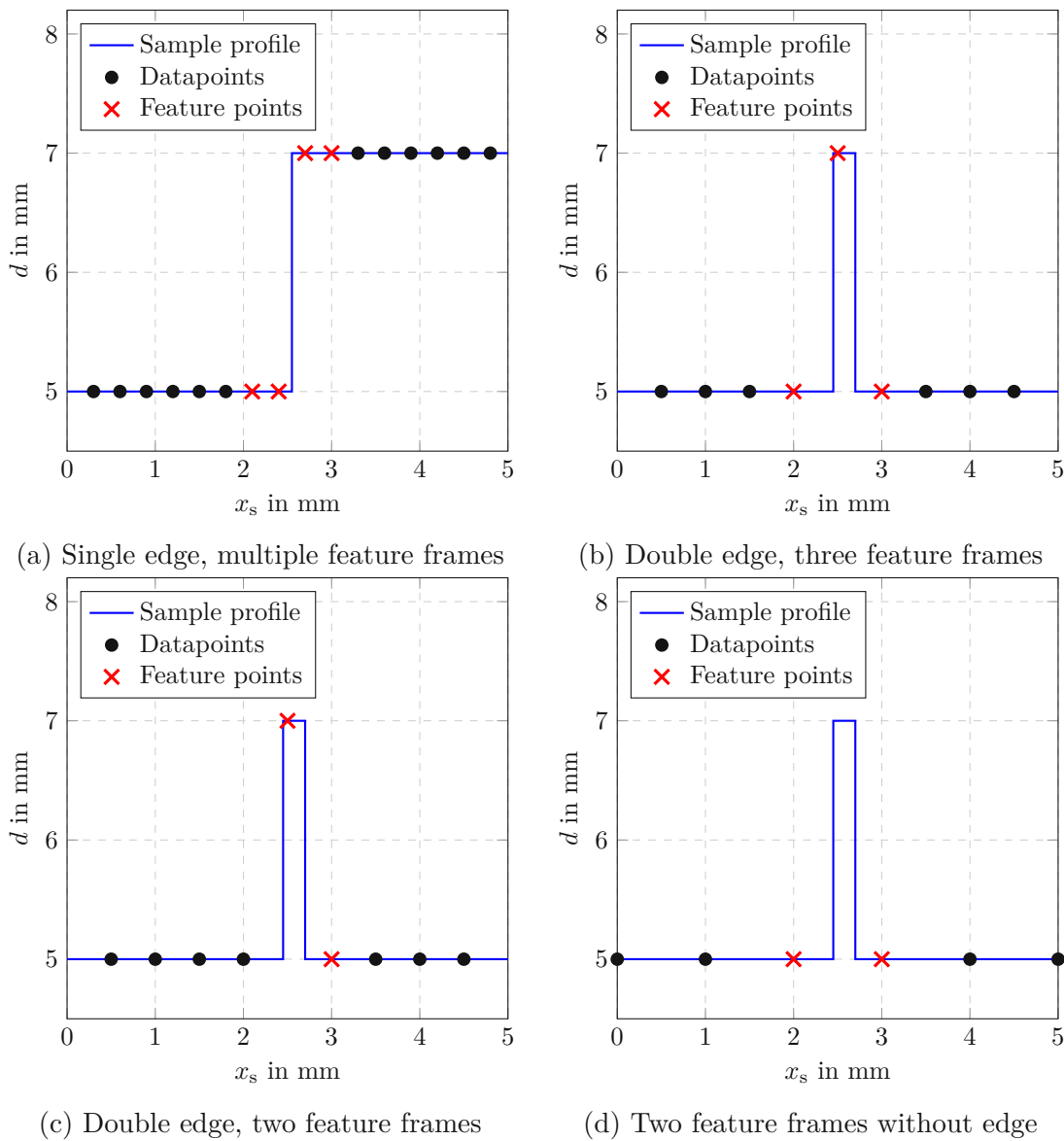
Figure 6.4: Overview of correctable edge types. In the case of a single edge with multiple feature frames in (a), the best feature frame is chosen to estimate the true edge position. As shown in (b), the middle frame is omitted on a double edge with three feature frames, as it can be ambiguous. When two feature frames are available at a double edge, as in Figure (c), each frame is used for one edge, respectively. If no edge is detected, but two feature points are available, as in (d), the sample profile still can be reconstructed.
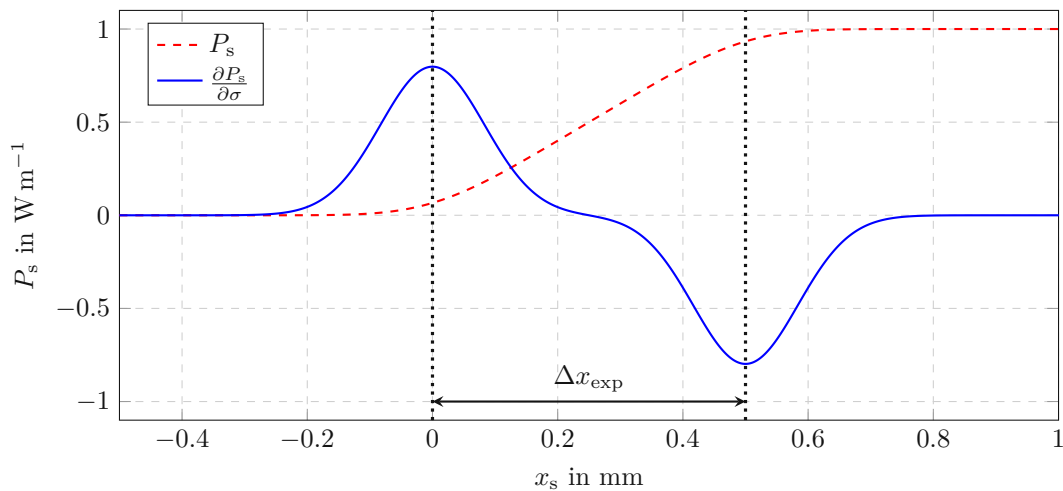
Figure 6.5: Sensitivity of the power distribution concerning the spot's standard deviation σ. In the middle of the exposed sample length, the sensitivity concerning σ and, thus, the sensitivity to model errors is the smallest.

locations. Since the distance to the sample before and after the double edge relates to the same spot on the imaging sensor, the intensity peaks of the middle frame cannot be unambiguously assigned to a specific lateral position. Thus, the middle feature frame is omitted, and the two outer feature frames are used to correct the lateral position of the two edges.

6.3.3 Double edge with two feature frames

When only two feature frames are available, both are edge frames, and both have to contain information about different edges. In the illustrated case in 6.4c, the datapoint before the edge is not a feature frame, hence containing no information about the edge. Therefore, the first feature frame has to contain information about the first edge. Similarly, the data point after the second feature frame is not a feature frame. Thus, the second feature frame must contain all the information about the second edge.

6.3.4 Two feature frames without an edge frame

The case where no edge frame is detected but two consecutive feature frames are available is solvable using a priori knowledge of the sample's profile. Suppose there is only one double edge between the two feature frames. In that case, the first feature frame contains the information about the first edge, and the second feature frame has

to contain information about the second edge. However, the measurement cannot be corrected if the structure within the two feature frames is more complex than a double edge. The edge height can be determined by using the location of the smaller peak in the model given in Eq. (6.3).

6.3.5 Single feature frame

No statement about any edge location can be made if only one feature frame is available. Even if an edge is detected in one frame, as exemplified in Fig. 6.6, the surfaces contributing to the double peak in the intensity profile cannot be distinguished. It can only be said that there is some feature. The size, however, is unknown.
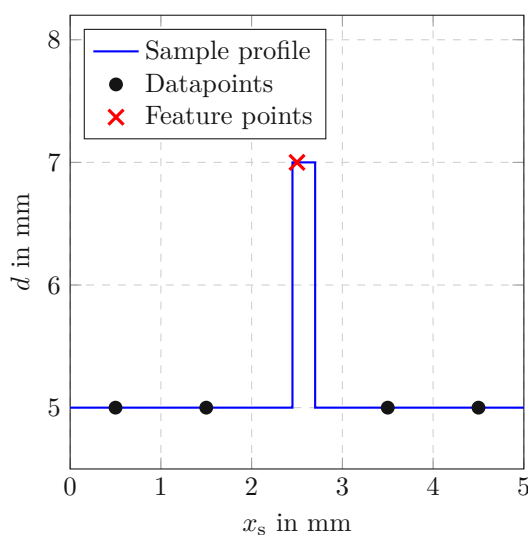
Figure 6.6: Uncorrectable edge. Since only one feature frame is available for the double edge, the two edges cannot be unambiguously reconstructed.

CHAPTER 7

Experimental performance evaluation

To verify the feature location correction procedure introduced in Chapter 6, measurements on a moving sample are conducted using the experimental setup described in Chapter 4. The lateral resolution and feature width uncertainty are compared to a standard, not corrected, measurement on a moving sample.

7.1 Test sample and evaluation procedure

For validation, the 3D printed test sample, shown in Fig. 7.1, is mounted on the linear stage. The sample contains four edge features of different lengths. The first feature is a valley of 2 mm height and a width of 4 mm. It is used to test the overall functionality of the correction procedure on large features. To evaluate the performance on small features, where the travel distance Δx_{exp} is larger than the feature itself, the second and third grooves with a depth of 2 mm and a width of 0.5 mm and 0.8 mm, respectively. The last feature is a step of 0.4 mm width at a height of 1 mm. Between each feature lies a flat surface with a width of 10 mm respectively, to distinguish between the individual features.

The actual feature topography is determined by performing static measurements on the sample using the custom LTS designed in Chapter 4. Using the linear stage, the sample is moved 1 µm between measurement points. The resulting reference sample profile is shown in Fig. 7.2. Note that the profile appears inverted compared to the modeled sample profile in Fig. 7.1b, as the distance to the sample d is measured and not the sample height directly. The feature widths differ slightly from the designed

(a) CAD model

(b) Nominal sample topography
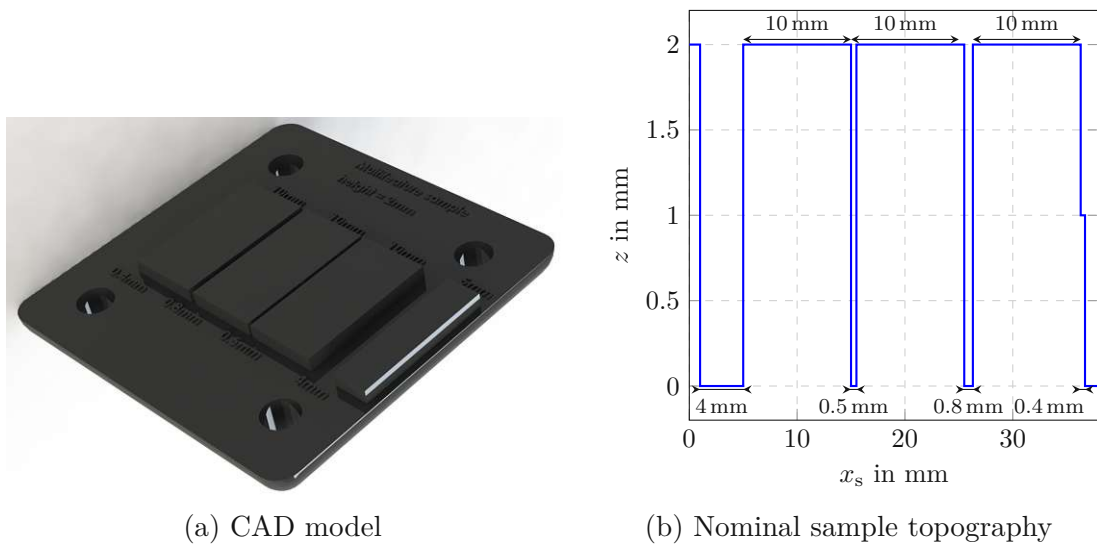
Figure 7.1: Test sample for the performance evaluation. The 3D-printed sample in (a) has a nominal feature height of 2 mm and a smaller feature width a height of 1 mm. The valleys alter in length, to determine the lateral resolution for various travel lenghts as depicted in (b).

widths due to manufacturing inaccuracies in the SLA printing and rework processes. Due to the relatively small size of the last feature compared to the laser spot size, it is not clearly visible as an edge but as a slope in the static reference measurement and, therefore, disregarded in the subsequent performance evaluation.

For the performance evaluation of the edge location correction procedure, measurements on the moving sample are conducted using various exposure times of the imaging sensor. The linear stage moves the sample at a constant speed of $v = 20 \, \text{mm s}^{-1}$. The travel distance during one exposure time $\Delta x_{\text{exp}} = v T_{\text{exp}}$ is adjusted by the chosen exposure time T_{exp}. A constant effective spot size on the sample for varying exposure times is achieved by adjusting the neutral density filter (see: Section 4.2).

Image data is transmitted via a USB 3.0 interface from the imaging sensor to the computer. Since this interface is not real-time capable, a constant frame time cannot be guaranteed. Looking at the image meta-data, the frame time fluctuates up to $\pm 50 \, \%$, also violating the set exposure time. Since the sensor's internal timings, which cause a blind spot, are unknown but expected to be small compared to the exposure time, they are neglected in the correction procedure, and the exposure time is assumed to be equal to the time difference between the two frames. This time, ΔT_{frame} is obtained from the transmitted meta-data. Thus, the travel distance used
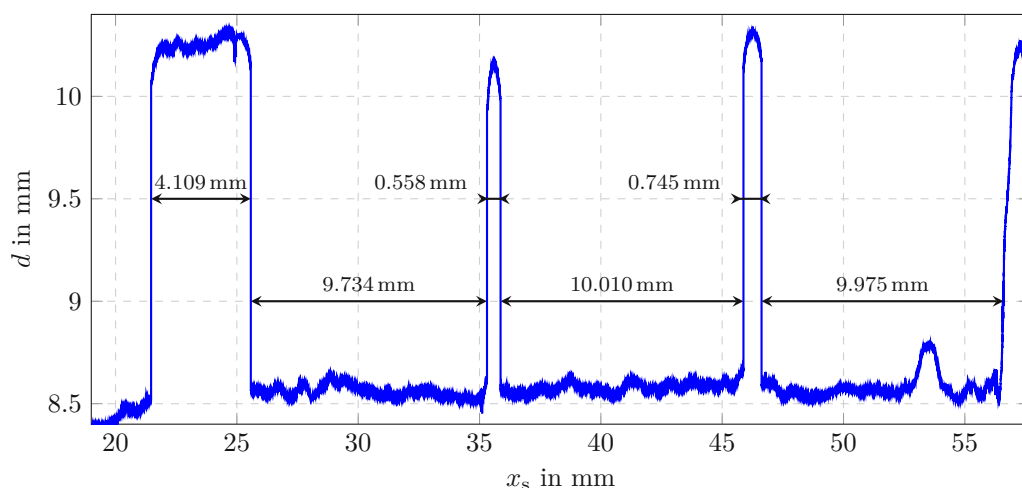
Figure 7.2: Static reference measurement of the sample. Due to manufacturing inaccuracies, the true feature widths differ from the CAD design. The last feature with a width of 0.4 mm and a height of 1 mm is not clearly visible due to its width being almost the effective size of the laser spot and its small height.

in the correction is obtained as

$$\Delta x_{\mathrm{sample}} = v \Delta T_{\mathrm{frame}} \approx v T_{\mathrm{exp}}. \tag{7.1}$$

7.2 Results

An example result is shown in Fig. 7.3. The illustrated section shows the second and third features of the test sample. With a frame time of $\Delta T_{\mathrm{frame}} = 40\,\mathrm{ms}$, the sample moves the distance $\Delta x_{\mathrm{sample}} = 0.8\,\mathrm{mm}$ during each frame. For a feature to be detected in a dynamic uncorrected measurement, at least half of the reflected light power has to be reflected from the feature surface to cause a higher intensity peak on the imaging sensor. Thus, the minimum feature width to be detectable is $\Delta x_{\mathrm{min}} = \Delta x_{\mathrm{exp}}/2$. In the illustrated case, the feature at $x_{\mathrm{s}} = 35\,\mathrm{mm}$ has a statically determined width of 0.558 mm. Although this feature width exceeds the necessary minimal width of $\Delta x_{\mathrm{min}} = 0.4\,\mathrm{mm}$, it is not detected in the uncorrcted dynamic measurement. That is probably caused by the fluctuating exposure time, which can lower the minimum feature width if the exposure time of the respective frame is shorter than the nominal value. However, utilizing the developed correction procedure, the feature is detectable, with its edge locations fitting the statically determined edge locations very well. While the feature at $x_{\mathrm{s}} = 46\,\mathrm{mm}$ is detected in
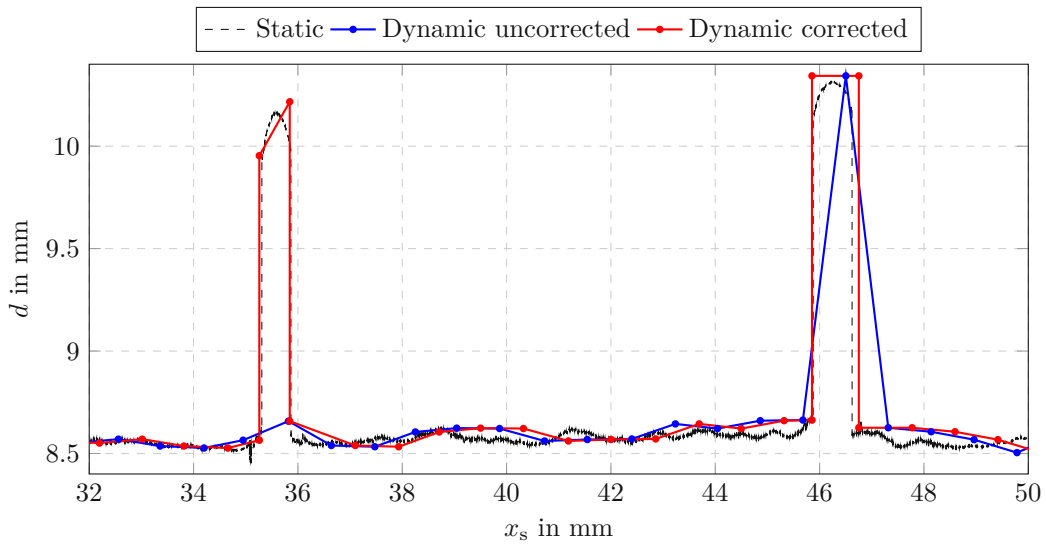
Figure 7.3: Correction result at a travel distance of $\Delta x_{\mathrm{exp}} = 0.8\,\mathrm{mm}$. The without correction invisible feature at $x_{\mathrm{s}} = 35\,\mathrm{mm}$ is clearly visible in the corrected measurement. Even if only one datapoint is on the feature, the edges can be reconstructed as visible at $x_{\mathrm{s}} = 46\,\mathrm{mm}$.

the uncorrected measurement, its edge location and width are greatly refined using the correction procedure.

To quantitatively evaluate the correction performance, dynamic measurements are performed for various exposure times, namely $10\,\mathrm{ms}$, $20\,\mathrm{ms}$, $30\,\mathrm{ms}$, $40\,\mathrm{ms}$ and $50\,\mathrm{ms}$, which correspond to travel distances $\Delta x_{\mathrm{frame}}$ of $0.2\,\mathrm{mm}$, $0.4\,\mathrm{mm}$, $0.6\,\mathrm{mm}$, $0.8\,\mathrm{mm}$ and $1\,\mathrm{mm}$ within one nominal frame. For each configuration, 50 measurements are conducted. The starting point x_0 varies randomly up to $1\,\mathrm{mm}$ for each measurement. After the raw image data of the measurements is obtained, the edge location correction procedure, described in detail in Chapter 6, is performed in a postprocessing step for each measurement. The measured feature widths shown in Fig. 7.2 serve as a performance measure. For a fair comparison, the edge location in the uncorrected dynamic measurements is assumed to be in the middle of the two edge frame locations, as it yields the smallest possible error as discussed in Chapter 3. As a performance measure, the error e of the dynamic feature widths, with respect to the statically measured feature widths, is considered. The accuracy in edge location detection is highly improved, as shown in Fig. 7.4. While the occurrence of errors in the uncorrected measurements, displayed in the left column, is widely spread, the corrected measurements in the right column are centered around an error of zero and limited to a significantly smaller range. Looking at the results given in Table 7.1, one can see that both the accuracy and the repeatability are significantly

improved by the correction procedure, as both the mean absolute error and the error's standard deviation are reduced. An outstanding performance increase is visible when investigating the detectability of features. While the uncorrected measurements miss 19 features at a travel distance of $\Delta x_{\text{frame}} = 0.8\,\text{mm}$, all features are detected in the corrected measurements. Even at a travel distance of $\Delta x_{\text{frame}} = 1\,\text{mm}$, where almost all of the small features with a width of $0.558\,\text{mm}$ are lost, the number of missed features can be reduced by more than a factor of two.

Table 7.1: Comparison of feature width errors for uncorrected and corrected dynamic measurements, respectively. The corrected measurements show a significant reduction in both absolute error and variance of error.

Δx_{sample} in mm	Uncorrected			Corrected		
	$\lvert\overline{e}\rvert$ in µm	σ_e in µm	missed	$\lvert\overline{e}\rvert$ in µm	σ_e in µm	missed
0.2	74.3	90.5	0	23.6	29.4	0
0.4	145.0	175.2	0	58.7	85.9	0
0.6	180.6	224.2	4	68.5	84.1	0
0.8	238.8	351.6	19	151.1	184.3	0
1.0	353.7	446.1	31	244.7	286.5	13

(a) $\Delta x_{\text{sample}} = 0.2\,\text{mm}$, uncorrected

(b) $\Delta x_{\text{sample}} = 0.2\,\text{mm}$, corrected

(c) $\Delta x_{\text{sample}} = 0.4\,\text{mm}$, uncorrected

(d) $\Delta x_{\text{sample}} = 0.4\,\text{mm}$, corrected

(e) $\Delta x_{\text{sample}} = 0.6\,\text{mm}$, uncorrected

(f) $\Delta x_{\text{sample}} = 0.6\,\text{mm}$, corrected

(g) $\Delta x_{\text{sample}} = 0.8\,\text{mm}$, uncorrected

(h) $\Delta x_{\text{sample}} = 0.8\,\text{mm}$, corrected

(i) $\Delta x_{\text{sample}} = 1\,\text{mm}$, uncorrected

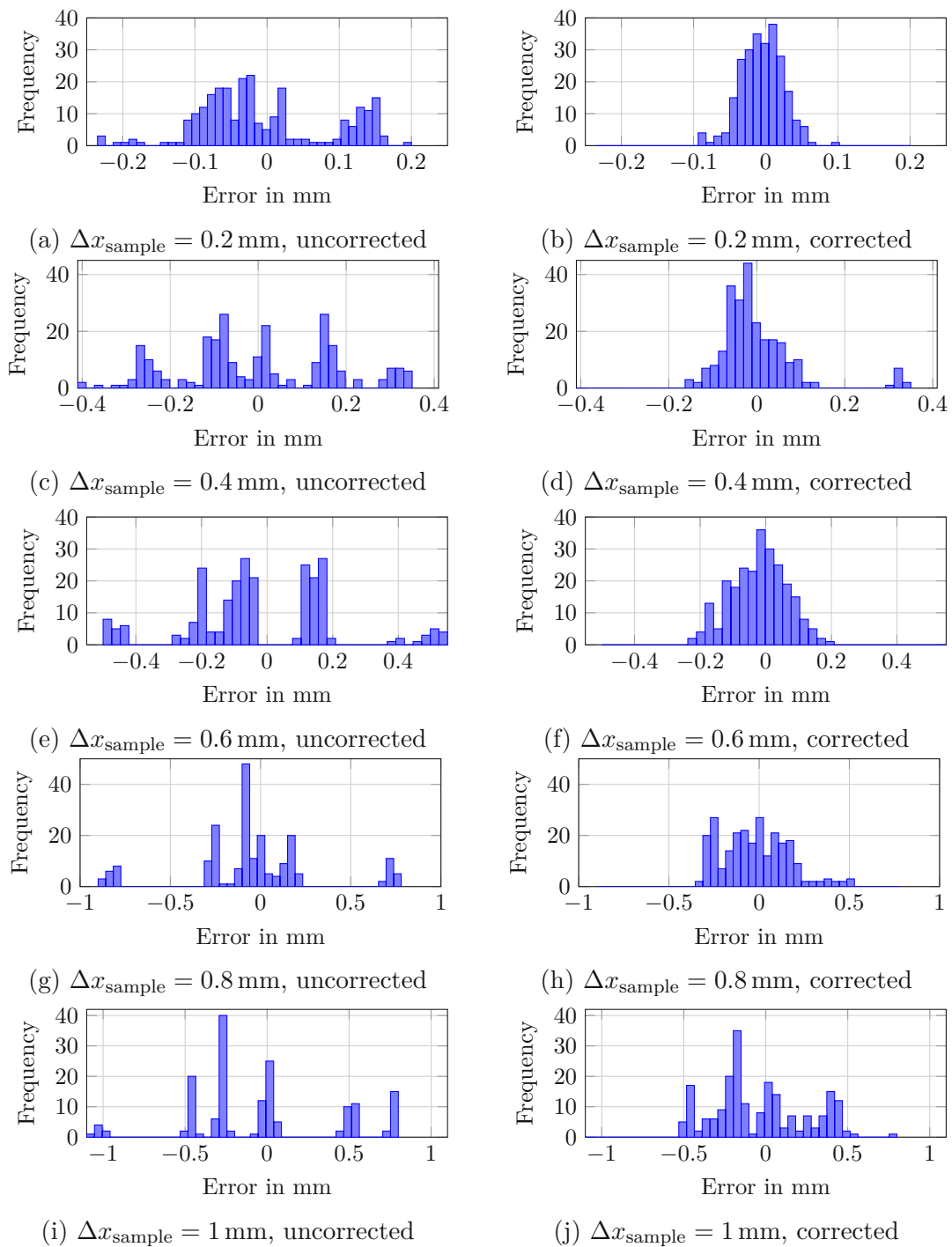(j) $\Delta x_{\text{sample}} = 1\,\text{mm}$, corrected

Figure 7.4: Histograms of feature width errors. While the errors of the dynamic uncorrected measurements in the left column are widely spread, the errors of the corrected dynamic measurement appear normally distributed around zero.

CHAPTER 8

Conclusion and Outlook

In the course of this thesis, a lateral feature location correction algorithm has been developed and successfully tested in laser triangulation measurements on moving samples. The findings are summarized in this chapter. Furthermore, an outlook towards future extensions and improvements regarding this work is given.

8.1 Conclusion

Regarding the findings of the literature research, this thesis aimed to reduce the lateral feature location uncertainty in laser triangulation measurements, as LTSs are the most frequently used sensors in in-line metrology applications. The initial analysis of the root causes of lateral uncertainty has shown that spatial sampling and motion blur result in lateral uncertainty that exceeds the travel distance of the moving sample Δx_{sample} during the sensor's exposure time. Since available industrial LTSs do not allow adjustment of sensor parameters like laser intensity or exposure time manually and are not able to output the imaging sensor's raw data, an experimental LTS has been designed. Considering the requirements derived in Section 4.1, the experiments LTS allows adjustment of laser intensity, exposure time, and, most importantly, the readout of the CMOS imaging sensor's raw pixel data. A thorough analysis of the intensity distribution on the imaging sensor when measuring on edge features has shown that the power ratio of the intensity peaks detected on the imaging sensor equals the power ratio of the laser on the sample surfaces prior to and after an edge.

After studying the state-of-the-art, two research questions arose and were formulated in Section 2.5. To conclude the findings of this thesis, these questions are answered in the following.

> **Research Question 1**
>
> Is it feasible to reduce the lateral position uncertainty of edge features in laser triangulation measurements on moving samples by algorithmically correcting the obtained measurement data?

The proposed feature location correction algorithm compares the peak power ratio on the imaging sensor to the model of the power ratio that is reflected from the sample surface. Using a combination of matched filtering, 1D Gaussian MLE, and GMM fitting, the power ratio obtained by the imaging sensor can be estimated. The power distribution model on the sample surface is derived by convolving the laser spot's intensity profile over the distance the sample travels during one exposure time Δx_{sample}. Using this model and the estimated power ratio, the lateral offset of an edge feature can be estimated. The experimental performance evaluation in Chapter 7 shows a significant reduction of the lateral feature location uncertainty. Using a 3D-printed test sample, the proposed method reduces the mean absolute feature width error by more than 60%. Thus, considering the presented results in Chapter 7, the first research question can be answered with yes.

> **Research Question 2**
>
> Is it feasible to reduce the effects of motion blur in laser triangulation measurements on moving samples by a tailored deblurring approach?

As shown in Chapter 7, small features can be missed in uncorrected measurements. The results in Table 7.1 show that features are missed in the uncorrected measurements if the feature width is smaller than the travel distance Δx_{sample}. Since the proposed correction algorithm does not only regard the displacement measurement value, but also the whole intensity distribution on the imaging sensor, information between two sampling points is considered as well. Only if the feature width is smaller than 70% of Δx_{sample}, features are missed in the corrected measurements, which is a significant improvement compared to the uncorrected case. Hence, the effect of missed features due to motion blur is significantly mitigated, which answers the second research question: Yes.

8.2 Outlook

Aiming for further improvement of the proposed lateral feature location correction algorithm, two limitations of the current approach must be pointed out. First, the CMOS imaging sensor transmits image data via a USB interface, which is not real-time capable. This leads to a fluctuation of the frame time and the exposure time. Evaluations have shown, that the deviation of the frame time from its nominal value reaches up to ±50%. Thus, an unknown error is induced in the intensity distribution model as it highly depends on the accuracy of the exposure time. A real-time imaging system with constant exposure and frame time can overcome this drawback. Furthermore, by knowing the exact exposure and frame time, the idle time, discussed in Section 3.1, which causes lateral blind spots in the measurement, can also be considered in the model.

As the spot diameter is a limiting factor for the axial, and thus, the lateral resolution of the correction algorithm, a focussed beam could be used instead of the collimated beam, reducing the spot size. However, a focused beam would result in a sample height-dependent spot size and intensity distribution on the sample, significantly increasing the model complexity.

The proposed method is currently limited to edge features of a sample. Since, in many applications, arbitrary surface structures are of interest, an extension to estimate slope gradients would be a significant improvement of the proposed approach. Measuring on non-flat surfaces, however, leads to non-Gaussian intensity distributions on the imaging sensor. The resulting intensity distribution depends on the slope gradient, direction, and sample height, leading to a large amount of possible distribution shapes on the imaging detector. Therefore, the integration of machine learning is a promising approach for this application.

Bibliography

[1]   D. Imkamp, R. Schmitt, and J. Berthold, "Blick in die Zukunft der Fertigungsmesstechnik: DIE VDI/VDE-GMA roadmap Fertigungsmesstechnik 2020", *Technisches Messen*, vol. 79, no. 10, pp. 433–439, 2012.

[2]   X. Jiang and D. J. Whitehouse, "Precision metrology", *Philosophical Transactions of the Royal Society A: Mathematical, Physical and Engineering Sciences*, vol. 370, no. 1973, pp. 4154–4160, 2012.

[3]   E.V., VDI Verein Detuscher Ingenieure, *Fertigungsmesstechnik 2020, Technologie - Roadmap für die Messtechnik in der industriellen Produktion*. Düsseldorf: Düsseldorf: VDI/VDE-Gesellschaft Mess- und Automatisierungstechnik, 2011.

[4]   R. Schmitt and F. Moenning, "Ensure success with inline-metrology", in *CVIII IMEKO WOLRD CONGRESS Metrology for a Sustainable Development*, 2006.

[5]   T. F. Yao, A. Duenner, and M. Cullinan, "In-line dimensional metrology in nanomanufacturing systems enabled by a passive semiconductor wafer alignment mechanism", *Journal of Micro and Nano-Manufacturing*, vol. 5, no. 1, 2017.

[6]   A. Yogeswaran and P. Payeur, "3d surface analysis for automated detection of deformations on automotive body panels", *New Advances in Vehicular Technology and Automotive Engineering*, pp. 953–978, 2012.

[7]   D. J. Whitehouse, *Handbook of surface and nanometrology*. Taylor & Francis, 2002.

[8]   K. Maize, Y. Mi, M. Cakmak, and A. Shakouri, "Real-Time Metrology for Roll-To-Roll and Advanced Inline Manufacturing: A Review", *Advanced Materials Technologies*, vol. 8, no. 2, p. 2 200 173, 2023.

[9]   G. Sansoni, M. Trebeschi, and F. Docchio, "State-of-The-Art and Applications of 3D Imaging Sensors in Industry, Cultural Heritage, Medicine, and Criminal Investigation", *Sensors*, vol. 9, no. 1, pp. 568–601, 2009.

86

[10] J. Li *et al.*, "Edge quality based iterative deconvolution algorithm for motion blurred gray scale images for geometrical measures", *Journal of Physics: Conference Series*,

[11] T. S. Cho, "Motion blur removal from photographs", Ph.D. dissertation, Massachusetts Institute of Technology, 2010.

[12] "Safety of laser products - part 1: Equipment classification and requirements", EN 60825-1:2014/AC:2022-03, European Committee for Electrotechnical Standardization, Brussels, BEL, Standard, 2022.

[13] Metrology.News. "Laser Profile Scanners Cutting Edge Performance Improves Production Quality". (2022), [Online]. Available: `https://metrology.news/laser-profile-scanners-cutting-edge-performance-improves-production-quality-and-performance/` (visited on 12/20/2023).

[14] L. Traxler, L. Ginner, S. Breuss, and B. Blaschitz, "Experimental Comparison of Optical Inline 3D Measurement and Inspection Systems", *IEEE Access*, vol. 9, pp. 53 952–53 963, 2021.

[15] A. A. Michelson and J.-R. Benoît, "Détermination expérimentale de la valeur du mètre en longueurs d'ondes lumineuses", *Trav. Mem. Bur. Int. Poids Mes*, vol. 11, no. 3, p. 85, 1895.

[16] R. Leach, *Fundamental principles of engineering nanometrology*. Elsevier, 2014.

[17] R. Saathof, M. Thier, R. Hainisch, and G. Schitter, "Integrated system and control design of a one DoF nano-metrology platform", *Mechatronics*, vol. 47, pp. 88–96, 2017.

[18] P. K. Subrahmanyan, "A model approach to precision motion control", Ph.D. dissertation, Massachusetts Institute of Technology, 1999.

[19] Q. He, S. Fan, N. Chen, R. Tan, F. Chen, and D. Fan, "Analysis of Inductive Displacement Sensors with Large Range and Nanoscale Resolution", *Applied Sciences 2021, Vol. 11, Page 10134*, vol. 11, no. 21, p. 10 134, 2021.

[20] S. Fericean and R. Droxler, "New noncontacting inductive analog proximity and inductive linear displacement sensors for industrial automation", *IEEE Sensors Journal*, vol. 7, no. 11, pp. 1538–1545, 2007.

[21] R. M. Schmidt, G. Schitter, and A. Rankers, *The design of high performance mechatronics-: high-Tech functionality by multidisciplinary system integration.* Ios Press, 2020.

[22] X. Liu, K. Peng, Z. Chen, H. Pu, and Z. Yu, "A new capacitive displacement sensor with nanometer accuracy and long range", *IEEE Sensors Journal*, vol. 16, no. 8, pp. 2306–2316, 2016.

[23] M. Kim, W. Moon, E. Yoon, and K. R. Lee, "A new capacitive displacement sensor with high accuracy and long-range", *Sensors and Actuators A: Physical*, pp. 135–141, 2006.

[24] B. Gmeiner, "kapascan : A versatile scanning capacitive imaging device for the analysis of battery parts", Master Thesis, Johannes Kepler Univerity Linz, 2018.

[25] K. Harding, "Chromatic Confocal Imaging", in *Handbook of Optical Dimensional Metrology*, CRC Press, 2012, pp. 428–432.

[26] A. Donges and R. Noll, *Laser Measurement Technology: Fundamentals and Applications*, 1st ed. Springer, 2015, pp. 247–278.

[27] H. Schwenke, U. Neuschaefer-Rube, T. Pfeifer, and H. Kunzmann, "Optical methods for dimensional metrology in production engineering", *CIRP Annals - Manufacturing Technology*, vol. 51, no. 2, pp. 685–699, 2002.

[28] F. Blateyron, "Chromatic Confocal Microscopy", in *Optical Measurement of Surface Topography*, R. Leach, Ed. Berlin, Heidelberg: Springer Berlin Heidelberg, 2011, pp. 71–106.

[29] T. Scheimpflug, *Improved Method and Apparatus for the Systematic Alteration or Distortion of Plane Pictures and Images by Means of Lenses and Mirrors for Photography and for other purposes.* GB Patent No. 1196, 1904.

[30] E. Csencsics, J. Schlarp, T. Glaser, T. Wolf, and G. Schitter, "Reducing the Speckle-Induced Measurement Uncertainty in Laser Triangulation Sensors", *IEEE Transactions on Instrumentation and Measurement*, vol. 72, pp. 1–9, 2023.

[31] Micro-epsilon, *ILD1900-2-IE Operating Instructions optoNCDT 1900 EtherCAT*.

[32] M. M. Auerswald, A. von Freyberg, and A. Fischer, "Laser line triangulation for fast 3D measurements on large gears", *International Journal of Advanced Manufacturing Technology*, vol. 100, no. 9-12, pp. 2423–2433, 2019.

[33] W. S. Boyle and G. E. Smith, "Charge Coupled Semiconductor Devices", *Bell System Technical Journal*, vol. 49, no. 4, pp. 587–593, 1970.

[34] M. F. Tompsett, G. F. Amelio, and G. E. Smith, "Charge Coupled 8-Bit Shift Register", *Applied Physics Letters*, vol. 17, no. 3, pp. 111–115, 1970.

[35] A. Polatoglu and İ. C. Özkesen, "Working Principles of CCD and CMOS Sensors and Their Place in Astronomy", *Journal of Anatolian Physics and Astronomy*, vol. 2, no. 1, pp. 51–59, 2022.

[36] E. Dereniak and D. Crowe, *Optical Radiation Detectors.* Wiley, 1984.

88

[37]   M. Lesser, "Charge-coupled device (CCD) image sensors", in *High Performance Silicon Imaging: Fundamentals and Applications of CMOS and CCD Sensors*, 2nd ed., Woodhead Publishing, 2020, ch. 3, pp. 75–94.

[38]   D. Durini, *High performance silicon imaging: Fundamentals and applications of CMOS and CCD sensors*, 2nd ed. Woodhead Publishing, 2019, pp. 1–523.

[39]   G. P. Weckler, "Operation of p-n Junction Photodetectors in a Photon Flux Integrating Mode", *IEEE Journal of Solid-State Circuits*, vol. 2, no. 3, pp. 65–73, 1967.

[40]   A. El Gamal and H. Eltoukhy, "CMOS image sensors", *IEEE Circuits and Devices Magazine*, vol. 21, no. 3, pp. 6–20, 2005.

[41]   E. R. Fossum, "Active pixel sensors: are CCDs dinosaurs?", in *Charge-Coupled Devices and Solid State Optical Sensors III*, M. M. Blouke, Ed., International Society for Optics and Photonics, vol. 1900, SPIE, 1993, pp. 2–14.

[42]   P. J. Noble, "Self-Scanned Silicon Image Detector Arrays", *IEEE Transactions on Electron Devices*, vol. ED-15, no. 4, pp. 202–209, 1968.

[43]   P. B. Denyer, D. Renshaw, G. Wang, M. Y. Lu, and S. Anderson, "On-chip CMOS sensors for VLSI imaging systems", in *IFIP Transactions VLSI'91*, 1991, p. 10.

[44]   S. Kleinfelder, S. Lim, X. Liu, and A. El Gamal, "A 10000 frames/s CMOS digital pixel sensor", *IEEE Journal of Solid-State Circuits*, vol. 36, no. 12, pp. 2049–2059, 2001.

[45]   Y. Tochigi, K. Hanzawa, Y. Kato, N. Akahane, R. Kuroda, and S. Sugawa, "A prototype high-speed CMOS image sensor with 10,000,000 fps burst-frame rate and 10,000 fps continuous-frame rate", *Digital Photography VII*, vol. 7876, pp. 153–160, 2011.

[46]   S. Yadav, C. Jain, and A. Chugh, "Evaluation of Image Deblurring Techniques Evaluation of Image Deblurring Techniques Charu jain", *Article in International Journal of Computer Applications*, vol. 139, no. 12, pp. 975–8887, 2016.

[47]   M. Tanaka, K. Yoneji, and M. Okutomi, "Motion blur parameter identification from a linearly blurred image", *Digest of Technical Papers - IEEE International Conference on Consumer Electronics*, 2007.

[48]   A. Levin, Y. Weiss, F. Durand, and W. T. Freeman, "Understanding blind deconvolution algorithms", *IEEE Transactions on Pattern Analysis and Machine Intelligence*, vol. 33, no. 12, pp. 2354–2367, 2011.

[49] A. Patel and A. Ganatra, "A Survey on Different Image Deblurring Techniques A Survey on different Image Deblurring Techniques Fagun Vankawala M. Tech (Computer Engineering) (pursuing) Charusat", *Article in International Journal of Computer Applications*, vol. 116, no. 13, pp. 975–8887, 2015.

[50] J. Sun, W. Cao, Z. Xu, and J. Ponce, "Learning a convolutional neural network for non-uniform motion blur removal", in *Proceedings of the IEEE Computer Society Conference on Computer Vision and Pattern Recognition*, 2015, pp. 769–777.

[51] C. Khare, K. Kumar, and Nagwanshi, "Implementation and Analysis of Image Restoration Techniques", *International Journal of Computer Trends and Technology*,

[52] W. H. Richardson, "Bayesian-Based Iterative Method of Image Restoration*", *Journal of the Optical Society of America*, vol. 62, no. 1, p. 55, 1972.

[53] A. K. Soe and X. Zhang, "A simple PSF parameters estimation method for the de-blurring of linear motion blurred images using wiener filter in OpenCV", *2012 International Conference on Systems and Informatics, ICSAI 2012*, pp. 1855–1860, 2012.

[54] J. M. Lee, J. H. Lee, K. T. Park, and Y. S. Moon, "Image deblurring based on the estimation of PSF parameters and the post-processing", *Optik*, vol. 124, no. 15, pp. 2224–2228, 2013.

[55] K. Xie *et al.*, "An experimental study of motion blur in optical co-rodinate metrology for dynamic measurements of geometrical features", *Joint International IMEKO TC1+ TC7+ TC13 Symposium*, 2011.

[56] B. Heflin, B. Parks, W. Scheirer, and T. Boult, "Single image deblurring for a real-time face recognition system", in *IECON 2010-36th Annual Conference on IEEE Industrial Electronics Society*, IEEE, 2010, pp. 1185–1192.

[57] M. Dobeš, L. MacHala, and T. Fürst, "Blurred image restoration: A fast method of finding the motion length and angle", *Digital Signal Processing*, vol. 20, no. 6, pp. 1677–1686, 2010.

[58] X. Wang and Y. Zhou, "A mechanical transmission based image de-blurring method used for on-line surface quality inspection", *Measurement: Journal of the International Measurement Confederation*, vol. 151, 2020.

[59] T. Hayakawa, T. Watanabe, and M. Ishikawa, "Real-time high-speed motion blur compensation system based on back-and-forth motion control of galvanometer mirror", *Optics Express*, vol. 23, no. 25, p. 31 648, 2015.

90

[60] J. Schlarp, E. Csencsics, and G. Schitter, "Design and evaluation of an integrated scanning laser triangulation sensor", *Mechatronics*, vol. 72, p. 102 453, 2020.

[61] D. Wertjanz, T. Kern, E. Csencsics, G. Stadler, and G. Schitter, "Compact scanning confocal chromatic sensor enabling precision 3-D measurements", *Applied Optics*, vol. 60, no. 25, pp. 7511–7517, 2021.

[62] M. Laimer, D. Wertjanz, P. Gsellmann, G. Schitter, and E. Csencsics, "High-precision 3D measurements on moving objects", *IEEE Transactions on Mechatronics*, 2023, under review.

[63] D. Wertjanz, E. Csencsics, T. Kern, and G. Schitter, "Bringing the Lab to the Fab: Robot-Based Inline Measurement System for Precise 3-D Surface Inspection in Vibrational Environments", *IEEE Transactions on Industrial Electronics*, vol. 69, no. 10, pp. 10 666–10 673, 2022.

[64] N. Joshi, R. Szeliski, and D. J. Kriegman, "PSF estimation using sharp edge prediction", *26th IEEE Conference on Computer Vision and Pattern Recognition, CVPR*, 2008.

[65] M. A. Drouin and J. A. Beraldin, "Active Triangulation 3D Imaging Systems for Industrial Inspection", in *3D Imaging, Analysis and Applications: Second Edition*, Springer International Publishing, 2020, pp. 109–165.

[66] Micro-epsilon, *Operating Instructions optoNCDT 1420*.

[67] T. Yoshizawa, *Handbook of Optical Metrology: Principles and Applications*. CRC Press, 2009, pp. 1–731.

[68] H. M. Merklinger, "Principles of view camera focus", 1996.

[69] R. Bellman, "Dynamic Programming", *Science*, vol. 153, no. 3731, pp. 34–37, 1966.

[70] F. Y. Kuo and I. H. Sloan, "Lifting the Curse of Dimensionality",

[71] G. T. Reddy *et al.*, "Analysis of Dimensionality Reduction Techniques on Big Data", *IEEE Access*, vol. 8, pp. 54 776–54 788, 2020.

[72] C. O. S. Sorzano, J. Vargas, and A. P. Montano, "A survey of dimensionality reduction techniques", 2014.

[73] M. Partridge and R. A. Calvo, "Fast Dimensionality Reduction and Simple PCA", *Intelligent Data Analysis*, vol. 2, no. 3, pp. 203–214, 1998.

[74] B. Mohammed, S. Hasan, and A. Mohsin Abdulazeez, "A Review of Principal Component Analysis Algorithm for Dimensionality Reduction", *Journal of Soft Computing and Data Mining*, vol. 2, no. 1, pp. 20–30, 2021.

[75] R. Bro and A. K. Smilde, "Principal component analysis", *Analytical Methods*, vol. 6, no. 9, pp. 2812–2831, 2014.

[76] H. P. Gavin, "The Levenberg-Marquardt algorithm for nonlinear least squares curve-fitting problems", *Department of civil and environmental engineering, Duke University*, vol. 19, 2019.

[77] C. M. Bishop, *Pattern Recognition and Machine Learning* (Information science and statistics), 1st ed. 2006. Corr. 2nd printing. Springer, 2006, pp. 423–460.

[78] I. J. Myung, "Tutorial on maximum likelihood estimation", *Journal of Mathematical Psychology*, vol. 47, no. 1, pp. 90–100, 2003.

[79] D. A. Reynolds *et al.*, "Gaussian mixture models.", *Encyclopedia of biometrics*, vol. 741, no. 659-663, 2009.

[80] J. A. Bilmes *et al.*, "A gentle tutorial of the em algorithm and its application to parameter estimation for gaussian mixture and hidden markov models", *International computer science institute*, vol. 4, no. 510, p. 126, 1998.

[81] A. P. Dempster, N. M. Laird, and D. B. Rubin, "Maximum Likelihood from Incomplete Data Via the EM Algorithm", *Journal of the Royal Statistical Society: Series B (Methodological)*, vol. 39, no. 1, pp. 1–22, 1977.

[82] G. J. McLachlan and T. Krishnan, *The EM algorithm and extensions*. John Wiley & Sons, 2007.

[83] G. Xuan, W. Zhang, and P. Chai, "EM algorithms of Gaussian mixture model and Hidden Markov Model", *IEEE International Conference on Image Processing*, vol. 1, pp. 145–148, 2001.

[84] G. L. Turin, "An Introduction to Matched Filters", *IRE Transactions on Information Theory*, vol. 6, no. 3, pp. 311–329, 1960.

[85] G. L. Turin, "An Introduction to Digital Matched Filters", *Proceedings of the IEEE*, vol. 64, no. 7, pp. 1092–1112, 1976.

[86] C. Will, K. Shi, R. Weigel, and A. Koelpin, "Advanced template matching algorithm for instantaneous heartbeat detection using continuous wave radar systems", *2017 1st IEEE MTT-S International Microwave Bio Conference, IMBioC 2017*, 2017.

[87] K. Sabu, S. Chaudhuri, P. Rao, and M. Patil, "An Optimized Signal Processing Pipeline for Syllable Detection and Speech Rate Estimation", 2021.

[88] H. Nobach and M. Honkanen, "Two-dimensional Gaussian regression for subpixel displacement estimation in particle image velocimetry or particle position estimation in particle tracking velocimetry", *Experiments in Fluids*, vol. 38, no. 4, pp. 511–515, 2005.

92

[89]   C. E. Willert and M. Gharib, "Digital particle image velocimetry", *Experiments in Fluids*, vol. 10, no. 4, pp. 181–193, 1991.

Eigenständigkeitserklärung

Hiermit erkläre ich, dass die vorliegende Arbeit gemäß dem Code of Conduct, insbesondere ohne unzulässige Hilfe Dritter und ohne Benutzung anderer als der angegebenen Hilfsmittel, angefertigt wurde. Die aus anderen Quellen direkt oder indirekt übernommenen Daten und Konzepte sind unter Angabe der Quelle gekennzeichnet.

Die Arbeit wurde bisher weder im In- noch im Ausland in gleicher oder ähnlicher Form in anderen Prüfungsverfahren vorgelegt.

Wien, im Dezember 2023

Thomas Kern, BSc